

Dosimetry and linac acceptance for the 1.5 T MRI-Linac

Simon Woodings

Dosimetry and linac acceptance for the 1.5 T MRI-Linac

Simon Woodings

Cover description

MRI-linac stained glass window by André Wopereis.

Photograph by Christiaan van Kesteren, Center for Multimedia, UMCU.

Cover design by Evelyn Wan.

Dosimetry and linac acceptance for the 1.5 T MRI-Linac

PhD Thesis, Utrecht University, The Netherlands

Simon Woodings, 2019

Manuscript:

Layout: S Woodings

Typesetting: L^AT_EX 2_ε

Printed by: boekendeal.nl

ISBN: 978-90-393-7256-2

Copyright:

© S Woodings

© IOP Publishing (Chapters 2, 4 and 6)

© Wiley Periodicals (Chapters 3 and 5)

Dosimetry and linac acceptance for the 1.5 T MRI-Linac

Dosimetrie en versneller acceptatie van de 1.5 T MRI-Versneller

(met een samenvatting in het Nederlands)

Proefschrift

ter verkrijging van de graad van doctor aan de
Universiteit Utrecht
op gezag van de rector magnificus, prof.dr. H.R.B.M. Kummeling,
ingevolge het besluit van het college voor promoties
in het openbaar te verdedigen
op 11 juni 2020 des middags te 2:30 uur

door

Simon James Woodings

geboren op 31 mei 1973 te Perth, Australië

Promotor: Prof.dr. B. W. Raaymakers

Copromotoren: Dr.ir. J. W. H. Wolthaus
Dr. B. van Asselen

Contents

1	Introduction	7
2	Dosimetry formalism	15
3	Magnetic field correction factors	29
4	PTW microDiamond in the MRI-linac	43
5	Linac acceptance of the MRI-linac	59
6	Beam characterisation of the MRI-Linac	83
7	Summary and general discussion	103
8	Samenvatting	111
	Bibliography	115
	Acknowledgements	125
	About the author	127

CHAPTER 1

Introduction

“See it, zap it!”

1.1 Radiation therapy

Radiation Oncology is the treatment of cancer using ionizing radiation. To achieve this, the goal is to deliver as high a radiation dose as possible to the target while minimizing dose to normal tissue and organs at risk. The target traditionally consists of a gross tumour volume (GTV) which can be observed, and a clinical target volume (CTV) which includes regions of potential microscopic spread of disease. A planned target volume (PTV) is created which includes the GTV, CTV and a physical margin to cover the various treatment uncertainties including patient setup, internal motion and limitations of the treatment system (International Commission on Radiation Units & Measurements, 1999, 2010). The ability of radiotherapy to treat the CTV without needing to invasively remove the tissue is a major advantage. Easy and accurate identification and irradiation of the target (see it, zap it) is an ongoing goal of radiation oncology.

1.2 IGRT

Image guided radiation therapy (IGRT) is a technique of identifying the target position (usually the GTV) at the time of treatment, and making a positional correction if necessary so that the target receives adequate treatment. This technique increases the probability of correctly irradiating the target, and facilitates smaller PTV margins and radiation beams because the positional uncertainty has been reduced. Smaller margins can significantly decrease the volume of irradiated tissue, with volume being proportional to the diameter cubed (x^3), which potentially allows higher doses to be delivered to the target, and normal tissue toxicity to be reduced (Verellen *et al.*, 2007).

X-ray cone beam computed tomography (CBCT) is a commonly available tool for 3D visualisation of the target region of the patient. It is highly accurate for co-registering implanted markers or bony anatomy. CBCT was a major advance in radiotherapy, facilitating IGRT for many anatomical sites (Jaffray *et al.*, 2002).

1.3 MRgRT

We are now entering a new era of magnetic resonance guided radiation therapy (MRgRT), where the principles of IGRT are applied but with three distinct advantages: (i) high quality soft-tissue contrast allowing direct visualization of the position and shape of the target independent of bony anatomy or implanted markers, (ii) adaptive radiation therapy (ART) where the plan can be re-optimised based on MR imaging of the patient at the time of treatment and (iii) fast MR intra-fraction imaging supporting interventions that mitigate or take into account motion of the target and organs at risk.

The high-quality, geometrically accurate imaging of MRgRT facilitates full plan adaptation based on the current anatomical information. It improves upon existing RT for highly-mobile, soft-tissue targets such as, for example, oesophagus, rectum and oligo-metastatic lymph nodes. MRgRT images during and after treatment will also facilitate the re-calculating of dose (dose reconstruction) for the actual treatment position, rather than the position at the start of the fraction. This in turn enables treatment methods based on dose accumulation, and increased precision for dose-response assessment for tumours and organs at risk.

1.4 Commercial MRgRT systems

Two MRgRT systems are currently commercially available; the Unity system from Elekta AB (Stockholm Sweden) and the MRIdian system from Viewray (Cleveland, Ohio). The Elekta Unity 1.5 T system (figure 1.1) grew out of the pioneering MRgRT concepts of Jan Lagendijk at University Medical Center Utrecht (UMCU) in 1999 (Lagendijk *et al.*, 2002; Raaymakers *et al.*, 2004; Lagendijk *et al.*, 2008). UMCU, Elekta AB and Philips (Best, the Netherlands) worked together to create several 1.5 T magnetic resonance imaging linear accelerator (MRI-linac) prototypes that demonstrated the feasibility of simultaneous MR imaging and megavoltage (MV) radiation delivery (Raaymakers *et al.*, 2009; Lagendijk *et al.*, 2014). The first clinical treatments with the 7 MV, 1.5 T prototype system were delivered in May 2017 at UMCU (Raaymakers *et al.*, 2017). These developments led to clinical treatments with the Elekta Unity 1.5 T MRI-linac (Werensteijn-Honingh *et al.*, 2019). The 0.35 T MRIdian was developed by James F. Dempsey, Viewray and the University of Washington, USA (Mutic *et al.*, 2014) and was first used clinically in 2014 with Cobalt-60 teletherapy. New MRIdian systems use 6 MV linacs. This thesis concerns the clinical introduction of the Elekta Unity system.

1.5 Dose deposition and measurements within a magnetic field

One striking difference between conventional linacs and MRI-linacs is dose delivery in the presence of a magnetic field.



Figure 1.1: The Elekta Unity 1.5 T MRI linac U02 at University Medical Center Utrecht.

1.5.1 Impact of magnetic field on dose

The MRI-linac radiation beam consists of photons. Photon interactions within the patient release electrons, which have an electric charge. Electrons moving within the magnetic field experience the Lorentz force, which causes the electrons to move in curved trajectories (see figure 1.2). As a result the deposition of energy (and therefore dose) is different in an MRI-linac, than in a regular linac.

In regions of quasi electronic equilibrium (where the inflow and outflow of electrons from a volume are almost the same) there is only a small effect due to the magnetic field. However, where the fluence of the secondary electrons is changing, the effect of the magnetic field on the electrons can make a large difference to the radiation dose. This applies at the beam entrance (build up), beam exit, and edges of the beam (penumbra). The long range of electrons travelling curved paths in air leads to new phenomena. The electron return effect (ERE) is where electrons in low density material (air) can curve back to the tissue that is upstream. This can be relevant at a tissue interface, such as the lung surface, or the exit surface of the patient (Raaijmakers *et al.*, 2005). Additionally there is the electron streaming effect (ESE), where electrons can spiral along the magnetic field lines and thus travel through the air in the patient superior or inferior directions. Most of these electrons originate from the beam exit side of the patient. The ESE can require preventative measures to avoid having increased dose outside the beam (eg Malkov *et al.* (2019); Park *et al.* (2018)).

1.5.2 Reference (and absolute) dosimetry

Dose measuring equipment (dosimeters) are affected by the magnetic field. Dosimetry is a fundamental component of radiation oncology – the ability to accurately measure

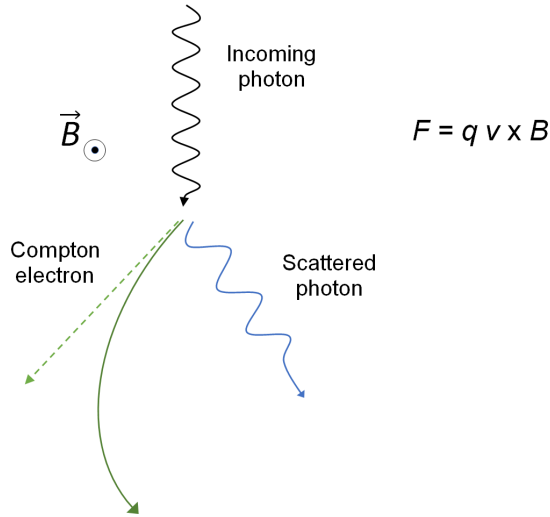


Figure 1.2: Electrons with charge q travel with curved trajectories at velocity v within a magnetic field B , under the influence of the Lorentz force F .

and calibrate radiation doses. Dose measurements depend on the design of the radiation detectors, and on the patient-equivalent material ('phantom') in which they are used. A strong magnetic field and the resultant curved electron trajectories can affect the flux into the radiation detectors, as well as the behaviour of the electrons inside the detectors, and therefore their sensitivity. Detailed investigation of the detector behavior in a magnetic field is necessary to ensure that accurate dose measurements can be made on MRI-linacs.

Reference dosimetry involves measuring the absolute dose in Gray, where $1 \text{ Gy} = 1 \text{ J/kg}$, usually at a specific point and with specific reference beam conditions. This is critical for the comparison of radiation treatments and treatment outcomes, and thus for the consistency of treatments between institutes and countries. Traditionally this is defined via national and international codes of practice (eg NCS 18 (Aalbers *et al.*, 2008), IAEA TRS 398 (Andreo *et al.*, 2000)). At the time of writing, magnetic field effects are not included within the dosimetry codes of practice and therefore they are not accurate when applied to a MRI-linac. Thus it is vital that information on dosimetry within a magnetic field, such as in chapters 2 and 3 be published for use internationally by clinical physicists.

1.5.3 Relative dosimetry

Relative dosimetry involves measuring doses at multiple spatial points, in 2D profiles, or 3D volumes, and comparing the doses within the dose distribution. Both absolute and relative dosimetry measurements are critical to the commissioning of the radiation beam in the treatment planning system (TPS) which is used to generate treatment plans

to fulfill the doctor's prescribed treatment.

1.6 Acceptance and commissioning

In order to safely and effectively deliver radiation beams from a treatment machine to a patient, it is necessary to characterise the system and validate it for clinical use. Acceptance testing is the process of demonstrating that a new system meets the criteria that were specified for its use. Commissioning is the process of measuring data specific to the new machine, which can be used for beam modelling within the treatment planning system. It is also used for answering clinically relevant questions, and for establishing a baseline of machine performance for future quality assurance (QA) tests. The fundamentals of this process are well documented in the Medical Physics and Radiotherapy communities; for example, by the Institute of Physicists and Engineers in Medicine (IPEM) (Kirby *et al.*, 2006). Due to the nature of this machine and the presence of the strong magnetic field, new methods and equipment have had to be adapted for some of the existing tests, and some entirely new tests have had to be created.

Fundamentally, the system alignment and beam geometry must be highly accurate for stereotactic body radiation therapy (SBRT) applications. Accurate dose calibration is critical. MR image quality and geometric accuracy (Tijssen *et al.*, 2019) are the basis of the system, and therefore significant testing is required. This has been well established at UMCU and within the Elekta consortium. Tijssen *et al.* also recognise the advent of hybrid tests of the combined MR-MV system, such as the image quality and geometric accuracy during irradiation.

Commissioning of the treatment planning system (TPS) and, more specifically, the Unity 7 MV beam model within the TPS, closely conforms to existing guidelines (Bruinvis *et al.*, 2005; van der Wal *et al.*, 2013; Ezzell *et al.*, 2003). The MRI-linac is designed with a fixed table position. Thus the treatment target is not necessarily located in the center of the bore (the radiation isocenter) as it typically would be with a standard linac. Small off-axis beams are more frequent and more important in an MRI-linac. Magnetic-field related effects such as ERE at the patient surface and within tissue inhomogeneities were also considered. This required additional data collection as part of the beam characterisation. To ensure accurate characterisation of small beams and beam edges (penumbra), a specialised small-beam microDiamond detector was also commissioned specifically for this work. TPS commissioning culminated in plan-specific QA of clinical IMRT plans.

The Unity system supports a variety of plan adaptation options, from rigid-registration position correction similar to existing CBCT-based IGRT, to full fluence re-optimisation. This incorporates all available information including anatomical deformations, to achieve the optimal treatment plan for the patient at the time of treatment. With such a complex range of options available, significant attention must be given to establishing the desired clinical workflow for each target area (Winkel *et al.*, 2019) as well as consideration for treatment interruption recovery and alternative treatment options (Raaymakers *et al.*, 2017).

The Unity system comprises numerous subsystems and each of these, as well as the combined whole, must be tested for correct connectivity and consistency of coordinate systems and data sharing. Checks include end-to-end tests designed to validate whole-of-system geometric accuracy and dose accuracy.

1.7 Thesis outline

This thesis concerns the Unity MRI-linac (and its prototypes). The overall aim is to ensure that the MRI-linac is safe and effective for clinical use, and can be introduced into the clinic. To this end it was necessary to identify and solve issues related to reference dosimetry in a magnetic field, acceptance testing of a new system in a new physical configuration, and beam characterisation in a magnetic field. These issues are addressed in the following chapters.

As dosimetry is the foundation of commissioning, QA and dose calculation, in chapter 2 a generic formalism is proposed for reference dosimetry in the presence of a magnetic field. Besides the regular correction factors from the conventional reference dosimetry formalisms, two factors are used to take into account magnetic field effects: 1) a dose conversion factor to correct for the change in local dose distribution and 2) a correction of the reading of the dosimeter used for the reference dosimetry measurements. The formalism is applied to the Elekta MRI-Linac, for which the 1.5 T magnetic field is orthogonal to the 7 MV photon beam.

A key question is whether these new magnetic field correction factors are applicable for types (groups) of ion chambers, or whether a factor must be specifically measured for each individual chamber. To investigate this issue, in chapter 3 an assessment of the chamber-to-chamber variation of the magnetic field correction factor is made for PTW30013 and FC65-G type ion chambers when they are oriented anti-parallel (\parallel) to, or perpendicular (\perp) to, the magnetic field.

To ensure that small radiation beams on the MRI-linac can be accurately measured and characterised, in chapter 4 the performance of the PTW 60019 microDiamond in a 1.5 T magnetic field is investigated. This is critical for the intended stereotactic body radiation therapy (SBRT) use of the MRI-linac. MicroDiamond warmup, constancy, dose linearity, dose rate linearity, field size dependence, leakage, angular sensitivity and effective point of measurement (EPoM) are assessed. The goal is to determine if the PTW 60019 microDiamond detector is suitable for MRI-linac small-beam commissioning and quality assurance.

In chapter 5 an acceptance procedure for the new Elekta Unity 1.5 T MRI-linac is developed and implemented. Tests are adopted and, where necessary adapted, from AAPM TG106 and TG142, IEC 60976 and NCS 9 and NCS 22 guidelines. Adaptations are necessary because of the atypical maximum field size (57.4 x 22 cm), FFF beam, the non-rotating collimator, the absence of a light field, the presence of the 1.5 T magnetic field, restricted access to equipment within the bore, table motion only in the longitudinal

direction, and MR image to MV treatment alignment. The performance specifications are set for SBRT. The goals are to develop and describe a comprehensive set of tests, and to demonstrate the feasibility of the procedure by applying it to the first MRI-linac.

In chapter 6 the Elekta 1.5 T MRI-linac 7 MV flattening filter free (FFF) radiation beam is characterised for the first time. The goal is to assess its suitability for clinical use, and to provide the data necessary for a beam model in the treatment planning system to be created and used for the first clinical treatments with the MRI-linac. Following acceptance testing, beam characterisation data are acquired with various ion chamber and film detectors in water phantoms. Beam characterisation parameters such as penumbra width and surface dose are measured and compared to a standard Elekta Agility linac.

Finally chapter 7 includes a discussion of additional acceptance testing and commissioning that is required for the whole system, including the treatment planning system, MRI, connectivity, plan QA and end-to-end tests. There is also discussion of developments for the future of the MRI-linac.

CHAPTER 2

A formalism for reference dosimetry in photon beams in the presence of a magnetic field

The following chapter is based on:

van Asselen B., Woodings S.J., Hackett S.L., van Soest T.L., Kok J.G.M., Raaymakers B.W. and Wolthaus J.W.H. 2018 A formalism for reference dosimetry in photon beams in the presence of a magnetic field *Physics in Medicine and Biology* 63 125008

Abstract

A generic formalism is proposed for reference dosimetry in the presence of a magnetic field. Besides the regular correction factors from the conventional reference dosimetry formalisms, two factors are used to take into account magnetic field effects: 1) a dose conversion factor to correct for the change in local dose distribution and 2) a correction of the reading of the dosimeter used for the reference dosimetry measurements. The formalism was applied to the Elekta MRI-Linac, for which the 1.5 T magnetic field is orthogonal to the 7 MV photon beam. For this setup at reference conditions it was shown that the dose decreases with increasing magnetic field strength. The reduction in local dose for a 1.5 T transverse field, compared to no field is $0.51\% \pm 0.03\%$ at the reference point of 10 cm depth. The effect of the magnetic field on the reading of the dosimeter was measured for two waterproof ionization chambers types (PTW 30013 and IBA FC65-G) before and after multiple ramp-up and ramp-downs of the magnetic field. The chambers were aligned perpendicular and parallel to the magnetic field. The corrections of the readings of the perpendicularly aligned chambers were 0.967 ± 0.002 and 0.957 ± 0.002 for respectively the PTW and IBA ionization chambers. In the parallel alignment the corrections were small; 0.997 ± 0.001 and 1.002 ± 0.003 for the PTW and IBA chamber respectively. The change in reading due to the magnetic field can be measured by individual departments. The proposed formalism can be used to determine the correction factors needed to establish the absorbed dose in a magnetic field. It requires Monte Carlo simulations of the local dose and measurements of the response of the dosimeter. The formalism was successfully implemented for the MRI-Linac and is applicable for other field strengths and geometries.

2.1 Introduction

The combination of a radiotherapy unit with a MRI scanner allows direct visualization of the target during the actual radiotherapy by providing excellent soft tissue contrast in real time. This will allow the development of high-precision MRI-guided radiotherapy. Several integrated MRI guided devices are under development or in clinical use (Keall *et al.*, 2014; Fallone, 2014; Mutic *et al.*, 2014; Lagendijk *et al.*, 2014). Beside the technical differences between systems, such as the magnetic field strength, photon beam energy spectrum and the orientation of the magnetic field relative to the photon beam, all deliver the dose in the presence of a magnetic field.

As a magnetic field only affects charged particles, it does not affect photon trajectories, and therefore the photon fluence will not change in a magnetic field. The Kerma is not affected, since the energy transferred to the electrons is the same with or without a magnetic field. However, the magnetic field will change the trajectories of the resultant electrons via the Lorentz force, and will consequently affect the whole dose distribution in several ways. The impact of the magnetic field on the dose distribution depends on the magnetic field strength and its orientation relative to the photon beam, and also on the energy of the electrons. Examples of changes in the dose distribution are in the buildup region, the depth of the maximum dose, the penumbra regions, near density interfaces and also in regions of transient charged particle equilibrium (Raaijmakers *et al.*, 2007, 2008; Oborn *et al.*, 2009, 2010; Keyvanloo *et al.*, 2012).

For reference dosimetry in a magnetic field, the magnetic field effects have to be taken into account and standard protocols have to be adapted, in which reference dosimetry is the process of determining the absorbed dose to water at a point under reference conditions (Aalbers *et al.*, 2008; Almond *et al.*, 1999; Andreo *et al.*, 2000). There are two issues to be considered relative to a reference setup with a photon beam quality without a magnetic field. First is the change in local dose distribution due to the change in electron trajectories. Second, the magnetic field has an influence on the reading of the dosimeter used for reference dosimetry and this influence also has to be included in the adapted formalism (Smit *et al.*, 2013).

The dose distribution in an area of transient charged particle equilibrium (i.e. beyond dose maximum) changes due to the magnetic field, for example in the isocenter at 10 cm depth for a 10x10 cm² field. At such a location, which is commonly chosen as the reference setup, the local dose distribution is different relative to the dose without a magnetic field due to the change in electron trajectories around the photon interaction point (Wolthaus *et al.*, 2016a). The electrons effectively deposit their energy in a different location. To clarify this effect, consider a broad photon beam with a magnetic field perpendicular to the central axis. In this case, the electrons trajectories will curve, which results effectively in increased energy deposition closer to the photon interaction point and reduction of the dose deposited downstream 2.1. Thus at any specified depth (beyond the depth of the dose maximum) the absorbed dose will be lower with a magnetic field than without a magnetic field. The net effect will depend on the magnetic

field strength and its orientation (Raaijmakers *et al.*, 2008).

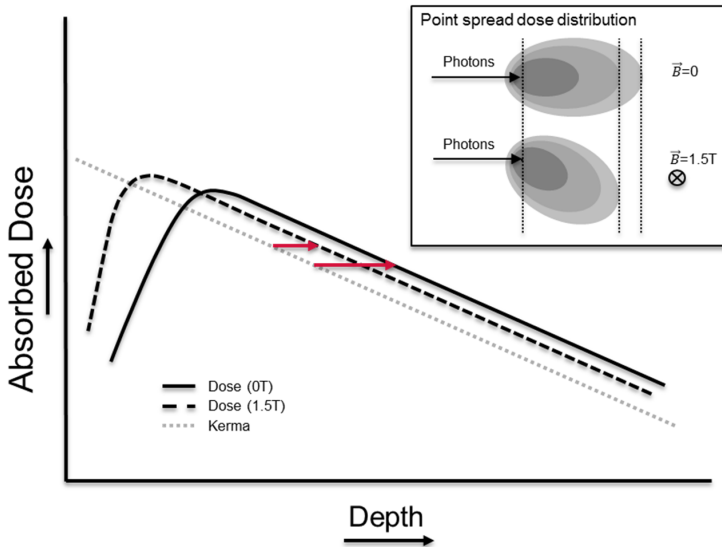


Figure 2.1: A schematic depth dose curve with and without a magnetic field perpendicular to the photon beam and the Kerma in water which is independent of the magnetic field. The arrows indicate the difference in energy deposition relative to the Kerma. To illustrate the change in dose distribution around an interaction point, point spread dose distributions are shown.

Ideally the change in detector reading due to the magnetic field would be proportional to the change in local dose. However, the response of some detectors, such as ionization chambers, may be influenced by the magnetic field. The change in reading depends on the dosimeter used and can be of the order of several percent for air-filled ionization chambers which are commonly used for reference dosimetry. It has been shown by several groups that the raw reading changes in a magnetic field, depending on the magnetic field strength, orientation of the magnetic field relative to the photon beam, chamber type and the orientation of the chamber (Smit *et al.*, 2013; Meijnsing *et al.*, 2009; de Prez *et al.*, 2016b; O'Brien *et al.*, 2016; Wolthaus *et al.*, 2016b; Reynolds *et al.*, 2013; Spindeldreier *et al.*, 2017; Malkov *et al.*, 2018). The chamber reading depends on the average path length of the electrons inside the air-filled cavity, which will be affected by the presence of the magnetic field due to the Lorentz force (Meijnsing *et al.*, 2009). The Lorentz force also affects the local electron fluence in the medium around the chamber, which in turn changes the local dose as described above as well as the inflow of the electrons into the cavity of the chamber. The variation of the electron influx will affect the reading of the ionization chamber (Meijnsing *et al.*, 2009). Currently, no code of practice is yet available for performing reference dosimetry in the presence of a magnetic field and therefore existing protocols have to be adapted. A standard formalism, such as presented in the TRS-398 (Andreo *et al.*, 2000), TG-51 (Almond *et al.*, 1999) and NCS-18 (Aalbers *et al.*, 2008), was adapted by O'Brien *et al.* (2016) according to the formalism presented

by Alfonso *et al.* (2008), which is a formalism for reference dosimetry of small and non-standard radiation fields. The adaptation of O'Brien *et al.* includes a correction of the absorbed dose-to-water coefficient ($N_{D,w}$) in the presence of a magnetic field which was determined by Monte Carlo calculations for several ionization chambers. To accommodate for the magnetic field Malkov *et al.* (2018) used a different approach and adapted the standard formalism by introducing a single correction factor for all changes from the reference conditions. This factor combines the standard beam quality correction and the magnetic field corrections and was determined using Monte Carlo simulations of ionization chambers.

The presented formalism in this paper introduces two correction factors to the existing reference dosimetry formalisms: a correction for the change in dose distribution due to the magnetic field and separately a correction for the change in reading of the ionization chamber. This approach makes a distinction between the different corrections to the dosimetry formalism needed to account for the effects of the magnetic field. Furthermore, the formalism presented here facilitates measurement of the change of reading due to the magnetic field by individual departments and comparison with Monte Carlo simulations of ionization chambers and calorimetry measurements. This approach was used for the clinical introduction of the MRI-Linac at the UMC Utrecht (Raaymakers *et al.*, 2017).

2.2 Formalism

In the existing codes of practice such as e.g. TRS-398 (Andreo *et al.*, 2000), TG-51 (Almond *et al.*, 1999) and NCS-18 (Aalbers *et al.*, 2008) the absorbed dose-to-water is given by

$$D_{w,Q} = M_Q N_{D,w,Q_0} k_{Q,Q_0} \quad (2.1)$$

Where Q is the machine specific beam quality, Q_0 the reference beam quality used for calibration of an ionization chamber, $D_{w,Q}$ is the absorbed dose-to-water at the reference point for beam quality Q , N_{D,w,Q_0} the absorbed dose-to-water calibration coefficient at the reference beam quality, and k_{Q,Q_0} is the beam quality correction factor which corrects for the difference in dose-to-water calibration coefficient between the reference beam quality Q_0 and the beam quality Q . The reading M_Q of the dosimeter corrected for pressure, recombination, polarity, relative humidity and temperature is given by

$$M_Q = M_{\text{raw}} k_{TP} k_h k_{\text{pol}} k_s \quad (2.2)$$

where M_{raw} is the raw dosimeter reading, k_{TP} the factor to correct the response for temperature and pressure, k_h for relative humidity, k_{pol} for polarity effect and k_s for incomplete charge collection due to recombination. The reading is corrected by eq. 2.2

to meet the reference conditions. To determine the dose in the presence of a magnetic field, the standard formalism (eq. 2.1) is adapted by including two factors. First a dose conversion factor to correct for the difference in local dose with and without a magnetic field is added, and secondly a correction to the reading of the detector obtained in the presence of the magnetic field is applied. As explained in the introduction, the absorbed dose-to-water at the reference point in the presence of a magnetic field is different than the dose without a magnetic field. To account for this difference the following dose conversion factor $c_{\vec{B}}$ is introduced;

$$c_{\vec{B}} = \frac{D_{w,Q}^{\vec{B}}}{D_{w,Q}} \quad (2.3)$$

where $D_{w,Q}^{\vec{B}}$ is the absorbed dose-to-water for beam quality Q in a magnetic field \vec{B} at the same reference point as the absorbed dose-to-water without the magnetic field $D_{w,Q}$. Note that the conversion factor accounts for the change of dose deposition in water because of the magnetic field and is therefore dependent on the magnetic field strength and its orientation relative to the photon field. Therefore the magnetic field is denoted as a vector. Note that this conversion factor is independent of the dosimeter. Besides the fact that the change in local dose influences the reading of the ionization chamber, the magnetic field also influences the charge collection directly. Due to the presence of the magnetic field the electron trajectories will change, especially in lower density media such as an air-filled ionization chamber. As a result, the electron fluence inside and just around the chamber, and therefore the raw chamber reading, will change. The Bragg-Gray cavity conditions are therefore no longer valid and the dose-to-water cannot be determined directly from the chamber reading. Therefore a correction factor has to be applied to the chamber reading to take into account this effect. This correction factor $k_{\vec{B},M,Q}$ is defined as

$$k_{\vec{B},M,Q} = \frac{M_Q}{M_Q^{\vec{B}}} \quad (2.4)$$

where M_Q is the corrected raw reading without a magnetic field and $M_Q^{\vec{B}}$ is the corrected raw reading ($M_{\text{raw}}^{\vec{B}}$) obtained in the presence of a magnetic field (eq. 2.2). The standard formalism can be adapted for the influence of the magnetic field using the dose conversion factor $c_{\vec{B}}$ and the correction on the detector reading $k_{\vec{B},M,Q}$. The dose-to-water in the presence of a magnetic field $D_{w,Q}^{\vec{B}}$ is therefore

$$D_{w,Q}^{\vec{B}} = c_{\vec{B}} k_{\vec{B},M,Q} M_Q^{\vec{B}} N_{D,w,Q_0} k_{Q,Q_0} \quad (2.5)$$

Note that if we combine the $k_{\bar{B},M,Q}$ and the $c_{\bar{B}}$ into a single correction factor this results in

$$c_{\bar{B}}k_{\bar{B},M,Q} = \frac{D_{w,Q}^{\bar{B}}M_Q}{D_{w,Q}M_Q^{\bar{B}}} = \frac{N_{D,w,Q}^{\bar{B}}}{N_{D,w,Q}} = k_{\bar{B},Q} \quad (2.6)$$

Where $k_{\bar{B},Q}$ is a modification of the k_{Q,Q_0} factor which takes into account the change in $N_{D,w,Q}$ due to the presence of the magnetic field. The $k_{\bar{B},Q}$ factor was used in the formalism presented by O'Brien *et al.* (2016) and determined by Monte Carlo. It can also be measured using calorimetry (de Prez *et al.*, 2016b). Using the relation above (eq. 2.6) the various methods to determine $k_{\bar{B},Q}$ can be compared. To use the presented formalism to determine the absorbed dose under reference conditions, all factors in eq. 2.5 should be established, including the two factors $k_{\bar{B},M,Q}$ and $c_{\bar{B}}$. The N_{D,w,Q_0} is obtained via standard calibration procedures at a Standard Laboratory. The beam quality, Q , is specified by the tissue phantom ratio $TPR_{20,10}$, which is then used to determine k_{Q,Q_0} (Aalbers *et al.*, 2008; Andreo *et al.*, 2000). The effects of recombination and polarity have to be verified for the specified beam quality in a magnetic field to correct the raw reading (Smit *et al.*, 2013). The $k_{\bar{B},M,Q}$ and $c_{\bar{B}}$ factors are determined for an open beam in a region of transient charged particle equilibrium, i.e. on the central axis at depth below the depth of the dose maximum and the range of contamination electrons. The change in dose-to-water, $c_{\bar{B}}$, is best determined with Monte Carlo simulations of dose distributions in water, since the change in dose due to the magnetic field is small and therefore difficult to measure, and difficult to distinguish from the change in chamber response due to the magnetic fields. Only depth dose curves have to be simulated to determine $c_{\bar{B}}$ and full representation of the detector is not required for these Monte Carlo simulations. Note that $c_{\bar{B}}$ is independent of the detector used. The change in local dose, is however, dependent on the orientations of the magnetic field and photon beam and on the beam energy spectrum. Therefore, $c_{\bar{B}}$ has to be determined for the specific magnetic field orientation and beam quality used. The $k_{\bar{B},M,Q}$ factor can be determined for each detector used for reference dosimetry by measuring the reading with and without a magnetic field. Both the $k_{\bar{B},M,Q}$ and $c_{\bar{B}}$ depend on the orientation of the magnetic field and photon field and on the beam quality, but the $k_{\bar{B},M,Q}$ factor is also specific to the detector design and the relative orientation of the chamber to both the magnetic field and the radiation beam. As a result the $k_{\bar{B},M,Q}$ factor has to be determined for the specific photon beam quality, magnetic field and detector orientation.

2.3 Materials and Methods

2.3.1 MRI-Linac system and reference setup

This formalism was implemented in a protocol for reference dosimetry on the MRI-Linac installed at our department. The MRI-Linac (Elekta AB, Stockholm, Sweden) combines a 1.5 T MRI scanner (Philips Medical Systems, Best, the Netherlands) with a 7 MV linear

accelerator. The magnetic field is directed out of the bore (i.e. along the IEC 1217, -y-axis) and is therefore orthogonal to the beam direction. The source to isocenter distance of this system is 143.5 cm. The beam quality was quantified by the tissue-phantom ratio at depths of 20 and 10 cm ($TPR_{20,10}$), for field size of $10 \times 10 \text{ cm}^2$ (Aalbers *et al.*, 2008) and was determined with and without the magnetic field. For this measurement the ionization chamber was positioned with its stem parallel to the magnetic field at the isocenter in an MRI-compatible version of the MP1 phantom (PTW GmbH, Freiburg, Germany). The MP1 phantom is a cuboid water tank with dimension $37 \times 32 \times 32 \text{ cm}^3$ designed for absolute dose and beam quality measurements. The phantom size meets the requirements of the existing codes of practice on reference dosimetry (Almond *et al.*, 1999; Andreo *et al.*, 2000; Aalbers *et al.*, 2008) For the other measurements and calculations, phantoms were positioned at a source to surface distance of 133.5 cm and a field size of $10 \times 10 \text{ cm}^2$ at isocenter was used. This is considered the reference setup. For the measurements, the orientation of the detector is described in section 2.3.3.

2.3.2 Dose-to-water Monte Carlo calculations

For the calculation of $c_{\vec{B}}$, the GPUMCD Monte Carlo algorithm (Hissoiny *et al.*, 2011a,b) was used to calculate the dose in water with and without magnetic field for the same reference setup. This model was validated against GEANT4 for dose calculation of radiotherapy beams (Ahmad *et al.*, 2016; Hissoiny *et al.*, 2011a). Calculations were performed using the reference setup for a water phantom of $40 \times 40 \times 35 \text{ cm}^3$. The phantom size meets the requirements of the existing codes of practice on reference dosimetry (Almond *et al.*, 1999; Andreo *et al.*, 2000; Aalbers *et al.*, 2008). To illustrate the variation in dose due to the magnetic field, $c_{\vec{B}}$ was calculated for various field strengths of 0, 0.2, 0.35, 0.5, 0.7, 1, 1.2, 1.5, 2 and 3 T. For each magnetic field strength calculations were performed using a 1 mm grid size and a dose uncertainty of 1%. Based on this dose uncertainty the total number of particles is predicted by software to achieve the desired uncertainty in the central high dose region. To further reduce the statistical uncertainty, each depth dose curve was calculated 13 times. Next, the mean depth dose curve along the central axes of these 13 calculations was determined, resulting in one depth dose curve for each magnetic field strength. Subsequently the mean depth dose curves were divided by the 0 T depth dose curve to illustrate the magnetic field effect on the central axis. To determine $c_{\vec{B}}$ the change in dose was determined by calculating the overall mean percentage difference at depths ranging from 6 to 15 cm to further reduce the uncertainty. The percentage difference of the dose for this range is nearly constant (O'Brien *et al.*, 2016). To indicate the uncertainty in the reduction in local dose and in $c_{\vec{B}}$, the standard error of the mean (SEM) was calculated.

2.3.3 Detector response measurements on the MRI-Linac

The measurements for reference dosimetry were performed in a water phantom as described by Smit *et al.* (2013). For the measurements the reference setup was used. The point of measurement was located in the isocenter of the beam (SAD = 143.5 cm) at a depth of 10 cm and 100 MU was delivered for each measurement. The $k_{\vec{B},M,Q}$ was deter-

mined for two ionization chamber orientations and for two different Farmer type waterproof ionization chambers, the PTW 30013 (PTW GmbH, Freiburg Germany) and IBA FC65-G (IBA Dosimetry GmbH, Schwarzenbruck Germany). The chambers were aligned both perpendicular and parallel to the magnetic field and were always perpendicular to the photon field (figure 2.2). To prevent variations in reading due to air around the ionization chamber in the holders of standard solid water dosimetry phantoms, all measurements were performed in water using the waterproof ionization chambers (Hackett *et al.*, 2016; Malkov *et al.*, 2017; O'Brien *et al.*, 2017). Measurements were made with PTW Unidos electrometers (types T10022 and T10009). Measurements were performed before and after multiple ramp up and ramp down sessions of the magnetic field. Readings of the ionization chambers were corrected for temperature and pressure. Other correction factors, like saturation correction, are considered equal with and without the magnetic field (Smit *et al.*, 2013).

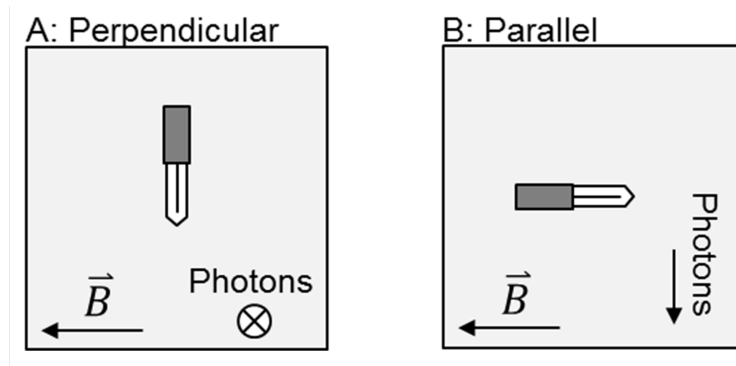


Figure 2.2: Orientation of the ionization chamber relative to the photon field and the magnetic field for the perpendicular and parallel orientation.

In order to position the chambers perpendicular to both the magnetic field and the photon beam (figure 2.2) a $20 \times 20 \times 10$ cm³ water block phantom (phantom T41014, PTW, Freiburg, GmbH, Germany), which accommodates a Farmer sleeve at a fixed depth of 5 cm. The sleeve was perforated to allow water around the ionization chamber. The gantry was rotated to 90 degrees and the water block was put on its side with the opening at the top to prevent water leakage from the phantom. To measure at a depth of 10 cm, 5 cm of RW3 slabs (PTW, Freiburg, GmbH, Germany) were positioned on the side of the phantom through which the beam entered. The measurements in which the ionization chamber was parallel to the magnetic field (figure 2.2) were performed with an MRI compatible version of the MP1 phantom (PTW GmbH, Freiburg, Germany).

2.4 Results

2.4.1 Beam quality

The beam quality measured at the MRI-Linac did not appear to be affected by the magnetic field. The measured $\text{TPR}_{20,10}$ with magnetic field was 0.701 ± 0.002 (1 SD) and 0.700

± 0.002 (1SD) without magnetic field. The parameter $\text{TPR}_{20,10}$ is in general practically independent of the SSD (Khan, 2014), and this was verified for a range of SSDs including the SSD used in these experiments. Since there were no effects of the magnetic field on the beam quality the beam quality dependence k_{Q,Q_0} was determined using a standard code of practice (Aalbers *et al.*, 2008).

2.4.2 Difference in dose to water: $c_{\vec{B}}$

The dose-to-water decreased with increasing magnetic field strength (figure 2.3). For a standard reference field size of $10 \times 10 \text{ cm}^2$ the decrease in dose was $0.51\% \pm 0.03\%$ (1 SEM) at a magnetic field strength of 1.5 T, compared to the same setup without magnetic field. This resulted in a $c_{\vec{B}}$ factor of 0.9949 for that setup.

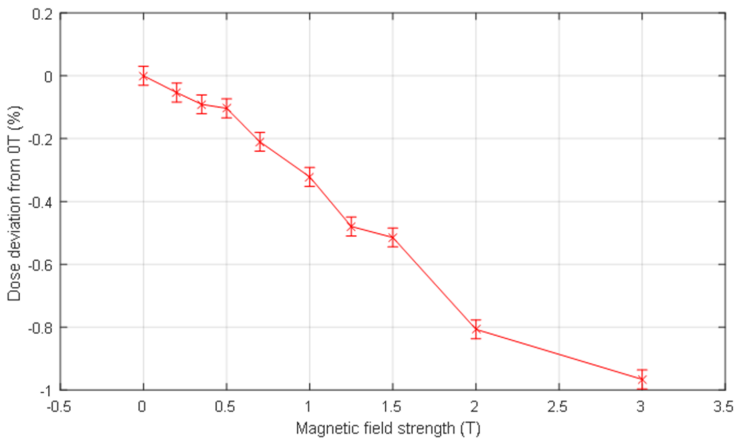


Figure 2.3: The dose deviation for various magnetic field strengths relative to the dose without the presence of the magnetic field. The magnetic field was orientated orthogonal to the photon field axis. Error bars indicate the standard error of the mean.

2.4.3 Measurement of $k_{\vec{B},M,Q}$

The presence of the magnetic field increased the readings of the PTW 30013 and the IBA FC65-G ionization chambers by 3.4% and 4.5% respectively when the ionization chamber was positioned orthogonal to the magnetic field and the photon beam. When the ionization chamber was positioned parallel to the magnetic field and orthogonal to the photon field the reading showed little change ($< 0.3\%$) relative to the reading without a magnetic field. The resulting $k_{\vec{B},M,Q}$ factors are shown in table 2.1.

2.5 Discussion

In this article we propose a formalism for reference dosimetry which can be used for radiotherapy in photon beams in the presence of a magnetic field. The difference to other formalisms is that the effects of the magnetic field on the dose distribution and

Chamber type	$k_{B_{\perp},M,Q}$	n_{\perp}	$k_{B_{\parallel},M,Q}$	n_{\parallel}
PTW 30013	0.967 ± 0.002	5	0.997 ± 0.002	5
IBA FC65-G	0.957 ± 0.002	4	1.002 ± 0.003	5

Table 2.1: The measured $k_{B_{\perp},M,Q}$ and $k_{B_{\parallel},M,Q}$ for two ionization chambers positioned orthogonal and parallel to the magnetic field including the standard error of the mean. Also the number of measurement series, i.e. number of ramp ups and ramp downs of the magnetic field, (n) is given.

on the reading of the dosimeter are taken into account separately. To demonstrate the use of the formalism in a protocol both of the effects are determined for the Elekta MRI-Linac, i.e. with the 1.5 T magnetic field orthogonal to the photon beam and for a nominal beam energy of 7 MV.

The effect of the magnetic field on the absorbed dose at a fixed depth has been determined here for multiple magnetic field strengths. In these simulations, the magnetic field was orthogonal to the photon beam. For this case the electrons released by photon-electron interactions travelled less in the forward direction since the electron paths were curved due to the Lorentz force. Therefore the energy was also released closer to the photon interaction point and the dose downstream decreased. This was especially the case for higher magnetic field strengths. For the same magnetic field orientation and a magnetic field strength of 1.5 T, O'Brien *et al.* (2016) found with Monte Carlo simulation a reduction of $0.5\% \pm 0.1\%$ of the dose-to-water. This result is in good agreement with the results found in this study. In another Monte Carlo study, Spindeldreier *et al.* (2017) reported a reduction in dose of 0.3% for a 1 T magnetic field orientated orthogonal to a 6 MV photon beam, which is also consistent with the data reported in this article.

The change in response of the Farmer chambers due to the influence of the magnetic field was 3.4 to 4.5% for the chamber aligned orthogonal to both the 1.5 T magnetic field and the photon beam. For the chamber aligned with the 1.5 T magnetic field the change in response was small ($<0.3\%$). Similar findings were reported in previous studies (Meijsing *et al.*, 2009; Smit *et al.*, 2013; Reynolds *et al.*, 2013; Spindeldreier *et al.*, 2017). Due to the magnetic field, the path of the high energy electrons in the active volume of the ionization chamber can change and therefore result in more or in fewer ionizations, depending on the relative orientations of the chamber and magnetic field. The influx of these electrons can also change since the magnetic field alters the trajectories of the electrons. The net effect will be specific to the orientation of the chamber relative to the magnetic field and the photon field, and the magnetic field strength.

In order to compare our results to the results of other studies, the $k_{\vec{B},Q}$ factors for this study were also calculated. The $k_{B_{\perp},Q}$ and $k_{B_{\parallel},Q}$ are calculated based on the values of $c_{\vec{B}}$, $k_{B_{\perp},M,Q}$ and $k_{B_{\parallel},M,Q}$ found in this study. The results are listed in table 2.2 together with the published data of other studies.

For the parallel orientation the measurement based $k_{B_{\parallel},Q}$ values determined in this study

Chamber type	Reference		TPR _{20,10}	$k_{B_{\perp},Q}$	$k_{B_{\parallel},Q}$
PTW 30013	UMC Utrecht	M	0.701	0.963(2)	0.992(2)
	de Prez et al. (2016b)	M	0.702	0.961(7)	
	O'Brien et al. (2016)	MC	0.695	0.976(1)	0.994(1)
				0.961(1)*	
	Malkov et al.(2018)	MC	0.695		0.988(1)
	Spindeldreier et al. (2017)	MC	0.674	0.954(3)	0.993(3)
IBA FC65-G	UMC Utrecht	M	0.701	0.952(2)	0.997(3)
	de Prez et al.(2016b)	M	0.702	0.951(7)	
				0.959(3)*	
	Malkov et al.(2018)	MC	0.695		0.992(1)

* Result obtained with chamber in the perpendicular orientation as shown in figure 2.2, but with the magnetic field in the opposite direction.

Table 2.2: The $k_{B_{\perp},Q}$ and $k_{B_{\parallel},Q}$ of the UMC Utrecht data compared with the reported data in the literature based on measurements (M) and Monte Carlo (MC) calculations for two ionization chamber models. Uncertainties are shown between brackets as the least significant digit of the reported value. All uncertainties are of Type A, i.e. based on statistical methods only, except for de Prez et al., which includes Type B errors as well.

are well in agreement ($< 0.5\%$) with the Monte Carlo based studies for both the PTW chamber (O'Brien *et al.*, 2016; Spindeldreier *et al.*, 2017; Malkov *et al.*, 2018) and the IBA chamber (Malkov *et al.*, 2018). Furthermore, the correction needed for the parallel orientation of the ionization chamber is smaller than that for the perpendicular orientation. For chambers in the perpendicular orientation, the results are in good agreement (0.2% difference) with the results of de Prez *et al.* (2016b), who measured the $k_{B_{\perp},Q}$ factor directly in a magnetic field using a calorimeter (de Prez *et al.*, 2016a) for both ionization chambers. The $k_{B_{\perp},Q}$ factor was also calculated using Monte Carlo for the PTW chamber. The variation between the $k_{B_{\perp},Q}$ values in these studies and the measurement-based $k_{B_{\perp},Q}$ values is, however, larger than the variation found for the parallel orientation. Also, the measurement-based $k_{B_{\perp},Q}$ values are closer to the $k_{B_{\perp},Q}$ values calculated with the magnetic field in the opposite direction. Furthermore, the effect of the magnetic field orientation when the chamber is perpendicularly oriented to the magnetic field is much larger, and in the opposite direction, in the study of O'Brien *et al.* than in the study of Spindeldreier *et al.* The influence of the magnetic field on ionization chamber measurements may be more difficult to accurately simulate with Monte Carlo, and therefore the parallel orientation is more preferable for reference dosimetry. The effective sensitive volume has an important impact on the chamber response in Monte Carlo simulations (Malkov *et al.*, 2017, 2018; Spindeldreier *et al.*, 2017). The charge collecting electric field inside the chamber can be distorted, especially near the guard electrode, and charge released in this volume may not be collected. The influence of the effective sensitive volume on the change of chamber response due to the magnetic field depends on the orientation of the magnetic field, photon beam and chamber.

In the proposed formalism, the effect of the magnetic field on the dose distribution and

on the reading of the dosimeter are taken into account as two distinct factors, $c_{\bar{B}}$ and $k_{\bar{B},M,Q}$. O'Brien *et al.* (2016) presented a different formalism using $k_{\bar{B},Q}$ as a correction of the $N_{D,w,Q}$ factor to determine the dose in presence of a magnetic field. Malkov *et al.* (2018) used another approach, which combines the standard beam quality correction and the magnetic field corrections in a single factor to directly correct the N_{D,w,Q_0} , calibration factor, i.e. a correction of the absorbed dose-to-water coefficient for the reference beam quality. The factors used by O'Brien *et al.* and Malkov *et al.* can only be determined directly by primary absorbed dose to water standards, such as e.g. calorimeters (de Prez *et al.*, 2016a), or by Monte Carlo simulations of the ionization chamber used for reference dosimetry. Absorbed dose to water primary standards which can operate in a magnetic field are, however, not widely available. Detailed Monte Carlo simulations have been performed only for specific models of ionization chambers and variations between chambers of the same type have not yet been investigated. Furthermore, Monte Carlo simulations have to be verified against measurements, for example to incorporate the influence of the effective sensitive volume. The proposed formalism enables radiotherapy departments to determine the correction factors required for reference dosimetry in a magnetic field, by separating the effects on the dose distribution and the response of the chamber. The $c_{\bar{B}}$ factor can be determined by Monte Carlo simulation of dose distributions in water. As only the change in local dose has been determined, the details of the ionization chamber are not necessary, which simplifies the simulations. The change in detector reading due to the magnetic field, $k_{\bar{B},M,Q}$, can be determined relatively easily from measurements for any detector and for all orientations during ramp-up or ramp-down procedures. The advantage is that this measurement in principle can be performed at a department during for example a ramp up procedure at the time of installation. The proposed formalism would therefore also be useful for detector development since the correction factors can be determined locally. Finally the presented formalism can be used to independently verify $k_{\bar{B},Q}$ factors that are determined from calorimetry measurements or Monte Carlo simulations.

2.6 Conclusion

A new formalism is proposed for reference dosimetry in the presence of magnetic fields. In this formalism the effect of the magnetic field on the dose distribution and the detector reading are separated. The measurements can be performed by individual departments and the formalism can be used to determine the correction factors needed to establish the absorbed dose in a magnetic field. This protocol was implemented for clinical use at our department.

2.7 Acknowledgments

This work was partially funded by EURAMET through EMPIR grant 15HLT08 MRgRT.

CHAPTER 3

Consistency of PTW30013 and FC65-G ion chamber magnetic field correction factors

The following chapter is based on:

Woodings S.J., van Asselen B., van Soest T.L., de Prez L.A., Lagendijk J.J.W., Raaymakers B.W. and Wolthaus J.W.H. 2019 Technical note: Consistency of PTW30013 and FC65-G ion chamber magnetic field correction factors *Medical Physics* 46 3739–3745

Abstract

Purpose: Reference dosimetry in a strong magnetic field is made more complex due to (i) the change in dose deposition and (ii) the change in sensitivity of the detector. Potentially it is also influenced by thin air layers, interfaces between media, relative orientations of field, chamber and radiation, and minor variations in ion chamber stem or electrode construction.

The PTW30013 and IBA FC65-G detectors are waterproof Farmer-type ion chambers that are suitable for reference dosimetry. The magnetic field correction factors have previously been determined for these chamber types.

The aim of this study was to assess the chamber-to-chamber variation and determine whether generic chamber type-specific magnetic field correction factors can be applied for each of the PTW30013 and FC65-G type ion chambers when they are oriented anti-parallel (\parallel) to, or perpendicular (\perp) to, the magnetic field.

Methods: The experiment was conducted with twelve PTW30013 and thirteen FC65-G chambers. The magnetic field correction factors were measured using a practical method. In this study each chamber was cross-calibrated against the local standard chamber twice; with and without magnetic field. Measurements with 1.5 T magnetic field were performed with the 7 MV FFF beam of the MRI-linac. Measurements without magnetic field (0 T) were performed with the 6 MV conventional beam of an Elekta Agility linac.

A prototype MR-compatible PTW MP1 phantom was used along with a prototype holder that facilitated measurements with the chamber aligned 90° counter-clockwise (\perp) and 180° (\parallel) to the direction of the magnetic field. A monitor chamber was also mounted on the holder and all measurements were normalized so that the effect of variations in the output of each linac were minimized.

Measurements with the local standard chamber were repeated during the experiment to quantify the experimental uncertainty.

Recombination was measured in the 6 MV beam. Beam quality correction factors were applied. Differences in recombination and beam quality between beams are constant within each chamber type.

By comparing the results for the two cross calibrations the magnetic field correction factors can be determined for each chamber, and the variation within the chamber-type determined.

Results: The magnetic field correction factors within both PTW30013 and FC65-G chamber-types were found to be very consistent, with observed standard deviations for the PTW30013 of 0.19% (\parallel) and 0.13% (\perp), and for the FC65-G of 0.15% (\parallel) and 0.17% (\perp). These variations are comparable with the standard uncertainty ($k = 1$) of 0.24%.

Conclusion: The consistency of the results for the PTW30013 and FC65-G chambers implies that it is not necessary to derive a new factor for every new PTW30013 or FC65-G chamber. Values for each chamber-type (with careful attention to beam energy, magnetic field strength and beam-field-chamber orientations) can be applied from the literature.

3.1 Introduction

Elekta AB (Stockholm, Sweden), Philips (Best, The Netherlands) and University Medical Center Utrecht have developed a linear accelerator (linac) with integrated 1.5 T magnetic resonance imaging (MRI). This combination facilitates simultaneous irradiation and high-precision image guidance with soft-tissue contrast (Legendijk *et al.*, 2014). The Elekta Unity MRI-linac is an upgraded version of the machine described by Raaymakers *et al.* (2009). The magnetic field (B) points out of the entrance of the bore, and is at all times at 90° to the central axis of the radiation beam delivered from the linac mounted on its ring gantry.

The magnetic field affects the dose deposition within a phantom and patient within the MRI-linac. The Lorentz force acts on charged particles, pulling them in a direction orthogonal to their motion and the magnetic field, which perturbs the dose deposition kernel (Raaijmakers *et al.*, 2005). The Lorentz force affects the trajectories of charged particles into, and within, a radiation detector. In addition, seemingly incidental environmental conditions such as thin air layers around the outside of an ion chamber or minor variations in ion chamber stem or electrode construction, may also make significant changes to ion chamber readings (Hackett *et al.*, 2016). Previously the performance of Farmer-type chambers have been investigated and their feasibility confirmed (Meijsing *et al.*, 2009; O'Brien *et al.*, 2016; Reynolds *et al.*, 2013; Smit *et al.*, 2013).

Calibration of the output of a linac beam requires accurate measurement of absorbed dose to water. National and international codes of practice specify what equipment should be used and how these measurements should be performed (Aalbers *et al.*, 2008; Almond *et al.*, 1999; McEwen *et al.*, 2014; Andreo *et al.*, 2000). Dosimetry on a clinical system must be traceable to an internationally-accepted primary standard. Dosimetry factors for the local standard are usually transferred to field detectors through cross-calibration. For the MRI-linac additional factor(s) are required due to the magnetic field. Various definitions and values of the magnetic field correction factor have been published (O'Brien *et al.*, 2016; de Prez *et al.*, 2018; Malkov *et al.*, 2017; Spindeldreier *et al.*, 2017; van Asselen *et al.*, 2018). Measuring the magnetic field correction factor for an individual chamber is a non-trivial activity involving high-precision measurements with and without magnetic field, and potentially with multiple relative orientations of radiation beam, magnetic field and ion chamber. If it can be established that there is little intra-chamber-type variation, then generic chamber-type values from the literature, or in the future from a code of practice, can be reliably used in the clinic.

The aim of this study was to assess the chamber-to-chamber variation of the magnetic field correction factors and determine whether generic chamber type-specific values can be applied for each of the PTW30013 and FC65-G -type ion chambers when they are oriented anti-parallel (\parallel) to, and perpendicular (\perp) to, the magnetic field.

3.2 Theory

Two cross-calibrations can be performed, one with and one without magnetic field, so that the magnetic field correction factor can be determined.

The Dutch code of practice for reference dosimetry (NCS 18) (Aalbers *et al.*, 2008), consistent with AAPM 51 (Almond *et al.*, 1999; McEwen *et al.*, 2014) and IAEA TRS 398 (Andreo *et al.*, 2000), describes the calculation of dose to water from a megavoltage photon beam of quality Q as:

$$D_{w,Q} = M_Q \cdot N_{D,w,Q_0} \cdot k_{Q,Q_0} \quad (3.1)$$

where M_Q is the ion chamber reading corrected for influence quantities such as recombination, polarity, temperature and pressure, N_{D,w,Q_0} is the absorbed dose to water calibration coefficient for the ion chamber at beam quality Q_0 and k_{Q,Q_0} is the beam quality correction factor.

Within a strong magnetic field, the charged particles follow curved trajectories in the medium, and into and within the chamber, and thus the relationship between charge collected within the ion chamber and dose deposited in water is also dependent upon B and the relative orientations of magnetic field, radiation beam and chamber.

This effect can be incorporated into the reference dosimetry in a number of ways (O'Brien *et al.*, 2016; de Prez *et al.*, 2016b; van Asselen *et al.*, 2018), which are all consistent with:

$$D_{w,Q,B} = M_{Q,B} \cdot N_{D,w,Q_0} \cdot k_{Q,Q_0} \cdot k_B \quad (3.2)$$

The cross calibration (in a magnetic field) of a field ion chamber to the local standard ion chamber is based on the equality of absorbed dose at the dosimetric reference point:

$$N_{D,w,Q_0}^{\text{field}} \cdot k_{Q,Q_0}^{\text{field}} \cdot k_B^{\text{field}} = N_{D,w,Q_0}^{\text{ref}} \cdot k_{Q,Q_0}^{\text{ref}} \cdot k_B^{\text{ref}} \cdot \frac{M_{Q,B}^{\text{ref}}}{M_{Q,B}^{\text{field}}} \quad (3.3)$$

In general, generic k_{Q,Q_0} factors would be used from the standard code of practice, although some centers may have chamber-specific k_{Q,Q_0} factors from primary standards laboratories that offer calibrations with beams other than Co-60.

If a cross-calibration is also performed with $B = 0$ T (on an Elekta Agility linac in this study), then the magnetic field correction factor can be determined from the combination of cross calibrations with beam quality Q_1 and field $B = 0$ T, and beam quality Q_2 and field

$B = 1.5$ T, along with the known magnetic field correction factor of the local standard chamber.

$$k_B^{\text{field}} = k_B^{\text{ref}} \cdot \frac{M_{Q_2,B}^{\text{ref}}}{M_{Q_2,B}^{\text{field}}} \cdot \frac{k_{Q_2,Q_0}^{\text{ref}}}{k_{Q_2,Q_0}^{\text{field}}} \cdot \frac{M_{Q_1}^{\text{field}}}{M_{Q_1}^{\text{ref}}} \cdot \frac{k_{Q_1,Q_0}^{\text{field}}}{k_{Q_1,Q_0}^{\text{ref}}} \quad (3.4)$$

It has been shown previously that generic k_{Q,Q_0} factors are applicable for these chamber types (McEwen, 2010). If generic k_{Q,Q_0} factors are used and a comparison is made between chambers that are all of the same type, then the ratios of k_{Q,Q_0} are all constants and have no effect on the distribution of k_B^{field} values. The k_B^{ref} is also unchanging throughout the experiment. Thus the distribution of k_B^{field} factors is influenced only by the ratios of the readings $(M_{Q_2,B}^{\text{ref}}/M_{Q_2,B}^{\text{field}}) \cdot (M_{Q_1}^{\text{field}}/M_{Q_1}^{\text{ref}})$.

3.3 Materials and Methods

3.3.1 Equipment

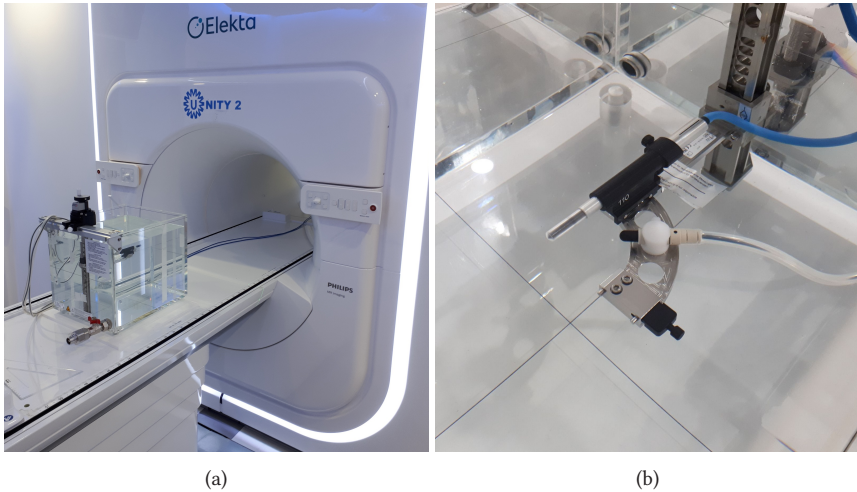


Figure 3.1: (a) PTW prototype MR-compatible MP1 waterphantom at the MRI-linac and (b) prototype holder, with PTW30013 chamber and CC13 monitor chamber.

For the most accurate and traceable results, measurements must be made in water (Hackett *et al.*, 2016; Aalbers *et al.*, 2008; Andreo *et al.*, 2000). A PTW MP1 waterphantom with prototype MR-compatible 1D manual drive and prototype Trufix BS right-angled holder were used (PTW GmbH, Freiberg Germany). The setup is shown in figure 3.1.

Irradiation with $B = 1.5$ T was delivered with an Elekta Unity MRI-linac using a 7 MV, flattening filter free, $10 \times 10 \text{ cm}^2$, 100 MU beam at ~ 430 MU/min with pulse repetition frequency (PRF) 275 Hz, gun duty cycle 71% and gantry 0° (beam quality Q_2). The position of the chamber was assessed, adjusted and verified using the rigid on-gantry MV

imager, such that the center of the chamber was at isocenter. The surface-axis distance (SAD) of this system is 143.5 cm. The water level was then set to 10.0 cm above this point (SSD 133.5 cm). The linac was calibrated to deliver 0.720 cGy/MU under these conditions.

Irradiation with $B = 0$ T was delivered with a clinical Elekta Agility linac using a 6 MV, conventional flat, 10×10 cm², 100 MU beam at ~ 500 MU/min with PRF 400 Hz, gun duty cycle 100% and gantry 0° (beam quality Q_1). The linac was calibrated to deliver 0.671 cGy/MU from this beam with SSD 100 cm and depth 10.0 cm, equivalent to ~ 0.81 cGy/MU under the conditions of this experiment (SSD 90.0 cm, depth 10.0 cm). For the Agility linac, the first chamber was setup with its center at isocentre using the room lasers, whose accuracy was previously confirmed through the standard departmental QA program. It is noted that, using another linac, it was not possible to exactly match the Unity beam quality and dose-per-pulse, but that the two inter-comparisons were independent and therefore it was not critical that the conditions be perfectly matched.

Twelve PTW30013 ion chambers (serial numbers 5555, 5556, 5557, 5593, 5679, 5703, 5949, 5951, 5974, 5975, 8377 and 9627) were sourced from PTW and UMC Utrecht. Thirteen FC65-G ion chambers (serial numbers 3642, 4077, 4081, 4082, 4083, 4090, 4091, 4092, 4093, 4095, 4096, 4097, 4098) were sourced from IBA and UMC Utrecht. In each case the construction of the set of chambers spanned more than one year. The chambers were inspected visually and via 70 kVp x-rays for any damage or faults in their electrodes or stems.

3.3.2 Measurements

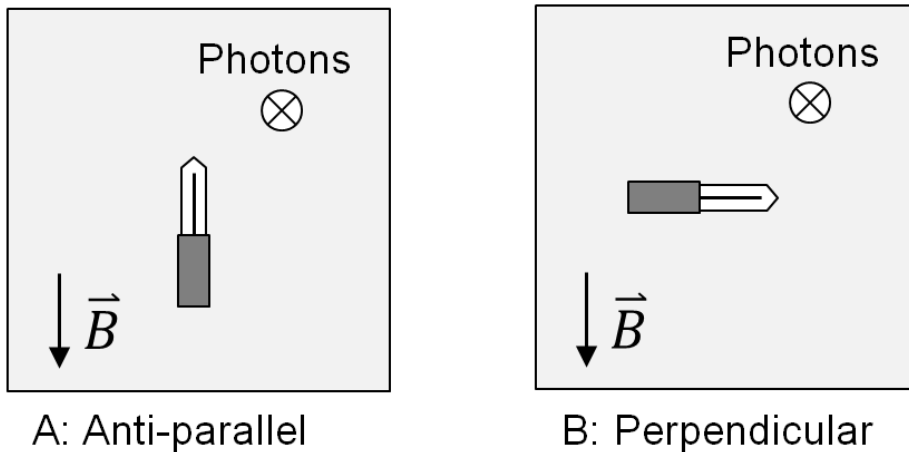


Figure 3.2: Gantry 0° beam's-eye-views of the relative orientations of ion chamber, magnetic field and beam direction for (A) antiparallel and (B) perpendicular (90° counter-clockwise) orientations.

Each time a new chamber was inserted the drive was left at the position corresponding

to 10.0 cm above isocentre and the water level was checked against the center of the ion chamber by viewing the chamber and its reflection from just underneath the water surface, as per the method of TG-106 (Das *et al.*, 2008). This ensured that each chamber was placed as close to 10.0 cm depth as possible. In order to swap a chamber on the MRI-linac, the table was withdrawn from the bore. On the Agility the table and phantom were never moved.

A single CC13 ion chamber (SN 5889, IBA-Dosimetry, Schwarzenbruck Germany) was used as a monitor chamber throughout the experiment. The CC13 was mounted in a custom attachment on the same holder as the field chamber (see figure 3.1). The CC13 was connected to a PTW UnidosE T10009 electrometer with settings -250 V and medium range.

Each field ion chamber was pre-irradiated with 400 MU and the collection voltage was applied for at least three minutes prior to nulling the chamber. Leakage was assessed over 30 seconds and initial measurements were monitored for drift. Measurements in the magnetic field were made with antiparallel (180°) and perpendicular (90° counter-clockwise) orientation (see figure 3.2), and with -250 V collecting potential. On the Agility linac, measurements were only made in one orientation (antiparallel) because the chamber sensitivity does not change with orientation since there is no magnetic field. Measurements were made with -250 V, -50 V and +250 V collecting potential in order to determine the recombination correction k_s and the polarity correction k_{pol} for each chamber. This was done to ensure that none of the chambers demonstrated unusual recombination or polarity behavior. At least 5 readings were made for each of the -250 V cross-calibration conditions and at least 3 readings for the other voltages. Measurements were performed with a PTW UnidosE T10009 electrometer.

Recombination and polarity corrections do not depend on magnetic field and therefore the same values can be used for beams with and without magnetic field (Smit *et al.*, 2013). Recombination does depend on dose per pulse which was 0.026 cGy/pulse for the MRI-Linac and 0.017 cGy/pulse for the Agility. However the same relative change applies for both the local standard and field chambers and the ratios cancel out. This cancellation also applies for the volume averaging effect because, although the 7 MV FFF MRI-linac and the 6 MV conventional Agility beams have different spatial dose distributions in the chamber volume, the differences apply equally to the local standard chamber and the field chamber.

Measurements were made with the local standard FC65-G ion chamber SN 3129 at the beginning of each experiment. The -250 V measurements were repeated during the middle and at the end of each session.

3.3.3 Analysis

Each field chamber reading was normalized by the CC13 chamber reading in order to minimize the effect of any variations in the outputs of the linacs, as well as temperature

and pressure variations.

The recombination correction was calculated using the two-voltage method as recommended by NCS 18 (Aalbers *et al.*, 2008) and IAEA TRS 398 (Andreo *et al.*, 2000). The validity of this method in a 1.5 T MRI-linac has been previously established via a Jaffé plot ($1/Q$ versus $1/V$) (Smit *et al.*, 2013). This was repeated for PTW30013 chamber and FC65-G chambers, which demonstrated linear behaviour over (at least) the range 30 – 300 V (data not shown).

The polarity correction was calculated using the standard method (Aalbers *et al.*, 2008; Andreo *et al.*, 2000).

The local standard chamber absorbed dose to water calibration coefficient, $N_{D,w,Q_0} = 4.827$ cGy/nC, is traceable to (internationally accepted) primary measurement standards at the Dutch primary standards laboratory VSL (12 March 2018). The local standard chamber magnetic field correction factors, $k_{B\parallel} = 1.0011$ and $k_{B\perp} = 0.9553$, were determined previously by measurement on the Elekta Unity MRI-linac with and without magnetic field (UMCU, 14 April 2018) using the method of van Asselen *et al.* (2018).

Generic beam quality correction factors (k_{Q,Q_0}) were determined for each chamber type from IAEA TRS 398 (Andreo *et al.*, 2000) using the measured Unity MRI-linac and Agility linac TPR_{20,10} values of 0.709 and 0.681 respectively.

The multiple FC65-G local standard measurements were used to assess the reproducibility of the experiment for a single chamber over the whole period. The field chamber results were calculated from the average local standard chamber measurements for each experiment.

For each PTW30013 and FC65-G chamber, the k_B was calculated directly using equation 3.4. The inter-chamber (intra chamber-type) standard deviation of k_B was calculated, and evaluated against the calculated uncertainties of the experiment.

3.4 Results and discussion

No damage or faults in the electrodes or stem of each chamber were observed during visual and x-ray inspection of the chambers.

	$k_{B\parallel}$		$k_{B\perp}$	
	PTW30013	FC65-G	PTW30013	FC65-G
average	0.990	1.000	0.961	0.956
standard deviation (%)	0.19%	0.15%	0.13%	0.17%

Table 3.1: Averages and standard deviations of k_B for PTW30013 and FC65-G chamber-types.

Local standard chamber readings, corrected for the CC13 chamber, should be constant throughout the four experiment sessions. The standard deviations of the local standard

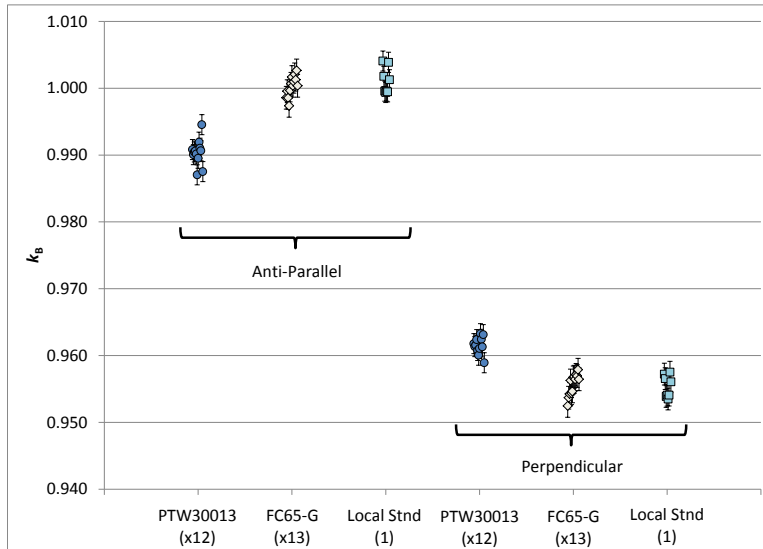


Figure 3.3: Magnetic field correction factors (k_B) for all of the PTW30013 (circles) and FC65-G (diamonds) chambers in both parallel and perpendicular orientations. Within each chamber type and orientation, the results are very consistent. For comparison, the results of repeated measurements of a single local standard chamber are shown (squares). The variation in each set of chambers is no greater than the variation in measurements of a single chamber.

chamber measurements were 0.11% and 0.10% (1.5 T), and 0.10% and 0.14% (0 T).

In this experiment there were several contributions to positional uncertainty. The reproducibility of chamber positioning depended on (i) the trufix BS holder (maximum measured difference 0.01 cm), (ii) the MP1 manual drive accuracy (maximum measured difference 0.01 cm) and (iii) the MRL table longitudinal accuracy (maximum measured difference 0.02 cm). Each time a new chamber was inserted any adjustment in water level was 0.02 cm or less.

Use of the CC13 monitor chamber on the same chamber holder as the field instruments meant that the CC13 chamber was subject to the same environmental conditions, with the potential exception of a small temperature gradient in the water. It also meant that, to first order, any residual error in holder depth would be cancelled out. Disadvantages included that (i) the chamber is smaller and therefore has lower signal-to-noise than a Farmer-type chamber and (ii) that it was placed approximately 3 cm off axis, which is in a dose gradient of 0.03%/cm in the FFF beam and could potentially transfer positional uncertainty into dosimetric uncertainty.

The statistical uncertainties (Type A) in the uncertainty budget for the distribution of magnetic field correction factors (table 3.2) come from the standard deviations of the repeated local standard chamber measurements (R_Q). Thus these include the positioning uncertainties. All of the other entries are of type B, ie based on calculations and estimates. Most are consistent with those of McEwen (2010) and de Prez *et al.* (2018). Uncertainties in variation of chamber angle and the difference in volume averaging are negligible. Uncertainty in k_B^{ref} has no impact on the distribution of k_B^{field} values, as k_B^{ref} remains unchanged throughout, but it does affect the uncertainty of the final k_B^{field} values. The recombination depends mostly on dose per pulse and varies little within a chamber type. Polarity varies little within chamber type. When applying generic k_Q factors from the codes of practice, the corrections are considered type-specific rather than chamber specific. Here we consider ratios of these correction factors, limited within the same chamber-type and for similar beam qualities (Q_1 and Q_2) with similar dose per pulse. Thus the uncertainties in ratios of recombination, polarity and beam quality for the same chamber type are expected to be small. In table 3.2, estimates of these uncertainties are given on the basis of measured uncertainties in k_s , k_{pol} and k_Q (de Prez *et al.*, 2018; McEwen, 2010).

Variable	Type	Agility	Unity
		$B = 0 \text{ T}$ Q_1	$B = 1.5 \text{ T}$ Q_2
R_Q (nC/MU)	A	0.14%	0.11%
Recombination ($k_{s,Q1}^{\text{field1}} / (k_{s,Q1}^{\text{field2}}) \times (k_{s,Q2}^{\text{field2}} / (k_{s,Q2}^{\text{field1}})$)	B	<0.05%	<0.05%
Polarity ($k_{\text{pol},Q1}^{\text{field1}} / (k_{\text{pol},Q1}^{\text{field2}}) \times (k_{\text{pol},Q2}^{\text{field2}} / (k_{\text{pol},Q2}^{\text{field1}})$)	B	<0.05%	<0.05%
Ratios of k_{PT} and humidity correction	B	0.03%	0.03%
Ratio $k_{Q2,Q1}^{\text{field2}} \times k_{Q1,Q2}^{\text{field1}}$	B		<0.12%
Combined standard uncertainty ($k = 1$) in $k_B^{\text{field1}} / k_B^{\text{field2}}$			0.24%

Table 3.2: Uncertainty budget (with coverage factor $k = 1$) in distribution of magnetic field correction factors represented by the uncertainty in $k_B^{\text{field1}} / k_B^{\text{field2}}$.

The k_B results for the twelve PTW30013 chambers and the thirteen FC65-G chambers are shown in figure 3.3 and summarized in table 3.1.

The goal of this study was to assess the standard deviations of the magnetic field correction factors for the two chamber types to determine if type-specific generic k_B values are valid. Thus the key results in table 3.1 are the standard deviations for k_B : 0.19% (\parallel) and 0.13% (\perp) for the PTW30013 and 0.15% (\parallel) and 0.17% (\perp) for the FC65-G. These values are all less than the standard uncertainty of 0.24% calculated in the uncertainty budget. Thus the observed distributions of magnetic field correction factors for the PTW30013 and FC65-G chambers are equivalent to the variation expected due to measurement uncertainty. This implies that it is valid to use a generic chamber-type magnetic field correction factor for either of these chamber types used in a specific field-beam-chamber orientation.

The k_B factors for each of the PTW30013 and FC65-G chambers were determined from an existing k_B for the local standard chamber. The average results for PTW30013 were $k_{B_{\parallel}} = 0.990$ and $k_{B_{\perp}} = 0.961$ and for FC65-G $k_{B_{\parallel}} = 1.000$ and $k_{B_{\perp}} = 0.956$, all ± 0.004 ($k = 1$). The uncertainty in these values is greater because they include the uncertainty of 0.28% ($k = 1$) in the local standard chamber factor k_B^{ref} .

It may also be useful to compare between the magnetic field correction factors in the two directions. The ratios of $k_{B_{\parallel}} / k_{B_{\perp}}$ are 1.030 ± 0.001 for PTW 30013 and 1.047 ± 0.001 for FC65-G. The $k_{B_{\parallel}}$ and $k_{B_{\perp}}$ measurements are correlated for each chamber type (Pearson correlation coefficient $r = 0.88$ for PTW30013 and 0.65 for FC65-G). The parallel and perpendicular measurements were acquired consecutively without making any adjustments to depth or water level, therefore it is not a surprise that the observed standard uncertainties ($k = 1$) are smaller for the ratios $k_{B_{\parallel}} / k_{B_{\perp}}$. This result implies that if the k_B values for an individual chamber are desired, it is sufficient to check the individual chamber in only one orientation.

Chamber type	Reference	$k_{B_{\parallel}}$	$k_{B_{\perp}}$
PTW30013	This study	0.990 ± 0.004	0.961 ± 0.004
	van Asselen	0.992 ± 0.002	0.963 ± 0.002
FC65-G	This study	1.000 ± 0.004	0.956 ± 0.004
	van Asselen	0.997 ± 0.003	0.952 ± 0.002

Table 3.3: Comparison of results from this study (combined standard uncertainties $k = 1$) with those from van Asselen et al. (type A standard uncertainties). Results are consistent.

The k_B results in this study are based on measurements that are entirely separate from, but consistent with, previously published results shown in table 3.3 (van Asselen *et al.*, 2018). The van Asselen et al. results were derived from a smaller number of chambers, but with multiple magnetic field ramp ups and ramp downs. Thus they are likely to have a smaller systematic error in k_B than the results presented here. van Asselen et al. also contains comparisons to results from Monte Carlo based studies which are broadly consistent.

The variation in the measured magnetic field correction factors is approximately the same for both anti-parallel and perpendicular orientations. Nevertheless, the anti-parallel factors are relatively close to unity (ie minimal perturbation) and therefore the parallel orientation is preferable to the perpendicular orientation. In addition the parallel and anti-parallel orientations can be more easily used for beams from different gantry angles and thus this setup is more practical for other dosimetry purposes (eg treatment plan QA).

The recombination and polarity corrections were almost identical within both chamber types. For the PTW30013 chambers $k_s = 1.003$ (σ 0.01%) and $k_{pol} = 0.999$ (σ 0.02%). For the FC65-G chambers $k_s = 1.004$ (σ 0.02%) and $k_{pol} = 1.000$ (σ 0.03%). The derived N_{D,w,Q_0} factors had standard deviations of 0.31% (PTW30013) and 0.32% (FC65-G). As a consistency check the values derived here for the three UMCU chambers were compared

to their previous values. The new N_{D,w,Q_0} factors were different by -0.03%, +0.05% and -0.20%.

It has been noted in the literature (McEwen, 2010; de Prez *et al.*, 2018) that differences of up to 0.4% exist at 6 – 7 MV in estimates of generic (chamber-type) k_{Q,Q_0} factors between direct measurements (eg NCS 18 (Aalbers *et al.*, 2008)) and generic-type calculations (eg IAEA TRS 398 (Andreo *et al.*, 2000)). This can affect calculations of cross-calibration parameters such as N_{D,w,Q_0} . However the method of deriving magnetic field correction factors used here is insensitive to k_{Q,Q_0} values as the ratios largely cancel.

The effective point of measurement (EPoM) of the Farmer-type ion chamber is shifted laterally and vertically due to the spiraling trajectories of the electrons. The combination of electric and magnetic fields also creates non-uniform sensitivity within the nominal chamber volume (Malkov *et al.*, 2017; O'Brien *et al.*, 2018). The k_B factor includes the effect of the change in EPoM due to the magnetic field.

3.5 Conclusion

The goal of this study was to assess the consistency of magnetic field correction factors within the PTW30013-type and FC65-G-type ion chambers. The factors were found to be very consistent, with observed standard deviations of $\sigma = 0.13\% - 0.19\%$, which were within the standard measurement uncertainty of 0.24% ($k = 1$) from the uncertainty budget. These results indicate that it is not necessary to derive a new factor for every new PTW30013 or FC65-G chamber, but that average values for each chamber-type (with careful attention to beam energy, magnetic field strength and beam-field-chamber orientations) can be applied from the literature.

3.6 Acknowledgments

This project has received funding from the EMPIR programme, grant 15HLT08 ‘Metrology for MR guided Radiotherapy’, co-financed by the Participating States and from the European Union’s Horizon 2020 research and innovation programme.

Our thanks to PTW for the loan of ten PTW30013 ion chambers and to IBA for the loan of twelve FC65-G ion chambers.

CHAPTER 4

Performance of a PTW 60019 microDiamond detector in a 1.5 T MRI-linac.

The following chapter is based on:

Woodings S.J., Wolthaus J.W.H., van Asselen B., de Vries J.H.W., Kok J.G.M., Lagendijk J.J.W. and Raaymakers B.W. 2018b Performance of a PTW 60019 microDiamond detector in a 1.5 T MRI-linac *Physics in Medicine and Biology* 63 05NT04

Abstract

Accurate small-field dosimetry is critical for a magnetic resonance linac (MRI-linac). The PTW 60019 microDiamond is close to an ideal detector for small field dosimetry due to its small physical size, high signal-to-noise ratio and approximate water equivalence. It is important to fully characterise the performance of the detector in a 1.5 T magnetic field prior to its use for MRI-linac commissioning and quality assurance.

Standard techniques of detector testing have been implemented, or adapted where necessary to suit the capabilities of the MRI-linac. Detector warmup, constancy, dose linearity, dose rate linearity, field size dependence and leakage were within tolerance. Measurements with the detector were consistent with ion chamber measurements for medium sized fields. The effective point of measurement of the detector when used within a 1.5 T magnetic field was determined to be 0.80 ± 0.23 mm below the top surface of the device, consistent with the existing vendor recommendation and alignment mark at 1.0 mm. The angular dependence was assessed. Variations of up to 9.7% were observed, which are significantly greater than in a 0 T environment. Within the expected range of use, the maximum effect is approximately 0.6% which is within tolerance. However for large beams within a magnetic field, the divergence and consequent variation in angle of photon incidence means that the microDiamond would not be ideal for characterising the profiles and it would not be suitable for determining large-field beam parameters such as symmetry. It would also require a correction factor prior to use for patient-specific QA measurements where radiation is delivered from different gantry angles.

The results of this study demonstrate that the PTW 60019 microDiamond detector is suitable for measuring small radiation fields within a 1.5 T magnetic field and thus is suitable for use in MRI-linac commissioning and quality assurance.

4.1 Introduction

The 1.5 T MRI-linac at the University Medical Center Utrecht has been developed as part of a collaboration with Elekta AB (Stockholm, Sweden) and Philips (Best, The Netherlands) and is an upgraded version of the machine described by Raaymakers *et al.* (2009). The 1.5 T magnetic field is parallel to the bore (IEC 61217 -y direction), and is at all times at 90 degrees to the 7 MV FFF radiation beam delivered from the linac mounted on its ring gantry.

The magnetic field affects the dose deposition within a phantom and/or patient within the MRI-linac (Raaijmakers *et al.*, 2005). It can also potentially affect the measuring of dose. Previously the performance of a Farmer-type chamber (Meijsing *et al.*, 2009; Smit *et al.*, 2013; Reynolds *et al.*, 2013; O'Brien *et al.*, 2016), 2D-arrays (Smit *et al.*, 2014), a water phantom (Smit *et al.*, 2014b), 3D-arrays (Houweling *et al.*, 2016; de Vries *et al.*, 2018) and an on-board EPID mounted outside the magnet (Raaymakers *et al.*, 2011) have been investigated and their feasibility confirmed.

Accurate small-field dosimetry is critical for the MRI-linac. The PTW 60019 microDiamond is close to an ideal detector for small field dosimetry due to its small physical size, high signal-to-noise ratio and approximate water equivalence (Lárraga-Gutiérrez *et al.*, 2015). Its primary use is within scanning water phantoms for determining percentage depth dose (PDD) curves, profiles and relative output factors, especially for small fields.

The performance of Diamond and microDiamond detectors have been previously established for conventional radiotherapy beams (De Angelis *et al.*, 2002; Laub *et al.*, 2014; Lárraga-Gutiérrez *et al.*, 2015), small-field radiotherapy (Ciancaglioni *et al.*, 2012; Ralston *et al.*, 2014; De Coste *et al.*, 2017) and high-dose-per-pulse flattening filter free (FFF) beams (Brualla-González *et al.*, 2016; Reggiori *et al.*, 2017). Diamond and photon diode detectors have also been studied in a 0.18 T magnetic field and simulated with higher magnetic field strength (Reynolds *et al.*, 2014).

The aims of this study were to test if a PTW microDiamond is suitable for use in an MRI-linac, and to characterise the detector performance and identify any limitations on use.

4.2 Materials and Methods

Unless otherwise noted, detectors were mounted within a prototype MR-compatible scanning water phantom (Smit *et al.*, 2014b) with source-surface distance (SSD) 133.5 cm, 10 cm less than the MRI-linac source axis distance (SAD) of 143.5 cm. The reference conditions for absolute dosimetry were 69.9 cGy per 100 MU at a depth of 10 cm with an SSD of 133.5 cm and a field size of 10x10 cm² at isocentre, approximately equivalent to 100 cGy per 100 MU at the d_{max} of 1.3 cm. Irradiations without a magnetic field were delivered with a 6 MV beam (Elekta Synergy S, Elekta AB, Stockholm, Sweden) and measured with a Blue phantom (IBA-Dosimetry, Schwarzenbruck, Germany). The reference

conditions were 100 cGy per 100 MU at the d_{max} of 1.6 cm, an SSD of 100.0 cm and a field size of 10x10 cm² at isocentre.

A comprehensive set of acceptance tests were performed, as outlined in table 4.1.

Test	Outcome	Value	Tolerance
visual inspection	passed		
x-ray inspection	recorded		
constancy	passed	σ 0.03 %	1.0% ¹
warm-up	passed	-0.06 ± 0.6 % per 100 MU	
leakage	passed	max -0.042 fA	20 fA ²
dose linearity (5 - 1000 MU)	passed	max 1.9%	2.0% ¹
dose rate linearity	passed	max 0.3%	2.0% ¹
field size (ROFs)	passed	max -0.3%	1.0% ¹
automated data collection mode	passed		
comparison with verified detector	passed	max 0.5%	1.0% ¹
effective point of measurement	determined	$+0.80 \pm 0.23$ mm	
angular dependence	determined	max 0.6% < 20 cm from CAX	
other manufacturer tests	passed		
recombination	-		
T and P dependence	-		
energy dependence	-		
absolute dose calibration	-		
polarity correction	-		
stem effect	-		

¹ Local department detector tolerances consistent with use for NCS 9 and AAPM 142.

² PTW microDiamond manual.

Table 4.1: Summary of acceptance tests as applied to the microDiamond detector.

4.2.1 Detectors

The PTW 60019 microDiamond (SN 122763) (PTW, Freiburg, Germany) acts as a diamond Schottky diode with a thickness of 1 μ m and a diameter of 2.2 mm (Almaviva *et al.*, 2008, 2010; Betzel *et al.*, 2010). The vendor-specified effective point of measurement (EPoM) for standard MV beams is 1.0 mm below the top surface of the housing (PTW, 2014) and it was operated at 0 V. A Unidos E electrometer (SN 092012) (PTW, Freiburg, Germany) was used to collect point measurements.

The detector was setup vertically (IEC 61217 +z direction) in the water phantom under standard conditions; vendor-specified effective point of measurement of detector at isocenter, depth 10 cm, SSD = 133.5 cm, 10x10 cm² field and gantry 0 degrees. The detector stem was perpendicular to the magnetic field and parallel to the G0 radiation beam. Other orientations (eg parallel to the bore and perpendicular to the G0 radiation beam) were not tested. Measuring in water prevented any air gaps, which have been shown to



Figure 4.1: Photo and x-ray of PTW 60019 microDiamond detector with scales shown.

affect dose deposition and dose measurement in a magnetic field (Hackett *et al.*, 2016; O'Brien *et al.*, 2017; Malkov *et al.*, 2017).

The microDiamond was compared to a cylindrical ion chamber CC04 (SN 11931) with collecting voltage -200 V and a parallel plate ion chamber Wellhofer Roos PPC-35 (SN 086) with collecting voltage -250 V (IBA-Dosimetry, Schwarzenbruck, Germany).

CC04 and CC08 (SN 7575) (collecting voltage -300 V) detectors were also used as monitor ion chambers (figure 4.2). The CC04 was used inside the top of the bore (above the phantom) inside a brass build up cap. The CC08 was mounted next to the waveguide and was connected to a PCElectrometer (SN 103746002) (Sun Nuclear Corporation, Melbourne, USA) (see figure 4.2).

4.2.2 Inspection and functionality

Visual and x-ray inspections (figure 4.1) and basic functionality tests were performed.

Tests of data acquisition with the PTW phantom were performed. 10 points each were acquired in point-measurement mode for different integration times, delay times and with/without monitor chamber. This is consistent with the PTW phantom step-and-integrate data collection mode, but without any detector movement.

4.2.3 Detector constancy, linearity and field-size

10 measurements of 100 MU from a 10×10 cm² field were made consecutively over approximately 10 minutes to assess short-term reproducibility. Measurements were repeated for 2 to 950 MU, and pulse repetition frequencies (PRF) of 34 to 275 Hz to test dose linearity and doserate linearity. Measurements were simultaneously recorded with

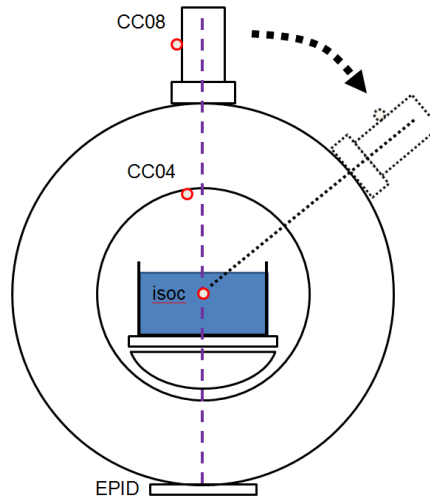


Figure 4.2: Schematic showing detector locations around the MRI-linac including monitor chambers next to the waveguide and attached to the inside top of the bore. Also shown in dotted lines is one of the linac positions used for angular dependency measurements, where the beam continues to point at radiation isocentre (isoc) from above the side of the water phantom.

the in-bore CC04 monitor chamber to compensate for any fluctuations in linac output. Dose per pulse was not varied.

Relative output factors for field sizes of 1×1 to 10×10 cm^2 were measured and compared to measurements with the CC04 detector in the phantom at isocentre. In both cases the detectors were positioned at a depth of 10 cm and offset $+0.35$ cm in the $+x$ crossline direction (IEC 61217) at the lateral position of maximum dose within the beam, due to the skew introduced by the magnetic field. For the 1×1 cm^2 field the offset was $+0.2$ cm.

4.2.4 Leakage and warmup

Leakage was assessed by making two readings at least 20 minutes apart, with no additional radiation delivered between readings. Leakage was assessed at 0 cGy and ~ 70 cGy.

Detector warmup was tested. Three irradiations of 950 MU were delivered at 780 MU/min, with delays of 51 minutes and 7 minutes between irradiations. Measurements with the microDiamond were logged in 1 s intervals using Dosicom software (PTW, Freiburg, Germany). Simultaneous measurements were logged with the CC08 ion chamber to correct for any dose rate variation in the linac.

4.2.5 Angular dependence

In the absence of an ideal spherical phantom, dependence on polar angle of irradiation was tested by rotating the gantry between -60 to +60 degrees in 10 degree intervals. It was not possible to rotate further due to the walls of the phantom (see figure 4.2). The position of the detector at isocentre was confirmed to within ± 1 mm using MV imaging. The measurements were repeated using the cylindrical CC04 ion chamber. Cylindrical chambers have angular dependence tolerance of $< 0.5\%$. The performance of the microDiamond was assessed relative to the CC04 readings. Thus cryostat transmission and change in path length through water were eliminated as potential factors.

The test was also performed without magnetic field using an Elekta Synergy linac and IBA Blue water phantom and compared to previously published values (PTW, 2014) in order to demonstrate that the phantom setup and technique were valid, and to eliminate beam energy spectrum variation with depth, or any other environmental causes as factors.

4.2.6 Effective point of measurement

Percentage depth dose (PDD) curves for a 10×10 cm² field were measured along beam central axis.

A well-guarded parallel plate chamber is the preferred detector for measurement of PDDs, especially in the build up region (Andreo *et al.*, 2000; van Dyk, 1999). The Roos PDD curve was measured with opposite polarising voltages (-250 V and +250 V) to assess any polarity effect in the build up region. PDDs were measured five times for the Roos chamber and four times for the microDiamond with fresh re-positioning of the phantom and detector for each scan. The curves were then matched to each other within the build-up region (1-12 mm) to determine an average depth offset between the Roos and the microDiamond EPoM, and to determine the uncertainty in the measurement. Uncertainty was also quantitatively determined by measuring the reproducibility of surface position setup for 10 independent setups of each detector.

4.2.7 Measurement comparison with other trusted detectors

Along with the effective point of measurement comparison to the Roos chamber, consecutive measurements were made with the microDiamond and a CC04 ion chamber. Measurements were made of a 10×10 cm² field PDD, with inline and crossline profiles at 1.3 cm and 10 cm depth, and of a 2×2 cm² field PDD, with inline and crossline profiles at 10 cm depth. Comparisons were also made with previous CC04 scans (PDD with inline and crossline profiles at 1.3 cm and 10 cm depth) made on the same linac with a 20×20 cm² field.

4.2.8 Additional information

The following tests were not expected to be influenced by the MRI-linac magnetic field, and were therefore expected to demonstrate the same behavior as previously observed on standard linacs.

Dependence on temperature and pressure was not tested. The microDiamond is independent of pressure. Insignificant temperature variation (0.3% in 20 °C) has been previously reported (Ciancaglioni *et al.*, 2012).

Neither photon beam quality nor initial electron energy spectra change with magnetic field. Dependence on beam quality of a PTW 60003 Diamond has previously been tested with no energy dependence reported (De Angelis *et al.*, 2002).

Dose per pulse dependence was not directly tested. Traditionally a factor of x8 variation in dose-per-pulse can be easily achieved by changing the source-detector distance (SDD). Due to the extended SDD of the MRI-linac and the closed bore, it is only possible (with difficulty) to achieve a factor of \approx x2.3 variation in dose-per-pulse, and therefore this test was not performed.

Recombination and polarity effects were not directly tested. The microDiamond operates at 0 V thus polarity is not relevant.

However, it is noted that PDDs and profiles depend on beam energy spectrum and, to a lesser extent, recombination and dose-per-pulse, and thus the comparison of microDiamond PDDs and profiles to those of the CC04 detector provides a practical check on energy dependence and recombination.

4.3 Results and discussion

4.3.1 Functionality

The microDiamond worked satisfactorily with the water phantom and tandem electrometer, UnidosE electrometer and with the Dosicom software.

Tests of microDiamond data acquisition under scanning conditions demonstrated that variation in measurements did decrease with increasing measurement time. All 1-s measurement sets had standard deviations less than 0.25%. 0.5-s measurements with a monitor chamber (the standard approach for profile scanning) also had standard deviations less than 0.26%. Shorter measurement times had higher uncertainties, up to $\sigma = 0.41\%$.

4.3.2 Detector constancy, linearity and field-size dependence

Short term constancy was measured. The standard deviation of the ratio of readings (microDiamond / CC04) was 0.03%, well within the tolerance of 1.0% (Kutcher *et al.*, 1994).

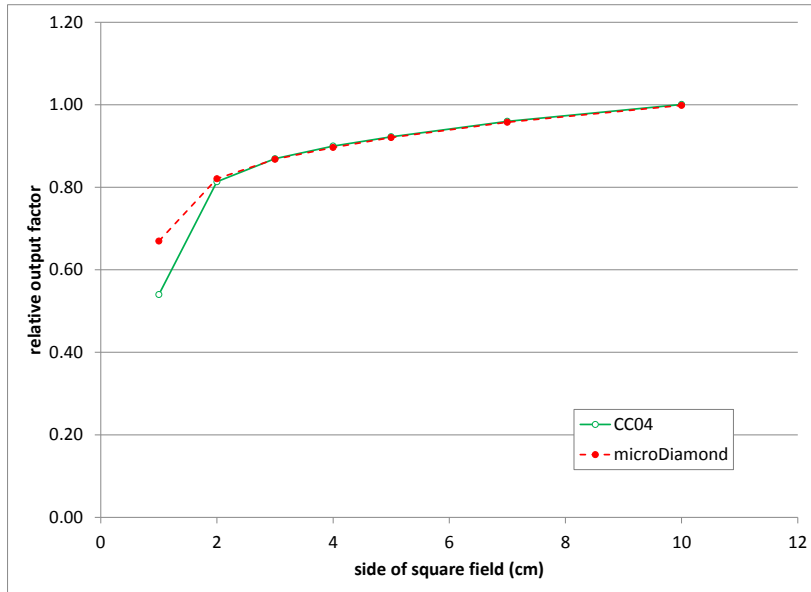


Figure 4.3: Relative output factors for the MRI-linac measured with a microDiamond and a CC04 ion chamber. Statistical uncertainties are smaller than point symbols.

MicroDiamond linearity with dose and with dose rate (pulse repetition frequency) was measured with fixed detector and beam conditions. Relative to the readings at 100 MU, the average scaled readings at 2 MU and 5 MU were +3.4% and +1.9% respectively, which is within standard specifications for linac testing. All other values were within 1.0%. Deviation with dose rate was less than 0.3% for all values. The microDiamond is linear with dose and dose rate (PRF) to within specifications for all intended purposes.

Relative output factors for field sizes of 1×1 to 10×10 cm² were measured. The standard deviation of the reference readings for 10×10 cm² field that were repeated throughout the experiment were 0.35% for the CC04 and 0.22% for the microDiamond, which are smaller than the point symbols in the graph. The microDiamond and the CC04 gave very consistent results down to 2×2 cm². The microDiamond measured a higher value for the smallest field sizes, consistent with the greater volume averaging in the CC04 chamber (figure 4.3). For the results presented here, no corrections were applied for volume averaging or for fluence perturbation. This implies that, following the conclusion of Ralston *et al.* (2014), the microDiamond ROF for the 1×1 cm² field is probably over-estimated by $2 \pm 1\%$.

4.3.3 Leakage and warmup

MicroDiamond leakages of -0.042 fA (at 0 cGy) and -0.007 fA (at 70 cGy) were measured. These rates are well within the tolerance of 20 fA (PTW, 2014).

All detector warmup results were consistent. Data from the middle run is shown in figure 4.4. The linac dose rate dropped by $\approx 2\%$, however this was accounted for with the CC08 monitor chamber. Due to the short 1-s integrations, the combined read-out noise of the two detectors was $\approx 1.7\%$. The microDiamond did not show any significant change in sensitivity during the first 100 MU, consistent with the results of Laub *et al.* (2014).

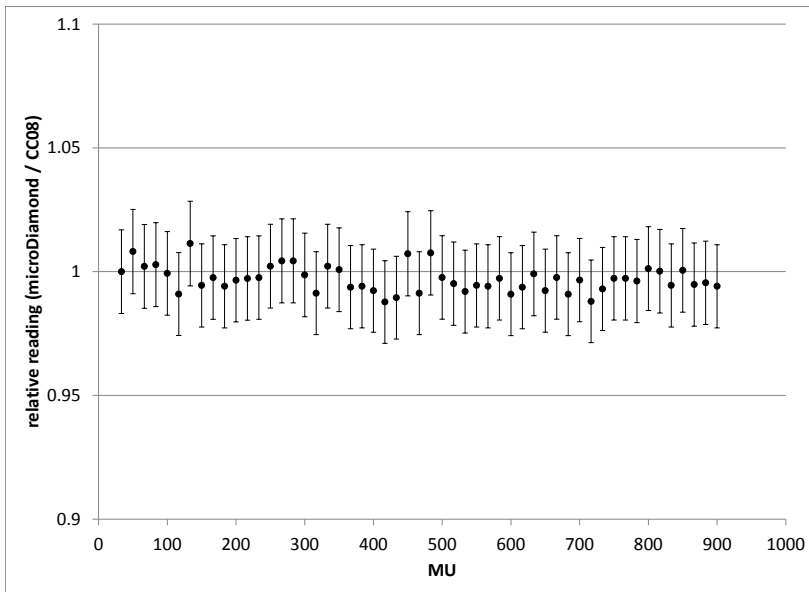


Figure 4.4: Initial response of the microDiamond during a single, long beam, with reading normalised to a monitor ion chamber (CC08). Even with 1-s observations there is no initial or warmup effect with time or radiation exposure.

4.3.4 Angular dependence

The angular dependence of the microDiamond is shown in figure 4.5. Measurements without magnetic field were symmetrical, changed by less than 2%, and were consistent with PTW data (PTW, 2014). Measurements with magnetic field demonstrated a strongly asymmetric response due to the Lorentz force on the secondary electrons released in the water. The intended use of the microDiamond is for small-field measurements in

a water phantom with beams incident from gantry 0 degrees. Anywhere within 20 cm of beam central axis the average angle of incident photons will be within ± 4 degrees. Therefore the maximum effect, even with magnetic field, is $\approx 0.6\%$. However for large beams with a magnetic field, the microDiamond would not be ideal for characterising the profiles and it would not be suitable for determining large-field beam parameters such as symmetry. It would also require a correction factor prior to use for patient-specific QA measurements where radiation is delivered from different gantry angles.

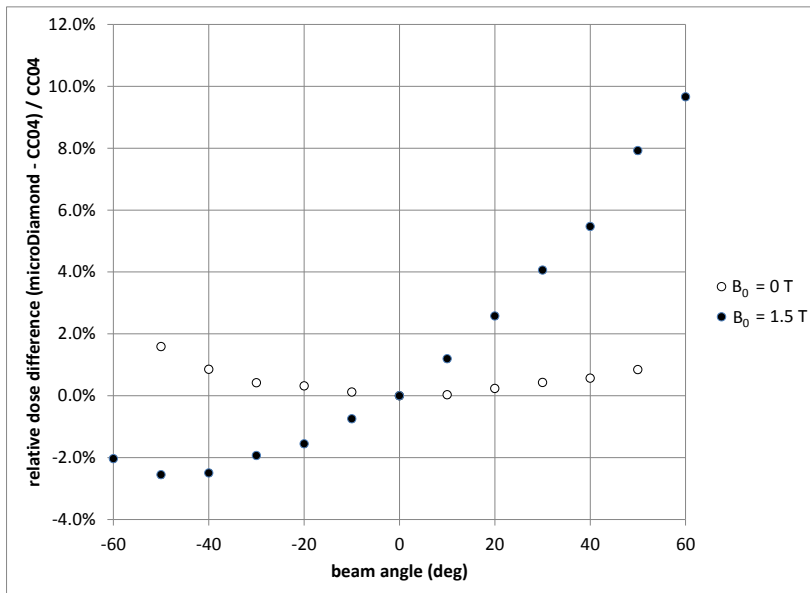


Figure 4.5: Angular sensitivity of the microDiamond relative to a CC04 ion chamber for incident beams at different gantry angles. Black circles show the average of the individual measurements (blue diamonds, mostly obscured). Asymmetric differences are probably due to the Lorentz force on the secondary electrons.

4.3.5 Effective point of measurement

The effective point of measurement of the Roos chamber is at the centre of the inside surface of the upper electrode. The entrance window of the Roos chamber has a physical thickness of 1.1 mm (PTW, 2015) and the effective point of measurement of the Roos chamber is 0.15 ± 0.01 g cm⁻² below its outer surface (Loe *et al.*, 2011). It is not expected that the effective point of measurement of the Roos chamber will be affected by the magnetic field as the chamber is well-guarded laterally and the source of electrons within the Roos chamber is still the inner surface of the upper electrode. This was not

experimentally verified, however it is consistent with the use of this type of chamber in the literature (Ghila *et al.*, 2016).

For the Roos chamber PDDs measured with -250 V and +250 V, differences at all positions were less than 0.02 mm or 0.2%. Thus, no polarity effect was observed and no correction was applied.

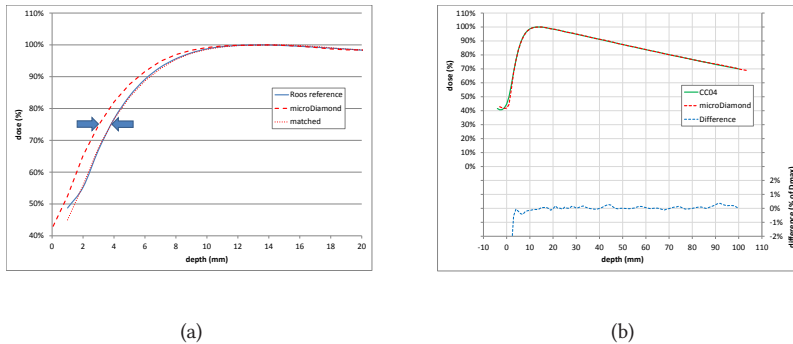


Figure 4.6: Percentage depth dose curve comparisons for a 10x10 cm² beam. (a) Effective point of measurement of the microDiamond was determined relative to the Roos chamber. (b) Agreement between the microDiamond measurement (red) and the CC04 measurement (green) was excellent, with differences shown in blue. Maximum difference beyond d_{max} was 0.3%.

From comparison of the measured PDDs, the average difference in the position of the top of the microDiamond and the top of the Roos chamber was 0.70 mm.

The 4 microDiamond scans had positional deviations of $\sigma = 0.10$ mm and the 5 Roos scans had positional deviations of $\sigma = 0.19$ mm. Assuming independence, adding the Roos and microDiamond scan variances implies an uncertainty in the average offset of $\sigma = 0.10$ mm. The 95% confidence interval on the random error was then ± 0.23 mm (t-distribution). The set-up of the Roos chamber at the water surface was repeated 10 times with standard deviation 0.13 mm. The microDiamond set-up was repeated 10 times with $\sigma = 0.09$ mm. Both distributions were consistent with the range of positions determined from the PDDs.

Thus the effective point of measurement of the microDiamond was determined experimentally to be $+0.80 \pm 0.23$ mm below its top surface.

Within a standard MV photon beam the microDiamond has a nominal EPoM of 1.0 mm which is marked as a black line on the outside of the detector (PTW, 2014). To within the limits of experimental uncertainty, this mark remains valid for use with the microDiamond in an MRI-linac.

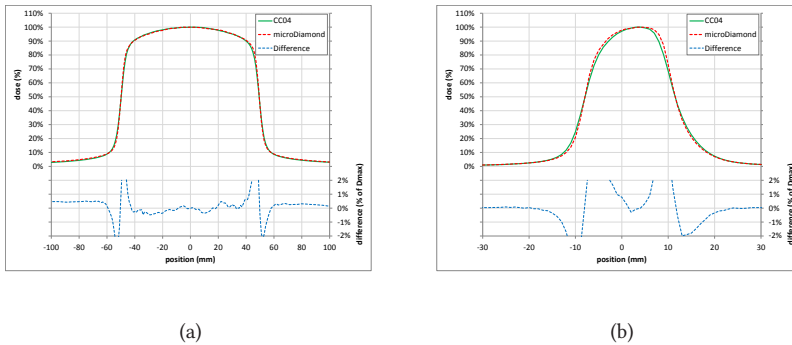


Figure 4.7: (a) Inline profile of a 10x10 cm² beam and (b) crossline profile of a 2x2 cm² beam, both at depth 10 cm. The microDiamond measurements (red) are in excellent agreement with the CC04 measurements (green). Differences are shown in blue. Maximum difference within the 10x10 cm² beam is 0.5%. The microDiamond measurement exhibits a sharper penumbra than the CC04 measurement as expected. There are no out-of-field low-dose or background-subtraction issues.

4.3.6 Measurement comparison with other trusted detectors

All 2x2, 10x10 and 20x20 cm² field scans with the microDiamond were in good agreement with those of the CC04. The maximum difference in the 10x10 cm² beam PDD was 0.3% (figure 4.6) indicating the suitability of the microDiamond for measuring PDDs. The inline profile at depth 10 cm is shown in figure 4.7a. The maximum difference within the beam is 0.5% and the tails of the microDiamond profile are in excellent agreement with the ion chamber. In the 2x2 cm² beam the microDiamond penumbra is steeper than that of the CC04 ion chamber (figure 4.7b). This is expected as the microDiamond has a collecting area of diameter 2.2 mm with less volume averaging than the CC04 with its internal diameter of 4 mm. Dose differences of greater than 2% due to the steep dose gradient in the penumbra are not shown in figures 4.7a and 4.7b. Reynolds *et al.* (2014) propose that Diamond and photon diode detectors may exhibit significant relative dosimetry variations during beam scanning, however no such variations were observed in this study with a microDiamond.

4.3.7 Beam quality and magnetic field strength

The microDiamond MRI-linac tests reported here were conducted only for a photon nominal beam energy of 7 MV and 1.5 T magnetic field. However, based on the results here, and on the basic physical principles, it is expected that the microDiamond is also valid for use in similar environments, such as the ViewRay 0.35 T system with 6 MV or Co-60 radiation (Mutic *et al.*, 2014). Additional checks may be required for the angular sensitivity of the microDiamond in each specific environment.

4.4 Conclusion

The PTW 60019 microDiamond has passed all required tests and is suitable for use in a 1.5 T magnetic field within a MRI-linac. Due to its significant angular sensitivity it is not suitable for characterising large radiation fields, and would require additional careful testing prior to use with beams incident on the detector from different angles. It is recommended that microDiamond scans be performed with 0.5-s measurement time, 0-s delay time and with a monitor chamber to compensate for any fluctuations in linac output. For small-field scans where a monitor chamber is impractical, it is recommended to increase the measurement time to 1-s per point and to check for variations in linac dose rate during the measurement beam.

4.5 Acknowledgments

Our thanks to PTW for the loan of the PTW 60019 microDiamond detector.

CHAPTER 5

Acceptance procedure for the linear accelerator of the 1.5 T MRI-linac

The following chapter is based on:

Woodings S.J., de Vries J.H.W., Kok J.G.M., Hackett S.L., van Asselen B., Bluemink J.J., van Zijp H.M., van Soest T.L., Roberts D.A., Lagendijk J.J.W., Raaymakers B.W. and Wolthaus J.W.H. Submitted, 19 Sep 2019 Acceptance procedure for the linear accelerator of the 1.5 T MRI-linac *Journal of Applied Clinical Medical Physics*

Abstract

Purpose: To develop and implement an acceptance procedure for the new Elekta Unity 1.5 T MRI-linac.

Methods: Tests were adopted and, where necessary adapted, from AAPM TG106 and TG142, IEC 60976 and NCS 9 and NCS 22 guidelines. Adaptations were necessary because of the atypical maximum field size ($57.4 \times 22 \text{ cm}^2$), FFF beam, the non-rotating collimator, the absence of a light field, the presence of the 1.5 T magnetic field, restricted access to equipment within the bore, table motion only in the longitudinal direction, and MR image to MV treatment alignment. The performance specifications were set for stereotactic body radiotherapy (SBRT).

Results: The new procedure is performed similarly to that of a conventional kilovoltage x-ray (kV) image guided radiation therapy (IGRT) linac. As proof of feasibility, results for the first Unity system are presented.

Conclusions: A comprehensive set of tests was developed, described and implemented for the MRI-linac. The MRI-linac meets safety requirements for patients and operators. The system delivers radiation for SBRT effectively. Specifications for clinical introduction were met.

5.1 Introduction

Elekta AB (Stockholm, Sweden), Philips (Best, The Netherlands) and University Medical Center Utrecht have developed a linear accelerator (linac) with integrated 1.5 T magnetic resonance imaging (MRI) (figure 5.1). This combination facilitates simultaneous irradiation and high-precision image guidance with soft-tissue contrast (Lagendijk *et al.*, 2014). Elekta Unity (MRI-linac) is the clinical implementation of the prototype machine described by Raaymakers *et al.* (2009). The system is in clinical use (Raaymakers *et al.*, 2017; Werensteijn-Honingh *et al.*, 2019).

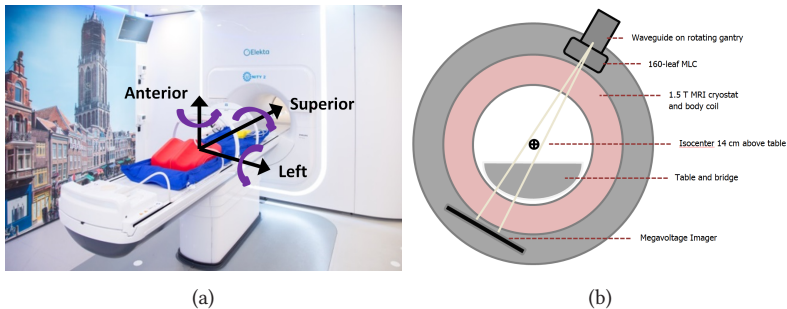


Figure 5.1: (a) Image of the first clinical Elekta Unity MRI-Linac at UMC Utrecht, including head-first supine patient coordinates, and (b) schematic showing basic linac and system features.

In order to safely and effectively deliver radiation beams from this machine to a patient, it is necessary to perform an acceptance testing and commissioning process. The fundamentals of this process are well established in the Medical Physics and Radiotherapy communities and are documented by, for example, the IEC (International Electrotechnical Commission, 2007), AAPM (Klein *et al.*, 2009; Das *et al.*, 2008), IPEM (Mayles *et al.*, 1999; Kirby *et al.*, 2006) and NCS (Meijer *et al.*, 1996; van der Wal *et al.*, 2013). However, due to the nature of this machine and the presence of the strong magnetic field, new methods and equipment had to be developed for some of the tests, and some entirely new tests had to be created. The aims of this study are to:

1. Create an acceptance testing procedure with reference to existing protocols;
2. Describe modified and new tests and equipment;
3. Demonstrate feasibility of the procedure by providing results of the tests from the first Unity MRI-linac.

5.1.1 MRI-linac special characteristics

The Elekta Unity has a 1.5 T magnetic field which points out of the bore (figure 5.1). The presence of the magnetic field means that all equipment, including for example water phantom drive motors, must be MR-compatible.

Dose measurements and dose distributions are affected by the B field. The Lorentz force acts on charged particles, pulling them in a direction orthogonal to both their vector motion and the magnetic field. This has a small effect inside and outside the radiation beam, but is clearly noticeable where there is an absence of electronic equilibrium – at interfaces and beam edges (Raaijmakers *et al.*, 2005). This effect must be taken into account in assessment of beam symmetry, beam edges, beam alignment and alignment of beam limiting devices. Furthermore, the electron return effect (ERE) must be characterized (Woodings *et al.*, 2018a). Finally, charged particles can also stream along magnetic field lines, which must be considered during radiation safety tests (eg dose to patient) (Malkov *et al.*, 2019) and during clinical implementation.

The 70 cm diameter wide-bore system is large enough for most patients but is a limit on equipment size. The isocenter is not easily accessible from outside the bore and therefore most equipment is setup externally, and then transferred with precise table motion to isocenter, similarly to other radiotherapy systems with bores (eg Halcyon, Tomotherapy and MRIdian). There is no light field, therefore the gantry-mounted megavoltage imager (MVI) is used for equipment position verification and for the daily morning QA check (figure 5.1).

The radiation beam passes through the liquid helium-filled, multi-layered metal cryostat and the MRI body coil. These have been designed to be as homogeneous as possible but the transmission varies with gantry angle and must be characterized for the TPS. The cryostat and coil are a source of scattered radiation. This requires additional characterization measurements and affects the beam model and radiation safety (Woodings *et al.*, 2018a). The level of liquid helium is stable, but can change after interventions such as magnet ramp-up or ramp-down. In order to minimize the effect of any change in the liquid helium level on clinical dose delivery, Elekta recommend that the beam is calibrated with a beam from gantry 90 degrees.

The Philips Marlin MRI (version 2017-04-10) has been designed with a cylindrical beam portal in the windings of the magnet so that the radiation beam can pass in between. This gap allows a maximum field size in the superior-inferior (y) direction of 22 cm at the isocentric depth, which is a limitation on clinical use at this moment. Due to the extended SAD a field size of up to 57.4 cm can be achieved in the lateral direction. This is important to optimally treat peripheral targets. Wider water phantoms have also been designed especially to accommodate QA tests for this field size.

The system delivers single-energy 7 MV flattening filter free (FFF) step-and-shoot intensity modulated radiation therapy (IMRT) beams from a standing wave waveguide mounted on a solid ring gantry around the MRI with a source axis distance (SAD) of 143.5 cm (figure 5.1). The system does not use steering coils and therefore there is much less chance of the beam steering being incorrect, or changing over time, which reduces the number of QA tests on linac stability. The internal monitor unit ion chambers are sealed.

The table is fixed with comfort mattress 13.0 cm below, and solid surface 14.0 cm below, isocenter. The table supports only longitudinal motion for initial patient setup and phantom setup. A treatment plan must be optimized based on images acquired of the patient in their current treatment position. Table accuracy, axis, angle and flex are not critical for clinical use, but they are important for setup of any phantoms which cannot be MR imaged. As the table is fixed, the radiation isocenter will typically not be within the target region and the MRI-linac will routinely deliver small off-axis radiation fields. Thus greater attention to these is required during beam characterization (Woodings *et al.*, 2018a). The linac gantry cannot tilt and the table cannot rotate so all MRI-linac treatments are co-planar. All beams have central axis perpendicular to the magnetic field.

The MLC is based on the Elekta Agility model with 80 leaf pairs with rounded leaf ends, each with projected width of approximately 0.72 cm at isocenter. The collimator does not rotate and therefore cannot be used to define a mechanical or radiation isocenter and therefore a new method is needed. MLC leaves move always in the superior-inferior (y) directions. The MRI-linac MLC has the additional capability to park opposing leaves underneath the primary collimator. The MLC is fully inter-digitating and can thus create island fields for simultaneous irradiation of multiple target regions. Minimum opposing leaf separation is set to 0.5 cm in the initial configuration. Full-attenuation diaphragms move in the orthogonal (x) direction.

Coordinate system transformation (alignment) between the MR imaging and MV delivery systems is critical and therefore must be tested.

Radiation delivery and MR imaging can be performed simultaneously without reducing image quality, and without affecting the radiation beam (Raaymakers *et al.*, 2009; Tijssen *et al.*, 2019). The magnet is linked across the plane of linac gantry rotation with a superconducting wire in a conduit. The conduit also allows the helium pressure to equalize across the whole system. The wire and conduit are centered within the beam at a gantry angle of 13° . Direct irradiation of this wire is excluded by the system. Thus there are limitations on beams delivered from approximately 13° , that depend upon field size and gantry angle and are incorporated into the treatment planning system (TPS).

5.2 Materials and Methods

5.2.1 Phantoms and detectors

There are special considerations for phantoms and detectors within a high-magnetic field environment. Phantoms must contain minimal ferromagnetic materials, which precludes their standard electric motors, power supplies, batteries, electronics and drive arms (Smit *et al.*, 2014). Air cavities must be eliminated to avoid perturbations to detector readings (Hackett *et al.*, 2016; Malkov *et al.*, 2017; O'Brien *et al.*, 2017).

Several phantoms were used for acceptance tests. Ion chamber scanning in water was

performed with an Elekta-Philips prototype MR-compatible MP3-style scanning water phantom, whose design was based on an earlier prototype (Smit *et al.*, 2014). Reference dosimetry was established with a PTW prototype MR-compatible MP1 (1D) water phantom (PTW, Freiburg, Germany) with a manual depth drive. Routine dosimetry was performed with a RW3 phantom consisting of multiple $30 \times 30 \times 1 \text{ cm}^3$ slabs and a prototype RW3 slab with a Farmer chamber cavity that can be sealed with water around the chamber to prevent any air layer affecting the detector reading (Hackett *et al.*, 2016). Other RW3 slabs, with chamber cavities that can be filled with ultrasonic gel, were used for various point dose measurements. A polymethylmethacrylate (PMMA) buildup cap with diameter 3.2 cm (with water-filled cavity), was used with a Farmer chamber for comparison of radiation beams from different gantry angles.

Elekta provided several phantoms for specific tasks. The Elekta MV Geometry Phantom was used to measure the isocenter coordinates on the MV imager (MVI). The Elekta MR-MV phantom, consisting of multiple ceramic ball bearings mounted in a CuSO_4 -filled framework, was used to measure the coordinate transformation between the MRI and the MV coordinate systems. The Elekta Las Vegas phantom and the Standard Imaging (Middleton, USA) QC3 phantom were used to measure MVI image quality. The Elekta Pixel Tool, a precision-milled 2D brass plate, was used to measure the MVI pixel size and panel tilt.

The readings in air-filled ion chambers are dependent on the relative orientations of radiation beam, magnetic field and chamber axis, and on chamber size, beam energy and field strength. These differences are due to the varying average path length of the ionising track of a secondary charged particle and the inflow of electrons into the chamber (Meijsing *et al.*, 2009). Additional correction factors are required for absolute dosimetry (O'Brien *et al.*, 2016; Reynolds *et al.*, 2013; Smit *et al.*, 2013; Spindeldreier *et al.*, 2017; van Asselen *et al.*, 2018). Relative dosimetry measurements in a scanning water phantom within the expected range of conditions can still be made with $< 0.3\%$ error due to chamber orientation (Smit *et al.*, 2014).

PTW30013 and FC65-G (IBA-Dosimetry, Schwarzenbruck, Germany) Farmer-type waterproof chambers were used with collecting voltage -250 V for absolute dosimetry. Waterproof chambers were chosen to enable measurements in water (or with water-filled phantom cavities) to prevent dosimetric artifacts from air layers around the detectors (Hackett *et al.*, 2016). Semiflex3D detectors were used for medium and large-field relative dosimetry. The measurement point of the Semiflex3D within a 1.5 T magnetic field was assigned so that it was equivalent to the microDiamond. The resultant effective point of measurement (EPoM) was very close to the -0.5 mm value used by UMCU and the $-0.3 r_{\text{cyl}} = -0.7 \text{ mm}$ recommended by O'Brien *et al.* (2018). A PTW60019 microDiamond detector was used with an EPoM of +1.0 mm for small-field measurements and for assessing beam penumbra (Woodings *et al.*, 2018b). A PTW Tandem electrometer was used with the Elekta-Philips phantom for collecting profile data. PTW Unidos E and Unidos Webline electrometers were used for point data collection.

A PTW31010 Semiflex detector was used as a monitor (reference) ion chamber. The chamber was mounted on an arm above the water surface and inside the corner of a 5 x 5 cm² field. It was later observed that for best results with the scanning water phantom the reference chamber should be placed well above the water surface (private communication, PTW).

2D array measurements were made with a PTW StarCheck maxi MR and a Sun Nuclear IC Profiler MR (Melbourne, USA).

The megavoltage imager (MVI) plays an important role in the alignment of the various measurement equipment. The Perkin Elmer (Santa Clara, USA) amorphous silicon detector is rigidly mounted on the gantry ring, aligned opposite to the beam at a source-detector distance (SDD) of 2658 mm. It has 1024 x 1024 pixels over an area of 410 x 410 mm². The physical pixel size and positions are rescaled to the isocenter distance. The MVI is located at a position on the gantry ring outside the MR cryostat where the magnetic field is close to 0 (Torres-Xirau *et al.*, 2018) (see figure 5.1). Thus the MVI data is free of magnetic field induced artifacts and remains an effective surrogate of the photon fluence.

Film sandwiched between copper sheets (thus capturing all generated electrons) was also used to measure a surrogate of photon fluence that was independent of Lorentz force (van Zijp *et al.*, 2016). Absolute position on a coronal film was acquired, if necessary, by simultaneous imaging with the MVI and then registering the film image to the MVI image and position.

5.2.2 Coordinate systems

The radiation delivery system (linac) uses the IEC61217 coordinate system (International Electrotechnical Commission, 2011) with the origin at isocenter. The imaging system uses DICOM coordinates. The megavoltage imager (MVI) rotates with the gantry, and therefore its coordinate system also rotates with respect to the patient. Its origin is in one corner of the panel (gantry 0 degrees, head first supine patient superior, right direction). The watertank has a coordinate system which can be modified in its software settings. Here it was set for consistency with IEC 61217. The coordinate systems are compared in table 5.1.

HFS Patient	IEC 61217 fixed	DICOM	MVI G 0°	MVI G 90°
Left	$+x$	$+x_{\text{DICOM}}$	$+u$	
Superior	$+y$	$+z_{\text{DICOM}}$	$-v$	$-v$
Anterior	$+z$	$-y_{\text{DICOM}}$		$-u$

Table 5.1: Coordinate systems used in the Elekta Unity system and in this article, compared to a head first supine (HFS) patient (see figure 5.1).

5.2.3 Acceptance tests

The acceptance tests are presented in categories. The acceptance tests are listed in table 5.2. A logical and efficient order in which tests should be done, based on dependencies and efficiency, is shown in Figure 5.2.

Table 5.2: Linear accelerator acceptance tests and specifications. External references for tests and specifications are shown in brackets.

Section	Description	Phantom	Specification
A1	Safety Inhibit systems		
A2	Radiation shielding Scattered radiation to the patient Bunker protection	Mini-phantom	ave <0.1% of in-field dose (IEC 60601-2-1) < 1.0 mSv/year
	Coordinate systems and data integrity Radiation beam and beam shaping (IEC61217) MVI (IEC61217) MRI (DICOM)		
A3	MVI Panel rigidity Rotational alignment Pixel scale and isocenter Image quality	Ball bearing Water phantom Elekta pixel tool, MV alignment phantom QC3, Las Vegas	< 0.3 mm < 0.2°
A4	Mechanical and dosimetric alignment of gantry, focal spot and beam Gantry tilt Gantry rotation and readout Beam alignment Isocenter locus	Spirit level Spirit level and spoke film Film, water phantom Film	< 0.2° < 0.2° < 1 mm and < 0.2° < 0.5 mm radius
A5	Mechanical and dosimetric alignment of MLC and jaws MLC stripe test MLC transmission Jaw stripe test Gantry angle dependency	Film, MVI Film, water phantom Film, MVI Film, MVI	< 0.5 mm (TG 142) < 0.5% from base-line/TPS (TG142) < 1 mm (TG 142) < 0.5 mm (TG 142)
A6	Table		

Table 5.2: Continued.

Section	Description	Phantom	Specification
	Orthogonality and movement	MVI	< 1° and < 2 mm (TG 142)
A7	Laser – Elekta indicative sagittal laser MR to MV alignment	Ball bearing	< 1 mm (TG 142)
A8		Elekta MR-MV alignment phantom	< 0.3° (Elekta)
A9	Dosimetric system		
	Output stability – short and long term	RW3	< 2% (TG 142)
	2nd linac monitor chamber	RW3	< 2% (TG 142)
	Linearity	RW3	< 2% (TG 142)
	Dose rate dependency	RW3	< 2% (TG 142)
	Output gantry angle and cryostat dependency	Mini-phantom	< 1% from baseline (TG 142)
	Profile constancy StarCheckMaxi		< 1% (TG 142)
	Profile gantry angle dependency	ICprofiler	< 1% (TG 142)
	Internal monitoring and beam cutoff	ICprofiler	3%
	Reference dosimetry	Water phantom	< 1% (NCS 18)
A10	Beam performance during MR imaging	Water phantom	< 2%

5.2.4 A1: Safety

Standard safety inhibit and interlock tests included ferrogaurd, ring-out system, door interrupt, radiation warning lights and audio, camera functionality, function keypad interrupt and terminate buttons and lights, machine room door inhibit on gantry motion, table drive and emergency on button. Functionality and calibration were checked for lasers, heating ventilation and air conditioning (HVAC) system condensation, SF6 gas level and bottle weight, mains power supply lights, cellar door interlock, magnet-on light and flood alarm. Functionality of the 2nd dose channel, dose difference and uniformity interrupts were checked during the Elekta Device Acceptance Tests (DAT). Changing the gun grid voltage can change the beam doserate, output, quality and profile. With assistance from Elekta, the change in dose distribution for a beam just within the linac internal interrupt tolerances was quantified. The maximum differences in output and beam quality were measured with an ion chamber in RW3. Maximum differences in profile (off axis dose) were measured with an IC profiler.

5.2.5 A2: Radiation shielding

A limit of 1.0 mSv/y was applied outside the treatment bunker, consistent with national guidelines in the Netherlands and IAEA SRS 47 (International Atomic Energy Agency, 2006). Primary and secondary shielding walls, and the maze and door were assessed using standard methods. Neutron dose measurements were performed. Doses within the

plane of the patient, and doses around the head of the linac were measured (International Electrotechnical Commission, 2009).

5.2.6 A3: MVI tests – alignment and isocenter

The Megavoltage Imager (MVI), formerly electronic portal image device (EPID), is not intended for patient imaging. It is the fundamental device used for QA and verifying equipment position inside the bore of the MRI-linac. It also plays a significant role in the independent system alignment checks shown in figure 5.2. As it is such a fundamental device for QA, the MVI panel rigidity was tested with a 5x5 cm² MLC-only beam delivered from 12 gantry angles (each 30 degrees apart). A ball bearing was placed within foam blocks close to isocenter. The ball bearing location and the beam edges were measured in each image. The ball bearing projected u position varied sinusoidally with gantry angle due to its offset from the isocenter. This effect was fitted and corrected. Theoretically any residual variation in the imaged ball bearing location (u,v) would be due to either (a) MVI panel shift (b) focal spot shift or (c) gantry ellipticity. The uncertainty of the measurements was ~ 0.5 pixels = 0.1 mm. Any variation in the field edge positions would be due to the same effects and/or MLC shift.

MVI panel rotational alignment with the IEC 61217 coordinate system (see figure 5.3) was tested with the MP1 water phantom with the water surface nominally at isocenter. The water surface was imaged from gantry 90° and 270°. The angle of the MV image pixel columns relative to the water surface (α_{90} and α_{270}) were measured. Gantry tilt (θ_{gantry}) and MVI panel rotation (ϕ_{MVI}) were calculated from the angles using equations 5.1 and 5.2.

$$\phi_{\text{MVI}} = (\alpha_{90} + \alpha_{270})/2 \quad (5.1)$$

$$\theta_{\text{gantry}} = (\alpha_{90} - \alpha_{270})/2 \quad (5.2)$$

MVI image pixel scale was measured in both (u and v) directions using the Elekta Pixel Tool placed at isocenter. Any difference between the two directions would indicate panel tilt (figure 5.3). MVI images were acquired from both gantry 0° and 180° and the results averaged, which cancelled any small variation due to setup. Isocenter coordinates (u_{isoc} , v_{isoc}) projected on the MVI panel were determined using the Elekta device acceptance test (DAT) method. Conceptually the isocenter is uniquely defined as the central point in the vertical $x - z$ plane defined by gantry rotation of the focal spot. In practice this position can be accurately determined in the x and z directions (u_{isoc}) by imaging the Elekta geometry phantom ball bearing from multiple (12) directions. In the y direction, it is defined by Elekta as the projected position of the center of the beam limiting devices. Special Elekta service beams are provided where a V-shape in the back of each jaw is imaged with several jaw positions. These images are then processed with Elekta software to determine the v_{isoc} coordinate. An approximate check of the v position was



Figure 5.2: Schematic of independent system alignment checks for the linac component of the MRI-linac.

performed by imaging a ball bearing at multiple positions within the scanning water phantom.

MVI image quality was measured with the Las Vegas phantom and with the QC3 phantom, each at isocenter. The Las Vegas phantom was assessed visually and as per the Elekta DAT. The QC3 phantom was analyzed to determine the modulation transfer function (MTF) expressed equivalent to line pairs per mm, as per a previous published result from the MRI-linac prototype (Raaymakers *et al.*, 2011). The predefined phantom analysis tools in Theraview (Cablon Medical, Best, the Netherlands) were used.

5.2.7 A4: Mechanical and dosimetric alignment of gantry, focal spot and beam

Gantry tilt (rotation around the $+x$ axis) was determined with a spirit level, and from the MVI panel rotation measurement (see subsection A3 and figure 5.3). The frame of the gantry is not a reference surface, however spirit level measurements were performed

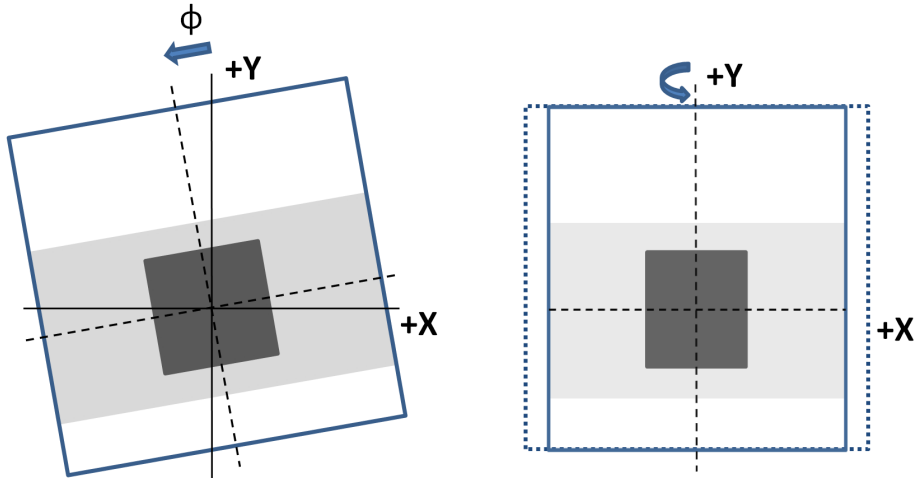


Figure 5.3: Schematic of MVI panel (a) rotation ϕ around z axis and (b) tilt around y axis.

for a number of different gantry rotations. Gantry rotation and readout (around the $+y$ axis) were measured with a spirit level on the reference surface of the Elekta beam generation system (waveguide). Measurements were made at 270 and 240 degrees, where the reference surface is accessible from the machine room.

An MLC-only spoke film was irradiated with beams from 12 different gantry angles delivered to an EBT3 film mounted in a transverse plane through isocenter (van Zijp *et al.*, 2016). The relative angles of the beams were then analysed, as well as the radius of the locus of isocenter.

Constancy of alignment of the focal spot and the MLC with gantry angle was tested as part of the MVI panel test.

Waterphantom x and y profiles were collected at depths of 1.3, 5.0 and 10.0 cm and analysed to check whether the beam was vertical. Field edges defined by the point of inflection of the penumbra were analysed and compared. Precise overlap of the gantry 0° and gantry 180° beams was checked with an opposing fields film.

A check of the beam alignment based on relative FFF peak position was performed with gantry 0 and gantry 180 degree MLC-only half-beams (figure 5.4). A film in the coronal plane through isocenter was irradiated and x -profiles analyzed. The profiles were also co-registered based on the beam edges to check the position of the MLC bank (sides of the MLC). A check is also performed by Elekta to verify that the maximum field size in the y direction fits between the two halves of the MRI primary magnet.

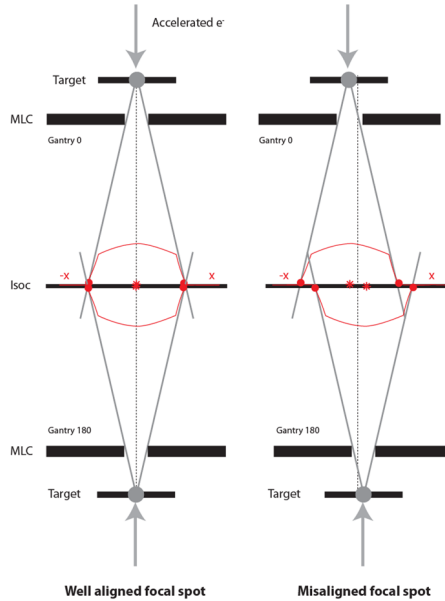


Figure 5.4: Schematic (front view) of the effect of a focal spot misalignment by using two opposed beams. Film check can be performed for jaw edges, MLC sides, and for FFF peak position (beam angle).

5.2.8 A5: Mechanical and dosimetric alignment of MLC and jaws

The operation and calibration of the Elekta Unity multileaf collimator (MLC) has been previously described and the transmission quantified (Woodings *et al.*, 2018a). The MLC and jaws were calibrated using the in-built Elekta workflows. The MLC and jaw calibrations were independently checked with UMCU tests (figure 5.2).

A stripe test with 1 mm leaf overlaps every 20 mm was measured with a film (between copper sheets) and the MVI over the range $-70 < y < +70$ mm for the central 56 leaf pairs. In-house software was used to assess the profile minimum due to relative leaf overlap, and the center of each overlap region (absolute positioning error) (Sastre-Padro *et al.*, 2004). The high-resolution EBT3 film data measured at isocenter was registered to the MVI image that was simultaneously acquired, so that the MVI-based coordinate system could be transferred to the film. A visual assessment of constancy was performed at gantry 0° for all 80 leaf pairs.

Average offsets and standard deviations were assessed and reported for each leaf pair and for each stripe. The jaws were verified with fluence film measurements of 50 mm wide stripes over the range -200 to $+150$ mm. The positions were evaluated using in-house software that finds the point of inflection of each edge. Maximum and average offsets and standard deviations were reported.

The stripe test was repeated at the cardinal gantry angles for the central 30 leaf pairs using the MVI.

5.2.9 A6: Table

Table orthogonality and precise movement are not critical for the MRI-linac, where each treatment is adapted based on the new position of the patient for each fraction. They are required for precise phantom setup. Orthogonality and movement with and without load (90 kg) were assessed. For three different indexed couch positions the Elekta geometry phantom was mounted, the couch moved to the predefined position and the phantom imaged. The position of the ball bearing was assessed using the in-built Elekta software. Residual translational offsets in the cardinal directions were recorded. Additional checks of orthogonality of the table and the table movement to the plane of the gantry were made using a set square, couch index bar and MVI images.

5.2.10 A7: Lasers

Lasers are not required for the MRI-linac as the treatment plan is adapted to the patient position for the current fraction. The system does include an indicative sagittal laser for approximate setup.

5.2.11 A8: MR to MV alignment

The rotational and translational offsets between the MRI coordinate system and the linac (MV) coordinate system were measured using the in-built Elekta workflow and the Elekta MR to MV phantom (figure 5.2). By using the pre-defined 3D MR imaging protocol (exam card) and the predefined x-ray beam sequence resulting in 31 MVI images, the MR to MV offset can be calculated using the in-built Elekta software. The rotational alignment must be within 0.3 degrees. The translational offset is entered into the Unity software environment so that the Monaco TPS can accurately place the MV isocenter within the MR dataset prior to adaptation of treatment plans.

5.2.12 A9: Dosimetric system

The linac was calibrated consistent with the Netherlands Code of Practice NCS18 (Aalbers *et al.*, 2008) with additional correction factors for the influence of the magnetic field (van Asselen *et al.*, 2018):

$$D_{w,Q}^B = c_B k_{B,M,Q} M_Q^B N_{D,w,Q_0} k_{Q,Q_0} \quad (5.3)$$

Where $D_{w,Q}^B$ is the absorbed dose to water, c_B is the ratio of dose with magnetic field over dose without magnetic field, $k_{B,M,Q}$ is the ratio of ionization reading without magnetic field over reading with magnetic field, M_Q^B is the ionization chamber reading with magnetic field corrected for influence quantities, and N_{D,w,Q_0} and k_{Q,Q_0} are the chamber calibration coefficient and beam quality correction factors.

The linac was calibrated to deliver 70.1 cGy per 100 MU at isocentre (143.5 cm) at 10 cm depth (SSD 133.5 cm) for a 10 x 10 cm² beam delivered from gantry 90°. This is equivalent to a D_{\max} of 100 cGy per 100 MU at $d_{\max} = 1.3$ cm under these reference conditions. The dose rate is automatically set to 425 MU/min with a pulse repetition frequency (PRF) of 275 Hz and a gun duty cycle of 71% (percentage of radio frequency pulses that are accompanied by gun pulses). The measurements were performed with both PTW30013 and IBA FC65-G Farmer-type waterproof chambers. The chambers were placed horizontally in an in-house built RW3 phantom, perpendicular to the radiation beam and anti-parallel to the magnetic field. The RW3 phantom factor was derived from comparisons of measurements in the RW3 phantom and the MP1 water phantom. The values of linac monitor chamber dose channels 1 and 2 were calibrated for 200 MU. Short term constancy was tested with 10 exposures in a row. Long term constancy was initially tested over a period of two weeks, with results here reported for a period of four months. Linearity with dose was tested over the range 2 – 1000 MU, and linearity with dose rate was tested for 54, 297 and 418 MU/min by varying the gun grid duty cycle between 10%, 50% and 71% (the standard operating value for this linac).

Profiles were tested for different gantry angles and for 5 MU and 100 MU using an ICprofiler on the Elekta rotating platform during installation. This system allows measurements to be acquired without the bridge or table affecting the beam. The crossline symmetry is expected to show greater variation due to (i) the Lorentz force shift of the profile (ie that the dose profile is intended to be slightly asymmetric) and (ii) variable transmission through the cryostat with gantry angle.

5.2.13 A10: Beam performance during MR imaging

Output and planar relative dose distributions were measured with and without simultaneous MR imaging to test constancy. A beam was delivered from gantry 0° to a film at isocenter at depth 10 cm. A typical imaging sequence was used: 3D Turbo gradient field echo (TFE) with resolution 2.5 x 2.5 x 5 mm³, repetition time (TR) 3.4 ms, echo time (TE) 2.0 ms, flip angle (FA) 12°, T1 contrast enhancement, 15 TFE shots, TFE factor 100, number of signal averages (NSA) 1. Radiofrequency (RF) power optimization and field (f₀) determination were switched off.

This test was repeated for the cardinal gantry angles with a 18x7 cm² beam imaged with the MVI.

Ion chamber measurements were performed without scanning, and during a number of different MRI scan sequences; 2D T2 turbo spin echo (TSE), T1 TSE and a diffusion weighted image (DWI).

5.2.14 A11: End to end test

An end-to-end test requires the whole system, not only the linac component and is therefore not strictly within the scope of this article. Nevertheless it is noted for the interest of the reader that an end-to-end test was performed using film in an Alderson

anthropomorphic phantom (last step in figure 5.2). The film position was defined by markers placed within the phantom. The lymph node plan was adapted based on the treatment position of the phantom. Dose magnitude and position were assessed.

5.3 Results

With only one photon energy, no flattened fields, no wedge and no electron beams, and with a beam line that is not user-adjusted, there are less acceptance tests than on a kV-IGRT linac. Some of the tests are new, but they are generally not more complex. When performed on the first Elekta Unity clinical system, the results of all tests were acceptable for clinical use. Test results for each category are presented below.

5.3.1 Safety

The safety tests were passed.

Changing the gun grid voltage to deliberately induce a fault condition changed the beam dose rate, output, quality and profile causing an inhibit. Within the deliverable range, the maximum change in $TPR_{20,10}$ was 0.4%, in output was 1.8%, and in off-axis dose was 1.3% (maximum point difference within the central 80% of field size of a 30 x 22 cm² beam). Thus the internal inhibits were effective in preventing the beam from deviating substantially from its calibrated state.

5.3.2 Radiation shielding

All doses were within the national and international regulated limits. Within the patient plane, the highest measured leakage dose was 0.02% of the in-field dose, within the 0.2% (max) and 0.1% (average) specification (International Electrotechnical Commission, 2009). Neutron readings were at the background level.

5.3.3 MVI

The position (rigidity) of the MV imaging panel had a standard deviation of 0.06 mm u and 0.03 mm v . Field edges were also constant to within 0.07 mm. Assuming no synchronization between focal spot shift, gantry ellipticity, MLC shift and panel shift, the panel rigidity is better than $1\sigma = 0.06$ mm. The angles of the MV image pixel columns relative to the water surface were each measured to be $\alpha_{90} = \alpha_{270} = 0.5/400$ pixels = $+0.072^\circ$ and from equations 5.1 and 5.2 gantry tilt (θ_{gantry}) was calculated to be $0.0 \pm 0.1^\circ$ and MVI panel rotation (ϕ_{MVI}) was calculated to be $0.07 \pm 0.1^\circ$. The MVI rotational misalignment could conceivably be taken into account in the evaluation of other acceptance tests. However, here it was established that installation of the panel was accurate (within 0.1 degrees) and the rotation was then considered negligible for other tests.

The MVI pixel scale was determined to be 0.2519 mm / pixel, with no difference in the u and v directions and therefore no panel tilt. MVI panel isocenter coordinates ($u_{\text{isoc}}, v_{\text{isoc}}$)

were determined to be (512.01, 651.64) (with origin pixel (1,1)). For use on the MVI display (with a (0,0) origin) the isocenter coordinates are (511.01,650.64). Independent UMC Utrecht measurements determined $(510.5 \pm 1.2, 652 \pm 12)$, where the u uncertainty is 2σ (standard deviation with coverage factor $k = 2$) and the v uncertainty is estimated assuming a water phantom setup uncertainty of 0.1° . The Elekta and UMCU results are consistent. The Elekta values were applied for all further tests.

The modulation transfer function (MTF) was equivalent to 0.3 line pairs per mm, consistent with the results from conventional linear accelerators (0.4 lp/mm), taking into account the extended SAD, detector distance, focal spot size and magnification factor. This is consistent with previously published results from the MRI-linac prototype (Raaymakers *et al.*, 2011).

5.3.4 Mechanical and dosimetric alignment of gantry, focal spot and beam

Gantry rotation and readout were assessed. The direct angle measurements at 270° and 240° agreed within $0.1 \pm 0.1^\circ$. The relative gantry angles measured from the spoke film had standard deviation 0.13° and maximum deviation 0.25° all $\pm 0.35^\circ$.

Gantry tilt was determined by spirit level and by laterally imaging a water surface. Both methods were consistent that the gantry tilt was $0.0 \pm 0.1^\circ$.

Waterphantom x and y profiles were analysed to check whether the beam was vertical based upon analysis of the beam edges (figure 5.5). The Lorentz force creates a constant $+x$ offset at each depth. The center of the crossline scans (based on field edges) shifted by -0.2 mm and the center of the inline scans by -0.4 mm, implying that the ‘vertical’ beam was travelling at an angle of $0.13 \pm 0.2^\circ$ around the y axis and $-0.26 \pm 0.2^\circ$ around the x axis. The test is dependent upon the reproducibility of the gantry angle ($< 0.1^\circ$), the water phantom setup ($< 0.1^\circ$) and the small range of depths measured (1.3 – 10 cm) ($< 0.1^\circ$). The combined uncertainty in the determined angle is $< 0.2^\circ$. The clinical impact of an error of 0.3° is a worst-case 1 mm error in the beam location at a distance of 200 mm from isocenter.

From the MVI rigidity measurements at different gantry angles, the average MLC field center was $(u, v) = (0.01, 0.09)$ mm from the Elekta defined isocenter position. The standard deviation around this average position was $\sigma = (0.07, 0.06)$ mm. This implies that the MLC origin was well matched to the isocenter, and that the position was valid over all gantry angles. The film to check beam alignment showed that the focal spot was centrally aligned between the MLC sides, with an acceptable offset of 0.3 mm.

The gantry 0° beam FFF peak crossed the patient plane (coronal plane through isocenter) at $x = -1.6$ mm from isocenter corresponding to a beam angle of 0.06 ± 0.1 degrees, which was considered acceptable. Uncertainty in the measurement is due to noise, potential systematic effects in the film and film scanner, and the gentle slope of the MRI-linac FFF beam. Adjustment of the direction of the MRI-linac beam requires physical movement

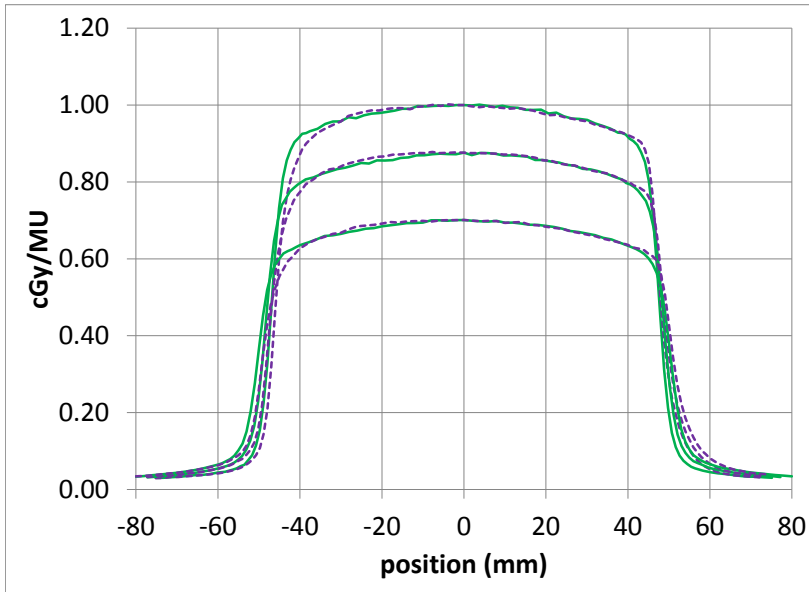


Figure 5.5: Inline (green, solid) and crossline (purple, dashed) profiles at 1.3, 5 and 10 cm depth for a $10 \times 10 \text{ cm}^2$ beam.

of the waveguide and is thus intended to be done only at installation.

The opposing fields film showed that the beam centers from gantry 0° and gantry 180° were aligned to within 0.63 mm crossline and -0.13 mm inline.

The field sizes of the opposing fields were also measured. The maximum difference was 0.6 mm, which was within the tolerance of 2 mm (1 mm per field edge). The locus of isocenter was measured with a spoke film (see figure 5.6). The radius of the locus was 0.38 mm.

5.3.5 Mechanical and dosimetric alignment of beam limiting devices

The MLC was first assessed at gantry 0° . Over 8 different MLC abutment positions, and for 56 leaf pairs, the average absolute positional deviation from the set position was 0.29 mm, with standard deviation 0.41 mm (see figure 5.7). Average relative error between leaf pairs in a stripe was 0.17 mm. Leaf pair 55 had the largest average absolute positional error of 0.8 mm over all positions.

The visual inspection of all 80 leaf pairs imaged from gantry 0° passed. The x-jaw po-

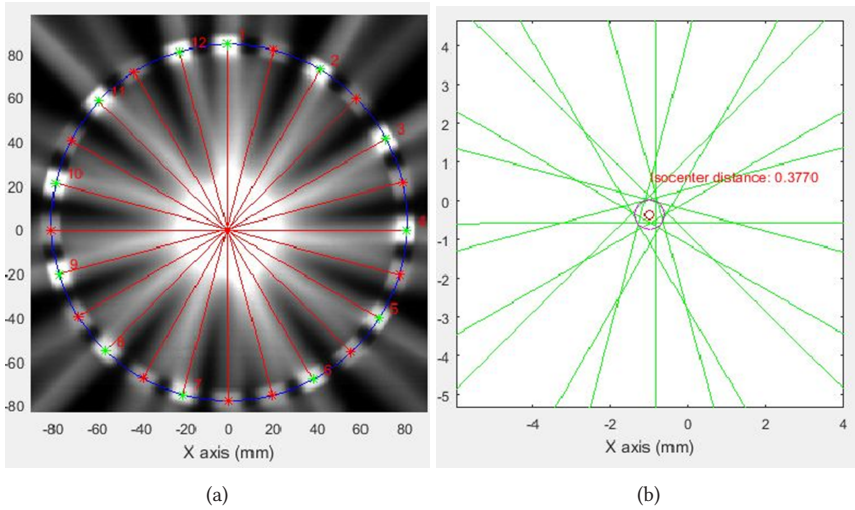


Figure 5.6: (a) Spoke film acquired with copper rings to assess photon fluence free of Lorentz force interference, and (b) the radius of the locus of isocenter was 0.38 mm.

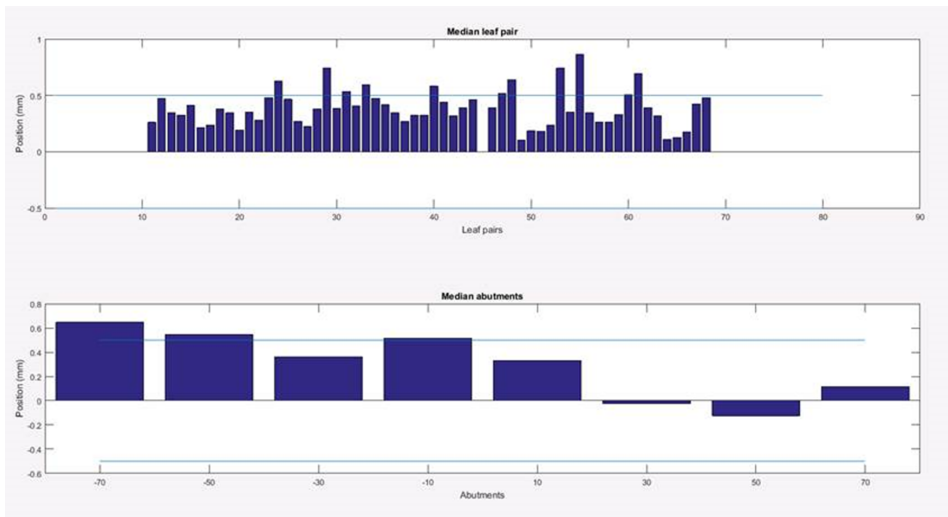


Figure 5.7: Top — absolute positional error for each leaf pair, averaged over all abutment positions (14 cm region). Bottom — error for each abutment position, averaged over all leaf pairs.

sitions were measured over the range -200 mm to +150 mm. The maximum deviation from the intended position was 0.9 mm. The average deviation was 0.16 mm. These are well within the traditional specification of 1% (1 mm per 100 mm distance from center).

MLC stripe fields were repeated at gantry 0, 90, 180 and 270 degrees and measured with the MVI, covering 22 cm (30 leaf pairs). The average absolute positional MLC errors, with

standard deviations in brackets, were respectively 0.10 (0.23), 0.07 (0.22), -0.08 (0.22) and -0.02 (0.23) mm.

5.4 Table

The table position was checked through a range of motion of 1280 mm. Residual errors in the translational axes were measured. The largest residual error in each (x, y, z) direction was (0.2, 0.4, 0.1) mm. This was within the hospital specification of 1 mm.

Table orthogonality to the gantry plane of rotation was verified by imaging an index bar. The index bar was parallel to the MV image pixel rows to better than 1 pixel in 200 mm (< 0.07 degrees). A set square was used to verify that the index bar was at right angles to the tabletop.

The height of the radiation isocentre above the table top was measured with a spoke film. It was 0.0 ± 0.5 mm different from the nominal value of 140 mm.

5.4.1 Lasers

The Elekta indicative sagittal laser is not intended for precision setup. The laser was aligned in a sagittal direction passing through isocenter, suitable to assist with approximate patient setup.

5.4.2 MR to MV alignment

The rotational and translational offsets between the MRI coordinate system and the linac (MV) coordinate system were measured. The rotational differences were (ψ, ϕ, θ) = (-0.04, +0.03, +0.09) degrees. No correction was applied for the rotational differences. The translational correction was (x, y, z) = (-0.51, -0.52, +0.30) mm.

5.4.3 Dosimetric system

The linac was calibrated consistent with the Netherlands Code of Practice NCS18 (Aalbers *et al.*, 2008) with additional correction factors for the influence of the magnetic field (van Asselen *et al.*, 2018).

The linac was reproducible in the short term with standard deviation 0.07%. Linac monitor channel 1 was perfectly 100 MU for each beam (as intended). Monitor channel 2 was always within 0.1 MU (0.1%).

Over a two week period with 10 measurements, the average measured dose was $100.1 \pm 0.2\%$ (1σ) of the calibrated value. No trend was apparent. The doses were independent of air pressure.

As part of on-going QA, measurements were routinely performed with Farmer chamber and MVI over a four month period. From analysis of the standard deviations of the differ-

ences of the measurements, it was determined that the standard deviations attributable separately to each of the Farmer chamber and RW3 phantom, MVI and linac were $\sigma = 0.45\%$, 0.27% and 0.27% respectively. The MV imager pixel factor was a valid representation of the phantom-measured dose and was implemented as a convenient daily dose check.

Linearity with dose was tested over the range 2 – 1000 MU. The difference in cGy/MU for a 5 MU beam was $+1.3\%$, which is within the 2% specification. The difference was less than 0.4% for all longer beams, within the 1% specification. Within each cardinal gantry angle the maximum deviation for 5 MU was less than 1.3% .

Linearity with dose rate was tested for 54, 297 and 418 MU/min. The maximum deviation for different dose rates, and within each cardinal gantry angle was 0.1% .

Inline and crossline IEC symmetry were measured by Elekta with an ICprofiler 2D array on a rotating platform, every 30° . The inline symmetry was in the range $100.4 - 100.9$. The crossline symmetry was in the range $100.7 - 102.1$. These values were all within the traditional specification of 3% and demonstrated acceptable beam constancy with gantry angle.

The measurements were repeated for the cardinal gantry angles with 5 MU and 100 MU. The differences in symmetry for the low-MU beams were all less than 0.4% . The maximum in-field point difference between any beam and the gantry 0° 100 MU beam was 0.8% .

5.4.4 Beam performance during MR imaging

With and without MR imaging, the profiles from the films were in excellent agreement (figure 5.8). The maximum difference at any point within the beam was 1.1% , consistent with the combined uncertainty of the film measurement and the beam reproducibility.

For the cardinal gantry angles, the maximum difference within the beam, as measured with the MVI, was 0.5% .

Ion chamber measurements were made with and without simultaneous MR imaging. The maximum difference in average readings was -0.13% .

From the ion chamber and film measurements it is concluded that radiation delivery and dose deposition, as expected, are not significantly affected by simultaneous MR imaging.

5.4.5 End to end test

Coordinates and orientations were consistent throughout the Unity system. Gamma test with $5\%/2\text{mm}$ parameters and 10% background threshold (SBRT criteria) had 99.8% agreement. Visual inspection of the film exposed within the Alderson phantom showed

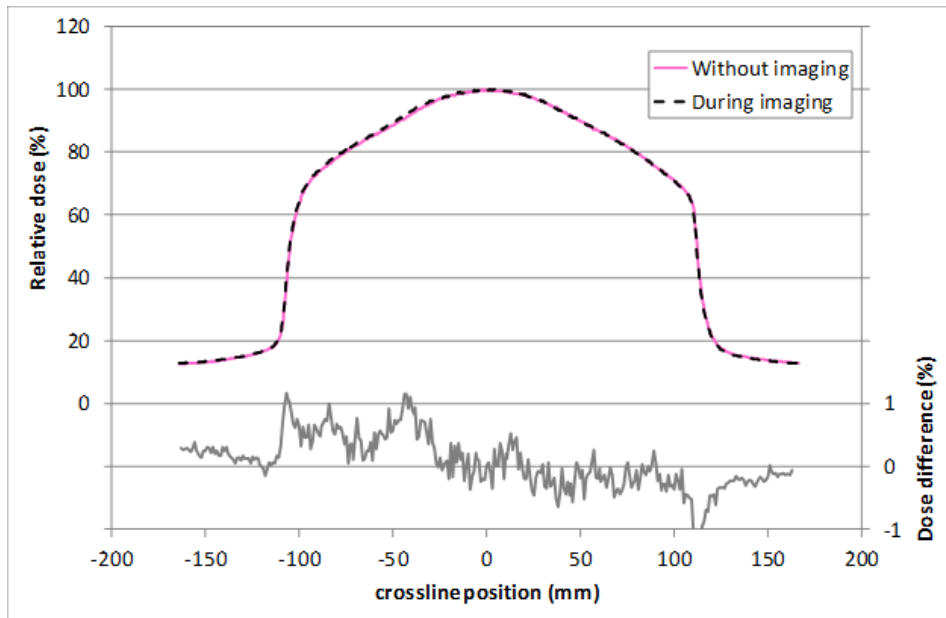


Figure 5.8: Relative crossline dose profiles and differences, with and without simultaneous MR image acquisition. To within the uncertainties of film dosimetry the profiles are identical.

the dose centered on the target marker. The offset between the co-registered film and TPS dose distributions was less than 1 mm.

5.5 Discussion

Linac acceptance testing results were acceptable for clinical introduction.

Acceptance tests must be followed by beam data collection, Elekta beam modeling and commissioning (Woodings *et al.*, 2018a). For the MRI-linac, beam data collection must include attention to magnetic field related effects such as electron streaming (Malkov *et al.*, 2019) and electron return effect (Raaijmakers *et al.*, 2005). Deep PDDs should be acquired with lateral beams, or by stitching together multiple measurements (Woodings *et al.*, 2018a).

Cryostat transmission may vary from one Unity system to the next. It may also vary by 0.6% based on how much helium is in the cryostat. The helium is recycled within the system therefore the helium level does not change appreciably over time, only potentially during specific events (for example magnet ramp-up). Thus cryostat transmission and helium level must be checked during commissioning (Woodings *et al.*, 2018a).

Table and receiver coil transmission are expected to be the same for all Unity systems. They should be checked as part of the acceptance and commissioning process (Woodings

et al., 2018a).

Patient stabilization and support device transmission should be considered as part of the commissioning process. At UMCU transmission through foam supports and vacuum mattress were considered negligible and not included in the dose calculations, consistent with our approach in the regular clinic.

The acceptance testing results were used to establish a baseline for future QA tests.

5.6 Conclusion

New tests for the MRI-linac were developed, implemented and are described here. The MRI-linac meets safety requirements for patients and operators. The system delivers radiation for SBRT effectively.

5.7 Acknowledgments

The authors wish to acknowledge the support of the Dutch Cancer Society for this work.

5.8 Conflict of interest

David Roberts is an employee of Elekta Limited. UMC Utrecht is a research partner of Elekta AB.

The authors have no conflicts of interest to disclose.

CHAPTER 6

Beam characterisation of the 1.5 T MRI-Linac

The following chapter is based on:

Woodings S.J., Bluemink J.J., de Vries J.H.W., Niatsetski Y., van Veelen B., Schillings J., Kok J.G.M., Wolthaus J.W.H., Hackett S.L., van Asselen B., van Zijp H.M., Pencea S., Roberts D.A., Lagendijk J.J.W. and Raaymakers B.W. 2018a Beam characterisation of the 1.5 T MRI-linac *Physics in Medicine and Biology* 63 085015

Abstract

As a prerequisite for clinical treatments it was necessary to characterize the Elekta 1.5 T MRI-linac 7 MV FFF radiation beam. Following acceptance testing, beam characterization data were acquired with Semiflex 3D (PTW 31021), microDiamond (PTW 60019), and Farmer-type (PTW 30013 and IBA FC65-G) detectors in an Elekta 3D scanning water phantom and a PTW 1D water phantom. EBT3 Gafchromic film and ion chamber measurements in a buildup cap were also used. Special consideration was given to scan offsets, detector effective points of measurement and avoiding air gaps.

Machine performance has been verified and the system satisfied the relevant beam requirements of IEC60976.

Beam data were acquired for field sizes between 1×1 and $57 \times 22 \text{ cm}^2$. New techniques were developed to measure PDD curves including the electron return effect at beam exit, which exhibits an electron-type practical range of $1.2 \pm 0.1 \text{ cm}$. The Lorentz force acting on the secondary charged particles creates an asymmetry in the crossline profiles with an average shift of $+0.24 \text{ cm}$. For a $10 \times 10 \text{ cm}^2$ beam, scatter from the cryostat contributes 1% of the dose at isocentre. This affects the relative output factors, scatter factors and beam profiles, both in-field and out-of-field. The average 20 – 80% penumbral width measured for small fields with a microDiamond detector at 10 cm depth is 0.50 cm. MRI-linac penumbral widths are very similar to that of the Elekta Agility linac MLC, as is the near-surface dose $\text{PDD}(0.2 \text{ cm}) = 57\%$. The entrance surface dose is $\sim 36\%$ of D_{max} . Cryostat transmission is quantified for inclusion within the treatment planning system.

As a result, the 1.5 T MRI-linac 7 MV FFF beam has been characterised for the first time and is suitable for clinical use. This was a key step towards the first clinical treatments with the MRI-linac, which were delivered at University Medical Center Utrecht in May 2017 (Raaymakers *et al.*, 2017).

6.1 Introduction

At University Medical Center Utrecht a linear accelerator (linac) with integrated magnetic resonance imaging (MRI) has been developed as part of a collaboration with Elekta AB (Stockholm, Sweden) and Philips (Best, The Netherlands). This combination facilitates simultaneous irradiation and high-precision image guidance with soft-tissue contrast (Legendijk *et al.*, 2014). The Elekta clinical magnetic resonance linac (MRI-linac) is an upgraded version of the machine described by Raaymakers *et al.* (2009). The 1.5 T magnetic field points out of the entrance of the bore, and is at all times at 90 degrees to the 7 MV radiation beam delivered from the linac mounted on its ring gantry.

The magnetic field affects the dose deposition within a phantom and/or patient within the MRI-linac. The Lorentz force acts on charged particles, pulling them in a direction orthogonal to their current motion and the magnetic field, which perturbs the dose deposition kernel (Raaijmakers *et al.*, 2005). This has a small effect inside and outside the radiation beam, but is clearly noticeable at the lateral edges of each beam. The radiation beam passes through the MRI cryostat which provides an additional source of beam flattening and of photon scatter.

For adaptive radiotherapy, high precision imaging and dose painting (Legendijk *et al.*, 2014), it is a key requirement that the MRI-linac beam, including its penumbra, is accurately measured, characterized and modelled.

Radiation distributions were measured with 1D and 3D scanning water phantoms, EBT3 Gafchromic film and ion chamber measurements in a build up cap, in order to fully characterise the beam.

The aims of this work were to:

1. Assess the MRI-linac treatment capabilities prior to clinical use;
2. Assess the MRI-linac radiation beam against international standards for medical radiation beams;
3. Characterise the MRI-linac radiation beam such that it can be modelled in the Monaco treatment planning system (TPS); and
4. Compare the MRI-linac radiation beam to a current-generation Elekta Agility radiation beam.

6.2 Materials and Methods

All irradiations within a magnetic field were delivered with a 7 MV flattening filter free (FFF) beam produced by an Elekta MRI-linac (Elekta AB, Stockholm, Sweden). The system has a source axis distance (SAD) of 143.5 cm with a fixed-height couch with solid

surface nominally 14 cm below isocentre. The reference conditions for absolute dosimetry were 69.6 cGy per 100 MU at a depth of 10 cm with an SSD of 133.5 cm and a field size of 10 x 10 cm² at isocentre, approximately equivalent to 100 cGy per 100 MU at the d_{max} of 1.3 cm. During these experiments the dose rate was 425 or 530 MU/min.

6.2.1 Special characteristics of the MRI-linac

6.2.1.A Magnet and radiation field size

The MRI closely resembles the Philips Ingenia system however a ring gap has been created within the magnet so that the radiation beam can pass inbetween. This allows a maximum field size in the longitudinal direction (IEC61217 y) of 22 cm. Due to the extended SAD a field size of up to 57.4 cm can be achieved in the lateral direction (IEC61217 x).

The magnet stretches across the plane of linac gantry rotation via a superconducting wire in a conduit. This wire is centered within the beam at a gantry angle of 13 degrees. Direct irradiation of this wire is excluded by the system. Thus field size limitations exist for some beams delivered from between gantry 9 – 17 degrees.

6.2.1.B Cryostat and body coil

The radiation beam passes through the helium cryostat and MRI body coil. These have been designed to be as homogeneous as possible. They flatten the beam and are a source of a small amount of scattered radiation. See section 6.2.8 for more information.

6.2.1.C Couch and treatment angles

The couch supports only longitudinal motion for patient setup. Thus there is no ability to adjust a patient position for an existing treatment plan. The MRI-linac is fundamentally an image-guided radiotherapy system. Dose *must* be optimised based on images acquired of the patient in their current treatment position. This also means that the isocentre will typically not be within the target region and the MRI-linac will routinely deliver small off-axis radiation fields.

The linac gantry cannot tilt and the couch cannot rotate so all MRI-linac treatments are co-planar.

6.2.1.D Delivery modes

In its initial clinical configuration, the MRI-linac delivers step-and-shoot intensity modulated radiation therapy (IMRT). Dynamic treatments will be supported in a future release. Thus variable dose rate and multileaf collimator (MLC) leaf speed are not important factors in this initial release. The MLC is based on the Elekta Agility model with 80 leaf pairs with rounded leaf ends, each with projected width of ≈ 0.72 cm at isocentre, although the MRI-linac has the additional capability to park opposing leaves underneath the primary collimator. The MLC is fully inter-digitating and can thus create island fields for

simultaneous irradiation of multiple target regions. Minimum opposing leaf separation is set to 0.5 cm in the initial configuration.

6.2.2 Phantoms

There are special considerations for phantoms and detectors within a high-magnetic field environment. Phantoms must contain minimal ferromagnetic materials, including standard electric motors, power supplies, batteries, electronics and drive arms (Smit *et al.*, 2014b). Air cavities must be eliminated to avoid the effects of small air cavities around detectors (Hackett *et al.*, 2016; O'Brien *et al.*, 2017; Malkov *et al.*, 2017).

Beam characterisation data were acquired with five phantoms:

- An Elekta-Philips-PTW prototype MR-compatible MP3-style scanning water phantom, whose design was based on an earlier prototype (Smit *et al.*, 2014b);
- A prototype PTW MR-compatible MP1 (1D) water phantom (PTW, Freiburg, Germany) with a manual depth drive;
- A 20 x 20 x 10 cm³ water block with a perforated Farmer chamber sleeve to allow water around the chamber;
- A RW3 phantom consisting of multiple 30 x 30 x 1 cm³ slabs (with water-filled cavities);
- A polymethylmethacrylate (PMMA) buildup cap with diameter 4.3 cm (with water-filled cavity), used with a Farmer chamber for comparison of radiation beams from different gantry angles.

6.2.3 Detectors

The readings in air-filled ion chambers are dependent on the relative orientations of radiation beam, magnetic field and chamber axis, and on chamber size, beam energy and field strength. These differences are due to the varying average path length of the ionising track of a secondary charged particle and the inflow of electrons into the chamber (Meijsing *et al.*, 2009). Additional correction factors are required for absolute dosimetry (Smit *et al.*, 2013; Reynolds *et al.*, 2013; O'Brien *et al.*, 2016; de Prez *et al.*, 2016b; Wolthaus *et al.*, 2016b; Spindeldreier *et al.*, 2017). Relative dosimetry measurements in a scanning water phantom within the expected range of conditions can still be made with < 0.3% error due to chamber orientation (Smit *et al.*, 2014b).

PTW30013 and FC65-G (IBA-Dosimetry, Schwarzenbruck, Germany) Farmer-type waterproof chambers were used with collecting voltage -250 V for absolute dosimetry. PTW31021 Semiflex 3D detectors were used with collecting voltage -200 V for medium and large field measurements. Data were acquired with a standard effective point of measurement (EPoM) of -0.14 cm ($-0.6 \times r_{\text{cy1}}$) (Andreo *et al.*, 2000), however this was

corrected to -0.05 cm for the MRI-linac percentage depth dose (PDD) curves, consistent with local analysis and with the microDiamond results (Woodings *et al.*, 2018b). PTW60019 microDiamond detectors were used with 0 V and an EPoM of 0.10 cm for small-field measurements and for assessing beam penumbra (Woodings *et al.*, 2018b). A PTW Tandem electrometer was used with the PTW MP3 phantom for collecting profile data. Unidos E and Unidos Weblin electrometers were used for point data collection.

A PTW31010 Semiflex detector was used as a monitor (reference) ion chamber. The chamber was taped at the top of the bore inside the corner of a 5 x 5 cm² field. Linac output fluctuations were assessed with an IBA CC08 ion chamber mounted by the linac waveguide.

6.2.4 Acceptance testing

Prior to beam characterisation it was necessary to test the basic performance of the MRI-linac system including geometric alignment. The system passed all tests (van Zijp *et al.*, 2016; Wolthaus *et al.*, 2016b; Raaymakers *et al.*, 2017).

Acquisition of MR images during radiation delivery is not expected to effect the dose distribution. To confirm that the radiofrequency pulse sequences and gradient magnetic fields have no effect, dose planes were measured with EBT3 Gafchromic film, and linac output and beam quality (TPR_{20,10}) were measured with an ion chamber, before and during MR image acquisition.

6.2.5 Beam requirements (IEC60976)

IEC 60976 mathematically defines flatness, symmetry and deviation and requires therapeutic MV x-ray beams to meet specifications. For the 7 MV FFF beam of the MRI-linac these specifications of flatness and deviation do not apply. The beam symmetry can be measured but not properly assessed with water phantom scans in the crossline (x) direction due to the influence of the Lorentz force on the electrons and the resultant asymmetric dose distribution. Beam symmetry in the inline (y) direction was evaluated for 10 x 10 and 57 x 22 cm² fields at depths of d_{\max} and 10 cm (isocentre).

6.2.6 Beam quality

Beam quality was characterised as per NCS 18 (Aalbers *et al.*, 2008) and IAEA TRS 398 Andreo *et al.* (2000) using tissue phantom ratio TPR_{20,10} with the detector EPoM at isocentre. Percentage depth dose (PDD) ratios at 20 cm and 10 cm were measured for a source-surface distance (SSD) of 123.5 cm for determination of PDD_{20,10}. These values are insensitive to the presence of the 1.5 T magnetic field.

It is noted that TG51 Almond *et al.* (1999) uses PDD (10cm) for beam quality. This value is not useful for the MRI-linac because both the position of d_{\max} and the dose D_{\max} are significantly altered by the magnetic field even though the photon spectrum and penetrative quality are unchanged.

6.2.7 Data for the treatment planning system

6.2.7.A Techniques

1-D profiles were acquired as shown in table 6.1. Horizontal profiles included crossline (x) and inline (y) profiles at depths of 1.3, 5, 10, 12 and 17 cm. Diagonal profiles were acquired only for the 57 x 22 cm² field at angles of ± 21.1 degrees.

Field size $x \times y$ (cm ²)	PDD and horizontal profiles	
	Semiflex 3D	microDiamond
1 x 1		✓
2 x 2	✓	✓
3 x 3	✓	✓
5 x 5	✓	✓
4 x 14	✓	
14 x 4	✓	
10 x 10	✓	✓
15 x 15	✓	
20 x 20	✓	
22 x 22	✓	
40 x 22	✓	
57 x 22	✓	

Table 6.1: Summary of 1-D data collected for the treatment planning system.

Due to limitations on water phantom size and geometry, deep PDDs and large profiles required detectors to be positioned in two holder locations. Multiple profiles were then stitched together using custom software to create the simple PDD, crossline or diagonal scans. PDDs were stitched together by rescaling the deeper PDD to match the shallower PDD at isocentre (10 cm depth). Stitching was required for crossline and diagonal scans for field sizes of 15 x 15 cm² and greater. In these cases the profile from the +x side was matched to the profile on the -x side in the region of overlap of the profiles, with small adjustments in gain and positional offset.

Crossline profiles were acquired first, in order to determine the offset of the peak dose (or plateau region) from beam central axis (CAX), both near the surface and at depth. This crossline offset was then implemented for the inline profiles, PDDs and relative output factors. For fields 4 x 4 cm² and larger the offset made no difference to the data collection. For smaller field sizes, offsets of $x = +0.1$ cm (1 x 1 cm²) and $x = +0.2$ cm (2 x 2 and 3 x 3 cm²) were used. No significant offset variation with depth was observed.

For most scans a monitor chamber was used to remove any fluctuations in linac output. For the smallest fields this was not possible. In order to remove any possible systematic effects due to linac dose rate drift all small field profiles were acquired in both directions and then checked to confirm that the scans were consistent.

6.2.7.B PDDs

Due to the electron return effect (ERE) (Raaijmakers *et al.*, 2005), the PDD curve at the beam exit is more complex and of more interest than for a beam without magnetic field. Direct ion-chamber measurement of the exit PDD is now achievable on the MRI-linac because a gantry-180° beam can be directed up through the scanning water phantom located on the couch.

Stitching the exit PDD and the regular PDD together is non-trivial because: (i) the SSDs of the two measurements are different and must be corrected, which can be achieved with the Mayneord F factor (Khan, 1994); (ii) use of the Mayneord F factor requires the G180° beam sizes to be scaled by $(SSD_{G0^\circ} / SSD_{G180^\circ})$ so that the beam-entry scatter conditions are consistent; (iii) even though the cylindrical Semiflex3D ion chamber is suitable for both G0° and G180° measurements, the correction for the effective point of measurement must be reversed.

6.2.7.C Profiles

Diagonal profiles were measured only for the largest 57 x 22 cm² beam. These were used to assess the beam fluence across the largest possible off-axis distance.

Small off-axis beams are important for the MRI-linac because the system is designed for the patient to be approximately centered within the bore, and therefore target regions could be away from isocentre. 1-D profile data and point data were acquired for several small fields for TPS evaluation.

Beam penumbra is an important parameter for stereotactic-type high-precision treatments. Characterising the penumbra is not trivial for an FFF beam, where the beam peak and the beam shoulder are at different dose levels. The most popular solution, whereby the shoulder is normalised to 100%, is only well defined where the linac has both FFF and normal (flattening filter) beams that can be compared (Fogliata *et al.*, 2012). The MRI-linac has FFF only, thus this solution is not applicable.

Here, the method of Budgetell *et al.* (2016) is used, whereby a profile is divided by the profile of the fully open FFF field to artificially flatten the profile. The resultant processed profile has lost its in-field shape, but retains its penumbra data, which can be processed using normal methods. Jaw and MLC penumbra were quantified with a 20 – 80% width.

6.2.7.D Relative output and scatter factors

Relative output factors (ROF) were measured with the detector EPoM at a depth of 10 cm (depth of isocentre). A microDiamond was used for 1 x 1 – 10 x 10 cm² fields, overlapping with a Semiflex 3D used for 2 x 2 – 57 x 22 cm² fields. All ROFs were measured with a detector offset of $x = +0.25$ cm from central axis (CAX), except for the 1 x 1 cm² beam where the offset was 0.2 cm. For the 1 x 1 – 3 x 3 cm² beams this was important in order to measure at the position of maximum dose and minimum dose gradient, which

is shifted from CAX due to the Lorentz force. This position was verified with crossline scans prior to the ROF measurement.

In-air scatter factors were also measured with a Semiflex 3D chamber in a brass build up cap for $3 \times 3 - 57 \times 22 \text{ cm}^2$ beams. The detector was placed with chamber centre at isocentre. No lateral offset was made as the range of the secondary charged particles in the brass buildup cap is negligible.

6.2.8 Cryostat scatter

The cryostat and body coil (hereafter cryostat) are expected to behave as a combined attenuator and scatter source. The effect is not as strong as a traditional cone-shaped flattening filter where the beam is attenuated most on beam central axis. The profiles sit between those of conventional flattened field and FFF beams.

The scatter from the cryostat is evident in the scatter factors (section 6.2.7.D) and in the profile tails of large fields (figure 6.6b). For this reason additional measurements were made in air with Farmer chamber and build-up cap to assess both the scatter contribution outside the field and the effective SSD. The chamber and build-up cap were supported on foam at isocentric height and were moved in 5 cm steps laterally across the bore. The chamber was irradiated with 5×5 , 10×10 , 20×20 and $40 \times 22 \text{ cm}$ fields from gantry 0° and 90° . The readings from the gantry 0° beam were used to assess scatter (collimator and cryostat) outside the beam. The in-field readings from the gantry 90° beam were used to assess (i) the change in dose with distance from the source, (ii) whether this was consistent with a dual target and cryostat source model, and thus (iii) the relative quantity of radiation scattered from the cryostat.

6.2.9 Cryostat transmission

Cryostat transmission as a function of gantry angle was assessed. The Farmer chamber and build up cap were located at isocentre, suspended off the end of the couch. 100 MU, $10 \times 10 \text{ cm}^2$ beams were delivered from gantry angles at 2 degree intervals, with the exception of the region 9 – 17 degrees where the Elekta system inhibits radiation (see section 6.2.1). Linac output was simultaneously measured with the independent CC08 ion chamber mounted next to the waveguide.

6.2.10 MLC characterisation

The multileaf collimator (MLC) is constructed and operates on similar principles to the Elekta Agility MLC. The leaves are driven by individual motors in a feedback loop with the optical system. Each leaf has a fluorescent ruby on its upper surface. There are also reference rubies mounted on each leaf bank. Ultraviolet LEDs illuminate the rubies which fluoresce. This light is then monitored by the camera and used to adjust the leaf position. The camera and system undergo coarse and fine optics calibrations to correct for distortions in the image. The physical offset between ruby and leaf tip is determined for each leaf by moving the leaves to end stops. A polynomial correction is used for

the rounded leaf ends. Finally MLC-delimited stripe fields (Sastre-Padro *et al.*, 2004) are imaged on the in-built rigidly-mounted MV imaging panel to determine a radiation calibration that corrects for the offset between mechanical head centre and radiation field centre.

The penumbra of the MLC leaves were characterised with microDiamond detector profiles acquired in the MP3 water phantom.

6.2.11 Linac calibration

The linac was calibrated consistent with the Netherlands Code of Practice NCS18 (Aalbers *et al.*, 2008) with additional correction factors for the influence of the magnetic field (Wolthaus *et al.*, 2016b; Smit *et al.*, 2013). The linac was calibrated to deliver 69.6 cGy per 100 MU at isocentre (143.5 cm) at 10 cm depth (SSD 133.5 cm) for a 10 x 10 cm² beam delivered from gantry 90 degrees. This is equivalent to a D_{\max} of 100 cGy per 100 MU at $d_{\max} = 1.3$ cm under these reference conditions.

The measurements were performed with both PTW30013 and IBA FC65-G Farmer-type waterproof chambers. The chambers were placed vertically, perpendicular to both the radiation beam and the magnetic field.

6.2.12 Surface dose

For the MRI-linac the entrance dose at the patient surface is expected to be higher due to cryostat scatter and due to helical trajectories of electrons scattered out of the patient. On the other hand there will be less dose from electron contamination from the linac head and cryostat because the shower of charged particles will be curved away by the magnetic field. For beams entering the patient through other materials, such as the couch, the entrance dose is expected to be near D_{\max} .

As described in section 6.2.7.B, the exit surface dose is expected to be increased by the electron return effect (Raaijmakers *et al.*, 2005).

Entrance surface dose on the MRI-linac was measured with film in an RW3 phantom. The film was arranged in a coronal plane, parallel to a gantry 90° beam, but offset 0.3 cm from beam central axis so that no primary photon ray-line travelled down the length of the film. Film profiles were extracted using custom software and rescaled to match Semiflex 3D water phantom profiles. Surface doses at a depth of 0.0 cm are reported.

PDD (0.2 cm) from ion chamber measurements for 10 x 10 cm² fields at SSD 133.5 cm (MRI-linac) and 100 cm (Agility) are also reported.

6.3 Results and discussion

6.3.1 Acceptance testing

The MRI-linac beam characteristics (TPR_{20,10} and coronal plane dose distribution for a 10 x 10 cm² beam at 10 cm depth) were not affected by the simultaneous acquisition of echo planar imaging (EPI) or turbo spin echo (TSE) MR images. Surface dose was not explicitly measured during MRI imaging, but no variation is expected.

6.3.2 Beam requirements (IEC60976)

Beam symmetry in the inline (y) direction for 10 x 10 and 57 x 22 cm² fields at depths of d_{\max} and 10 cm (isocentre) was in all cases better than 100.5%, and thus within the IEC specification of 103%. Crossline (x) scans were also evaluated, including the asymmetric effect of the Lorentz force. Crossline symmetries were all better than 101.7%.

It is noted that, due to the FFF beam shape and the Lorentz force crossline asymmetry, the standard (IEC 60976) methods of evaluating profile shape, as well as profile QA, are no longer valid. New methods are required. Flatness, symmetry and deviation could be replaced with a profile matching concept such as dose difference within the central 80% of the nominal field size (FS) with respect to reference profiles:

$$\max_{|y_x \leq 80\%FS} [|D_{x,\text{measured}} - D_{x,\text{ref}}|/D_{\text{norm}}] \leq 1\%$$

where D_{norm} is the normalization value, usually equal to the maximum dose within the profile. The reference profiles must match the TPS, and could be acquired from a vendor published dataset, beam matching dataset or linac commissioning data.

6.3.3 Beam quality

The tissue phantom ratio (TPR_{20,10}) measured in water was 0.701. The PDD_{20,10} ratio was 0.618.

6.3.4 Data for the treatment planning system

6.3.4.A PDDs

For the 10 x 10 cm² beam $d_{\max} = 1.3$ cm. This is shallower than would be typical on a linac with no magnetic field.

The ERE is clearly observed in figure 6.1 and is approximately 10% of the dose at d_{\max} for medium and large beams. The practical range of the ERE is 1.2 ± 0.1 cm back into the phantom or patient. In this case the ERE was measured with a phantom of depth 25 cm. The small-field PDDs were measured with a microDiamond detector. This limited both the depth of the standard PDD, and the ability to measure and join an exit PDD.

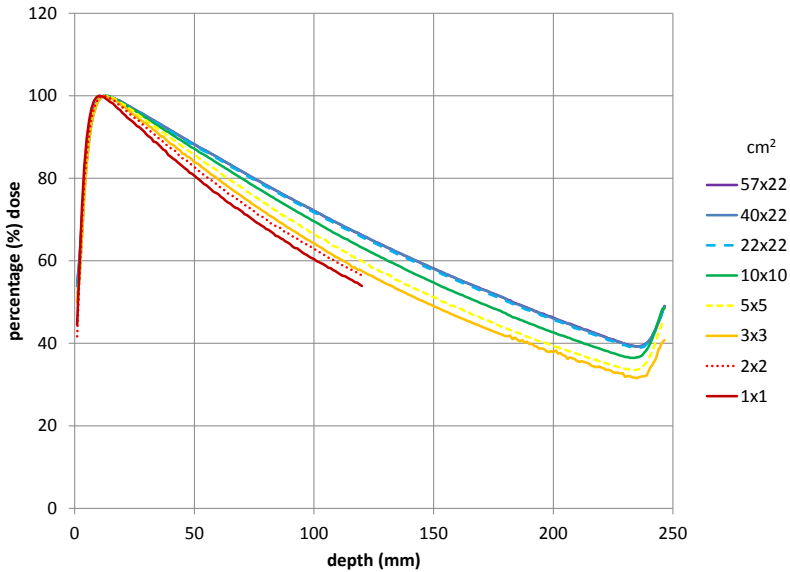


Figure 6.1: Multi-scan combined PDDs showing shallow d_{\max} , and electron return effect at the exit side of the phantom at 25 cm.

Clinical staff should be aware of the increased exit surface dose which should be evaluated in some circumstances - for example breast radiotherapy (van Heijst *et al.*, 2013; Kim *et al.*, 2017). Nevertheless, the magnitude and extent of this exit surface dose change is less than the effect of a treatment couch on the entrance surface dose.

6.3.4.B Profiles

Example inline and crossline profiles are shown in figure 6.2. The asymmetry in the edges of the crossline profiles is evident, with an average shift of $x = +0.24$ cm. The Lorentz force, and thus the crossline shift, must be adequately modeled/calculated within the treatment planning system. Once this is achieved, the shift in profile does not affect the ability of the optimizer to generate the desired treatment plan. For example, mirrored beam angles are not required.

Diagonal profiles for the largest 57×22 cm² beam are shown in figure 6.3. These were used to assess the beam fluence across the largest possible off-axis distance.

MRI-linac penumbra (20 – 80%) widths for each field edge for several standard field sizes are shown in table 6.2 (after artificial flattening). Also shown is a comparison between

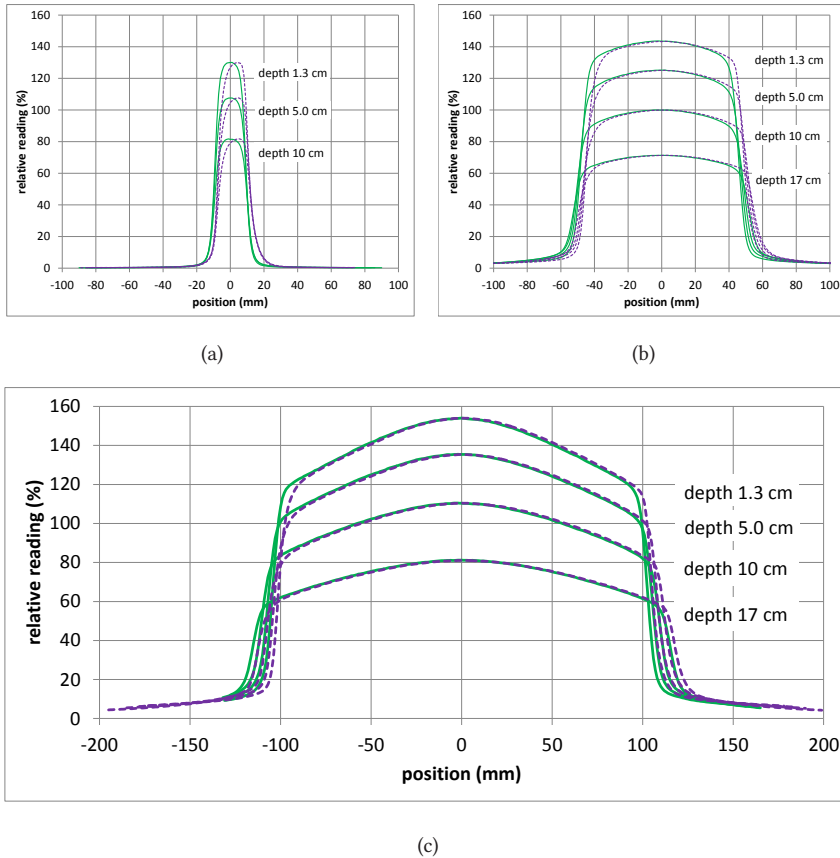


Figure 6.2: Inline (solid green) and crossline (dashed purple) profiles for 2×2 , 10×10 and 22×22 cm^2 beams at depths of 1.3, 5 and 10 cm (and 17 cm for 10×10 and 22×22 cm^2 beams). All profiles scaled relative to 100% at centre of 10×10 cm^2 beam at 10 cm depth.

the MRI-linac and an Agility 6 MV FFF beam, measured with comparable detectors. The MLC penumbral width of both machines (MRI-linac y and Agility x) are similar. The Agility jaw penumbra (y) is sharper. The MRI-linac jaw penumbra (x) is wider due to the Lorentz force on the scattered, charged particles. However, it is still very similar to the MLC penumbra.

6.3.4.C Relative output and scatter factors

The measured MRI-linac relative output factors and collimator (and cryostat) scatter factors are shown in figure 6.5. For comparison, 6 MV flattened and FFF beam values from an Elekta Agility are also shown. The MRI-linac demonstrates similar behavior for small fields. For larger field sizes the scatter increases, and this is also evident in the ROFs which are more similar to the flattened beam than the FFF beam.

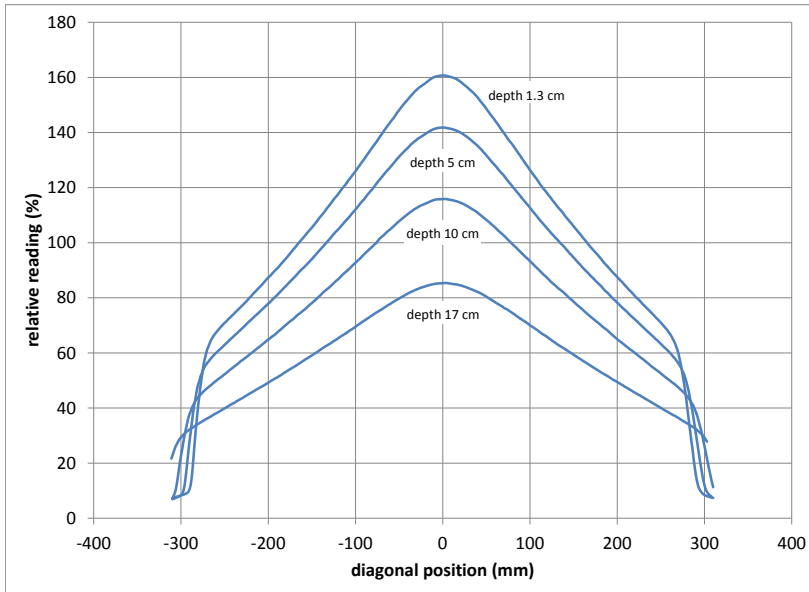


Figure 6.3: Diagonal profiles of largest $57 \times 22 \text{ cm}^2$ beam at 1.3, 5, 10 and 17 cm depth. Readings relative to the $10 \times 10 \text{ cm}^2$ beam reading on CAX at 10 cm depth.

Elekta will provide a data collection template for the MRI-linac. The template and requirements are based on the knowledge gained from this work, and similar data collection processes at Elekta factory and MRI-linac consortium sites.

6.3.5 Cryostat scatter

The change in ionisation reading with distance from the source (SDD) is consistent with the cryostat acting as a secondary scatter source. A best fit to the data, including that shown in figure 6.6a, indicates that for field sizes of 6×6 , 10×10 and $20 \times 20 \text{ cm}^2$ the cryostat contributes respectively 0.3%, 1.0% and 2.0% of the in-field dose at isocentre. This is incorporated within the TPS modelling and is of no clinical consequence.

The collimator and cryostat scatter factors (figure 6.5) are normalised to the $10 \times 10 \text{ cm}^2$ beam, so any scatter difference at this field size is not evident in this factor. However, the CSF for the $20 \times 20 \text{ cm}^2$ beam is increased by 2.0% relative to the $10 \times 10 \text{ cm}^2$ beam.

Figure 6.6b compares MRI-linac and Agility 6 MV (with flattening filter) profiles for 5×5 , 10×10 and $20 \times 20 \text{ cm}^2$ beams at 10 cm depth. An Agility 6 MV FFF profile is also shown for the $20 \times 20 \text{ cm}^2$ beam. At 2 cm beyond the nominal field edge (position

Linac	Detector	Field size (cm ²)	Depth (cm)	Width 20 – 80% (cm)			
				-x	+x	-y	+y
MRI-linac	microDiamond	2 x 2	1.3	0.42	0.47	0.38	0.36
		2 x 2	10	0.43	0.56	0.43	0.40
		5 x 5	1.3	0.44	0.52	0.41	0.38
		5 x 5	10	0.55	0.64	0.50	0.50
	Semiflex 3D	10 x 10	1.3	0.61	0.70	0.62	0.61
		10 x 10	10	0.77	0.87	0.76	0.74
MRI-linac	Semiflex 3D	5 x 5	10	0.69	0.76	0.67	0.67
Agility	CC04	5 x 5	10	0.68	0.70	0.51	0.52

Table 6.2: Penumbra widths for the MRI-linac at depths 1.3 and 10 cm, measured with microDiamond (small fields) and Semiflex 3D. Also shown are comparison values between the MRI-linac and Agility 6 MV FFF for the 5 x 5 cm² field shown in figure 6.4.

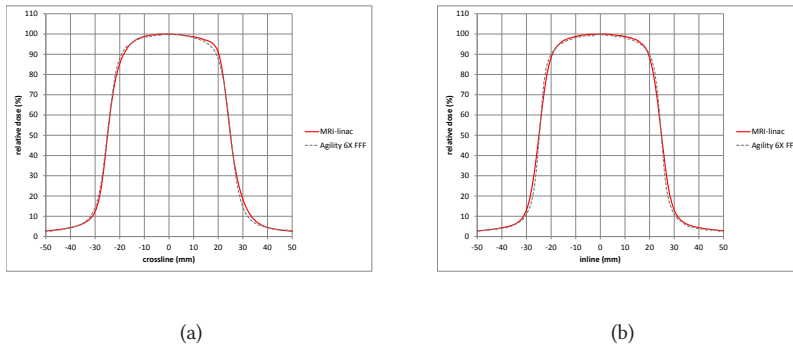


Figure 6.4: Comparison of MRI-linac and Agility 6 MV FFF crossline penumbra (left) and inline penumbra (right) for a 5 x 5 cm² beam at depth 10 cm (without artificial flattening). Crossline penumbra width is similar, with the Agility having a smaller penumbra in the inline direction.

marked with black dots in figure), the MRI-linac average relative readings are smaller than the flattened beam profiles by 0.9%, 1.2% and 0.2% (percentage of central axis dose) respectively. At this position the MRI-linac dose is 3.1% higher than the Agility 6 MV flattening filter free beam. These results are consistent with those reported previously by Duglio *et al.* (2016).

Measurements outside the beam, in the isocentric xy plane, were also made in air with a Farmer chamber in a build up cap. These measured collimator and cryostat scatter and head leakage but excluded phantom scatter. These are compared to the dose profiles measured at d_{\max} along the same divergent paths in table 6.3. It is evident that the scatter accounts for the differences in readings between field sizes.

Both the in-field profile shape, and the scatter outside the beam (figure 6.6b) indicate that the cryostat is equivalent to a partial flattening filter. The in-air measurements

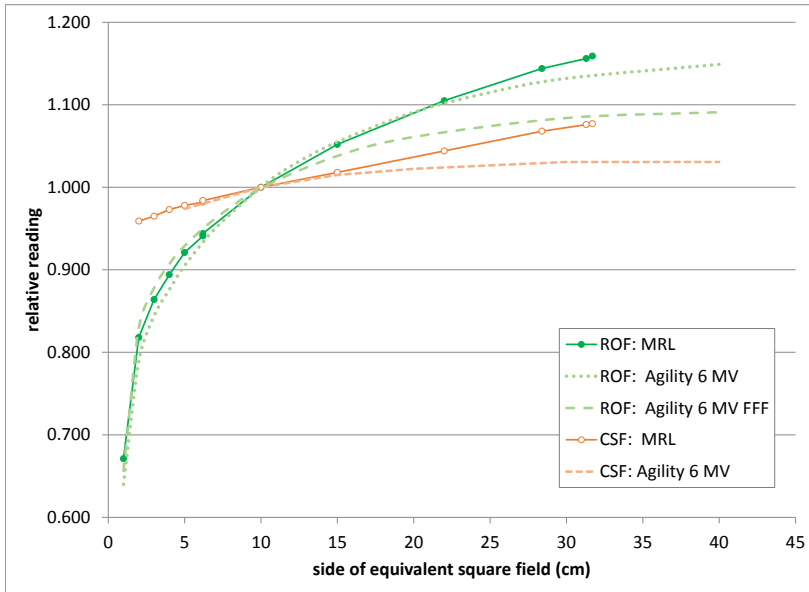


Figure 6.5: Relative output factors (ROFs) and collimator and cryostat scatter factors (CSF) for the MRI-linac in comparison with data from a standard Elekta Agility linac (6 MV flattened and FFF). The cryostat scatter becomes evident for larger fields.

	Field size (cm ²)			
	6 x 6	10 x 10	20 x 20	40 x 22
Distance from CAX (cm)	5	10	15	25
Distance from field edge (cm)	2	5	5	5
Average reading in water	2.0%*	2.2%	4.8%	5.4%
Average reading in air	1.5%	1.6%	3.7%	4.3%

Table 6.3: Out-of-field readings measured in water and in air, expressed as percentage of central axis readings. Photon scatter accounts for the majority of variation between beam sizes. (Note reading in water for 6 x 6 beam was interpolated from 5 x 5 and 10 x 10 cm² beams)

demonstrate that the scatter dose is increasing from 1.5% for small beams up to, for example, 3.7% for a 20 x 20 cm² beam. Photon interactions with the cryostat are modelled within the Monaco TPS so that the photon scatter dose is calculated correctly. It is also noted that for out-of-field dose, the MRI-linac performs as well or better than the Agility 6 MV conventional flattened beam.

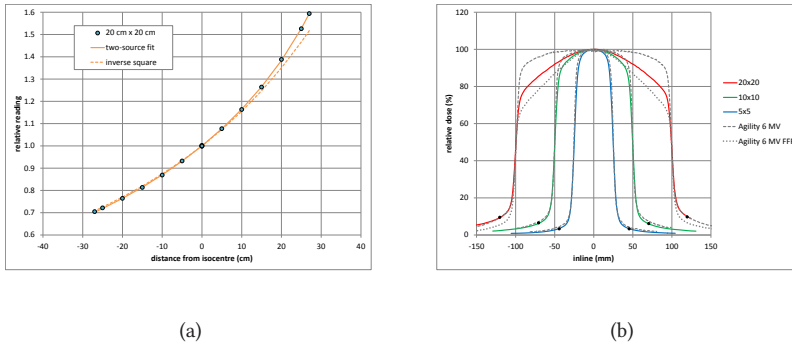


Figure 6.6: Visualisation of cryostat scatter dose. (a) MRI-linac scatter is quantified through a dual-source fit in an ‘effective SSD’ plot, and (b) the out-of-field dose is compared between the MRI-linac and an Agility linac

6.3.6 Leakage

Leakage measurements in the patient plane were all less than 0.1% D_{\max} of a 10 x 10 cm² beam, consistent with standard linacs. Thus the leakage has no significant additional effect on out-of-field dose.

6.3.7 Cryostat transmission

The transmission through the cryostat varies with gantry angle. Figure 6.7 shows the transmission variation measured as a function of gantry angle. MV images were also acquired to check for small attenuating structures, with the only item being the magnet conduit at +13 degrees, which is excluded as a treatment gantry angle (see section 6.2.1). Output variation was also measured separately with an ion chamber and was found to be within normal linac tolerances of $\pm 0.5\%$. Thus the observed variation in figure 6.7 is due to the cryostat. The slight asymmetry is due to the manufacturing tolerances of the cryostat and gradient coil assembly. The cryostat variation is reproducible and has been quantified for inclusion within the TPS.

6.3.8 Surface dose

Field size (cm ²)	2x2	5x5	10x10	20x20
Surface dose	32.3%	34.6%	35.8%	38.0%

Table 6.4: MRI-Linac 7 MV relative surface dose (at 0.0 cm) expressed as a percentage of D_{\max} , for a range of beam sizes.

For the MRI-linac the entrance surface dose for a 10 x 10 cm² beam measured with film was 36%. Values for different beam sizes are shown in table 6.4. The Semiflex 3D-measured PDD (0.2 cm) was 57%. For the Elekta Agility 6 MV flattened beam, the equiv-



Figure 6.7: Change in transmission through the cryostat (change in ion chamber relative reading) as a function of gantry angle. Missing data around gantry 13° is due to avoidance of the superconducting wire. Full range in transmission is 3.5%.

alent value (measured with ion chamber CC04) was 60.7%. Thus at the shallow depth of 0.2 cm the near-surface doses were very similar.

For standard linacs the relative surface dose is within the range 10 - 25% for all clinical $10 \times 10 \text{ cm}^2$ beams (van Dyk, 1999).

In the MRI-linac, contaminant electrons from the linac head and the cryostat are curved away by the magnetic field. However, it is possible that there is some contribution from low energy photons scattered from the cryostat. In addition, the average direction of the secondary particles released from a gantry 0 degree beam is angled, and this is known to increase the surface dose (Khan, 1994). Nevertheless, at 0.2 cm depth the MRI-linac dose is similar to that from an Agility.

6.4 Conclusion

The 1.5 T MRI-linac 7 MV FFF beam has been characterised for the first time and is suitable for clinical use.

Basic properties have been verified including the expected functional capabilities. Coplanar, step-and-shoot IMRT using leaves of width ≈ 0.72 cm, up to a maximum field size of 57.4×22 cm² was achievable, and the system satisfied the relevant beam requirements of IEC60976.

Beam data were acquired for field sizes between 1×1 and 57×22 cm². The described and presented data were sufficient to model the beam in the Monaco treatment planning system. Beam characterisation required new techniques to be developed, including the measurement of PDD curves with electron return effect at beam exit. These exhibited an electron-type practical range of 1.2 ± 0.1 cm. The Lorentz force acting on the secondary charged particles created an asymmetry in the crossline profiles with an average shift of $+0.24$ cm. For a 10×10 cm² beam, scatter from the cryostat contributed 1% of the dose at isocentre. This affected the relative output factors, collimator (and cryostat) scatter factors and beam profiles, both in-field and out-of-field. The average 20 – 80% penumbral width measured for small fields with a microDiamond detector at 10 cm depth was 0.50 cm. MRI-linac penumbral widths were very similar to that of the Elekta Agility linac MLC, as was the near-surface dose $\text{PDD}(0.2 \text{ cm}) = 57\%$. The film-measured entrance skin dose was $\sim 36\%$ of D_{max} . Cryostat transmission was quantified for inclusion within the TPS.

CHAPTER 7

Summary and general discussion

7.1 Summary

Acceptance testing, beam characterisation and dosimetry processes for the 1.5 T MRI-linac were developed and implemented.

In chapter 2 a generic formalism was proposed for reference dosimetry in the presence of a magnetic field. Two factors are used to take into account magnetic field effects: 1) a dose conversion factor to correct for the change in local dose distribution and 2) a correction of the reading of the dosimeter used for the reference dosimetry measurements. The formalism was applied to the Elekta MRI-Linac. The factors were derived; $c_B = 0.9949$ and $k_{B_{\parallel},M,Q} = 0.997 \pm 0.002$ or $k_{B_{\perp},M,Q} = 0.967 \pm 0.002$ (for a PTW 30013 chamber). The formalism was successfully implemented for the MRI-Linac and is applicable for other field strengths and geometries.

In chapter 3 the variation in chamber magnetic field correction factors was measured to determine whether generic chamber type-specific magnetic field correction factors can be applied for each of the PTW30013 and FC65-G type ion chambers when used in different orientations to the magnetic field. The magnetic field correction factors within both chamber-types were found to be very consistent. The variations are comparable with the standard uncertainty ($k = 1$) of 0.24%. The consistency of the results for the PTW30013 and FC65-G chambers implies that it is not necessary to derive a new factor for every new PTW30013 or FC65-G chamber. Values for each chamber-type (with careful attention to beam energy, magnetic field strength and beam-field-chamber orientations) can be applied from the literature.

In chapter 4 the PTW 60019 microDiamond was commissioned for use for small-field dosimetry and beam characterisation on the MRI-linac. Standard techniques of detector testing were adapted where necessary to suit the capabilities of the MRI-linac. Detector warmup, constancy, dose linearity, dose rate linearity, field size dependence and leakage were within tolerance. Variation of up to 9.7% was observed in the angular sensitivity, which is significantly larger than in a 0 T environment. For profile scanning, the maxi-

imum effect is approximately 0.6% which is within tolerance. However for large beams within a magnetic field it would not be suitable for measuring beam symmetry. The effective point of measurement of the detector when used within a 1.5 T magnetic field was determined to be 0.80 ± 0.23 mm below the top surface of the device. The results of this study demonstrate that the PTW 60019 microDiamond detector is suitable for measuring small radiation fields within a 1.5 T magnetic field and thus is suitable for use in MRI-linac commissioning and quality assurance.

In chapter 5 an acceptance procedure for the new Elekta Unity 1.5 T MRI-linac was developed and implemented consistent with stereotactic body radiotherapy use. The procedure includes a list of acceptance tests and specifications (table 5.2) and a schematic of system alignment checks (figure 5.2) which are intended to assist future Unity MRI-linac users. As proof of feasibility, results for the first Unity system were presented. The MRI-linac met safety requirements for patients and operators and specifications for clinical introduction. The system delivers radiation for SBRT effectively.

In chapter 6 the Elekta 1.5 T MRI-linac 7 MV FFF radiation beam was characterised. Machine performance was verified and the system satisfied the relevant beam requirements of IEC60976. Beam data were acquired for field sizes between 1×1 and 57×22 cm². New techniques were developed to measure PDD curves including the electron return effect at beam exit. The 1.5 T MRI-linac 7 MV FFF beam was characterised for the first time and was suitable for clinical use. This was a key step towards the first clinical treatments with the MRI-linac, which were delivered at University Medical Center Utrecht in May 2017 (Raaymakers *et al.*, 2017).

7.2 General discussion

This thesis addressed several key issues for the clinical introduction of the MRI-linac. Additional topics were addressed, and must continue to be addressed in the context of further development of the MRI-linac hardware, software and clinical applications.

7.2.1 Measurement equipment

New physics equipment is highly desirable. Items such as copper plates and rings (or equivalent) to remove the effect of the Lorentz force from measurements (van Zijp *et al.*, 2016) are important for checking beam alignment. A MRI-compatible 2D-array is important for efficient and high quality routine beam QA. A MRI-compatible scanning water phantom (Smit *et al.*, 2014b) enables gold-standard beam characterisation and QA, which cannot be achieved without it.

Additional tests with the PTW MP3 scanning water phantom have demonstrated an interaction between the motor drive position and the reference ion chamber reading. This is probably due to contaminant electrons from the motors streaming along the field lines to the reference detector. Thus, for optimal performance the reference detector

should be located above the height of the motor drives and also away from the edge of the bore.

Phantoms that support both MR imaging and dose measurement are very useful for the MRgRT environment, and necessary for end-to-end testing where the treatment plan is adapted. New phantoms are needed. For end-to-end testing, Elekta use a prototype version of the CIRS MRGRT motion management phantom (model 008Z) (CIRS, Norfolk Virginia, USA) which supports MR imaging and dose measurement with ion chambers. PTW are developing an Octavius patient QA system which supports MR imaging and 3D-volume dosimetry with a 2D ion chamber array.

7.2.2 Dosimetry

A new formalism and set of magnetic field correction factors was discussed in chapters 2 and 3. A key assumption of the van Asselen method is that the photon fluence of the beam remains the same with and without the magnetic field. If MRI-linac measurements of k_B for a specific chamber (or a new type of chamber) are desired, it is recommended that the MRI-linac megavoltage imager (MVI) be used to verify beam constancy throughout the experiment.

While in principle it is good to directly measure $k_{\vec{B},M,Q}$ for a specific ion chamber, the uncertainty in a single experiment is comparable to the uncertainty from using values from the literature, as was established in chapter 3.

The Netherlands Standards Laboratory (VSL) have developed an MRI-compatible primary standards calorimeter which can be used in the Unity MRI-linac (de Prez *et al.*, 2016a, 2019a). This enables a direct measurement of energy deposition, and is thus the gold-standard for determining ion chamber calibration coefficients including magnetic field correction factors. The results from the calorimetry and the van Asselen methods are consistent (de Prez *et al.*, 2019b).

It is worth repeating that reference conditions must now include specification of magnetic field strength and direction, beam gantry angle, and for measurements, the orientation of the ion chamber relative to the beam and magnetic field.

7.2.3 System alignment and beam geometry

The Elekta installation process includes significant testing of system alignment and beam geometry. An independent process is thoroughly described in chapter 5. The independent process did indeed reveal that in one instance the accelerating waveguide was misaligned after on-site replacement, which is a useful reminder of the value of independent checks.

7.2.4 MRI

Magnetic resonance image quality and geometric accuracy are fundamental to the system. Acceptance, commissioning and QA have been well established by a multi-center consortium, including tests of the simultaneous use of MRI and linac. Guidelines have been provided (Tijssen *et al.*, 2019). An indicative example from these guidelines is that the gradient linearity results in geometric accuracy better than 1 mm within a 250 mm central diameter, and better than 2 mm within a 400 mm diameter. Image quality equal to that of Philips 1.5 T diagnostic scanners is achievable in many cases. However, specialised receiver coils for head and neck are not yet available.

General diagnostic protocols are usually not suitable for the MRI-linac. Specific T1, T2 and DWI protocols have been developed by Elekta and Philips for multiple anatomical sites, that ensure image quality and geometric accuracy.

7.2.5 Beam characterisation

Beam characterisation is thoroughly described in chapter 6, including an assessment of the Lorentz force crossline profile offset. Additional tests using gafchromic film with and without copper plates to remove the Lorentz force offset (van Zijp *et al.*, 2016), have demonstrated that the offset is $x = +1.5$ mm, consistent with the results of O'Brien *et al.* (2018), and less than the +2.4 mm reported in chapter 6. The earlier value includes the lateral effective point of measurement (EPoM) offset of the PTW semiflex3D detector, which at ≈ 0.7 mm is larger than was previously expected. The remaining difference is within measurement uncertainty.

7.2.6 TPS

The treatment planning system (TPS) and the Unity 7 MV beam model within the TPS, were commissioned as per existing guidelines (Bruinvis *et al.*, 2005; van der Wal *et al.*, 2013; Ezzell *et al.*, 2003). The MRI-linac makes frequent use of small off-axis beams (because the target is rarely at isocentre) therefore additional attention was given to these. Specific magnetic-field related effects such as ERE at the patient surface and within tissue inhomogeneities were also investigated.

A 1.5-T B field does not affect (i) the ability to optimise plans or (ii) final plan quality, which is comparable to existing clinical plans, even in the presence of air cavities (Bol *et al.*, 2015) or during tracking (Menten *et al.*, 2016).

TPS commissioning culminated in plan-specific QA of clinical IMRT plans. Measurements were performed at UMCU with gafchromic EBT3 film (Ashland, Covington Kentucky, USA) or a Delta4-MR (Scandidos, Uppsala Sweden). Plans for 90 patients have now been tested and passed with good results. Initially the pre-plan and the first fraction of treatment were individually measured. This continues for new treatments (new TPS templates or new anatomical sites). Established sites are tested with a sample of

plans each month as per standard UMCU practice in our conventional radiation therapy clinic.

7.2.7 Connectivity and shared coordinate systems

The Unity system comprises numerous subsystems. All systems complied with the IAEA 61217 coordinate system and could share data in a consistent manner. Plans were developed and checked through the entire treatment chain (CT, contouring, TPS, planning, export, plan documentation, R&V system, treatment delivery, motion monitoring, plan backup and restoration). In each step, the data was correctly transferred, and maintained correct coordinates and orientations.

7.2.8 Clinical workflow and end-to-end tests

A variety of plan adaptation options were tested (Winkel *et al.*, 2019) and commissioned. At UMCU the full fluence re-optimisation, which incorporates all available information, is used to achieve the optimal treatment plan for the patient at the time of treatment.

Each fraction includes online QA of the adapted plan. At UMCU, a collapsed cone dose calculation method (Oncentra, Elekta AB) is used for an independent 3D dose calculation as a sanity check. A custom-software parameter check including number of segments, number of MU, beam irregularity and beam modulation (Du *et al.*, 2014) is also performed. The system is fully automated. It now operates as a traffic light system to be used by the clinical team without requiring a physicist to be present.

A pilot study was performed with a pre-commercial-release MRI-linac system to demonstrate technical feasibility and accuracy of the MRI guidance system within a clinical setting. The observed average difference between the treatment position determined from portal images of the radiation beams, and that determined from the MR images, was 0.3 mm (Raaymakers *et al.*, 2017).

An end-to-end test was performed using the Unity MRI-linac system at UMCU with transverse Gafchromic EBT3 film inside an Alderson phantom. The Alderson phantom is suitable for MR imaging and dose measurement (see chapter 5). The test included full plan reoptimisation for the current phantom position. Positional accuracy was established with markers inside the phantom that were visible on the film. The excellent agreement of calculated and measured dose and position confirmed that the entire MRI-linac is able to be used to accurately deliver high-dose stereotactic MR-guided adaptive radiotherapy.

7.2.9 The future

The Elekta Unity 1.5 T MRI-linac is expected to undergo significant technical upgrades in the coming years. A high priority is automatic gating, where the system can detect if the identified target moves beyond the treatment portal/region and can automatically pause the beam, and wait for the target to return, or perform an adjustment to correct

for a slow positional drift. Continuous rotation VMAT arcs will be a feature of a future release. And longitudinal table motion during treatment would facilitate MR-guided tomotherapy and allow almost any size of target to be treated.

The ultimate goal is intra-treatment (quasi-real time) plan optimisation, which has already been described in detail (Kontaxis *et al.*, 2017).

Acceptance, commissioning and QA must develop to include these new technical capabilities. Online QA is increasingly important because freshly adapted plans cannot be directly measured prior to clinical delivery. Short term solutions for the current MRI-linac as well as long term solutions for future MRI-linac capabilities including quasi real-time plan adaptation, are required. Solutions for time-resolved plan QA to support validation/verification of dose accumulation while the target and organs at risk are deforming, will be an active area of research and development in the coming years.

7.3 Conclusion

The capabilities of the MRgRT systems will lead to widespread, international uptake. The drive towards more frequent adaptive treatments will require new quality-assurance solutions that are as efficient and accurate as possible.

Higher precision imaging and target and organ-at-risk identification support hypofractionation and dose escalation. These are expected to reduce toxicity, be more comfortable for the patient, and lead to improved rates of local control and cancer-specific survival as well as better patient quality of life. As of November 2019, MRgRT is already in clinical use in at least 10 countries throughout the world.

CHAPTER 8

Samenvatting

8.1 Samenvatting

Dit proefschrift beschrijft de acceptatie testen, bundel verificatie en dosimetrie procedures voor de klinische implementatie van de 1.5 T MRI-versneller.

In hoofdstuk 2 is een generiek formalisme beschreven voor referentie dosimetrie in een magnetisch veld. Er zijn twee factoren waarmee rekening gehouden moet worden bij magnetische velden: 1) een dosis conversie factor, om te corrigeren voor de *werkelijke verandering* in de lokale dosis verdeling (ongeveer 0.5%) en 2) een correctie op de *uitlezing* van de gebruikte dosimeter in de referentie dosimetrie metingen, de zogenoemde kamer-specifieke magnetische veldcorrectiefactor (variërend van 0.3 tot 3.5% afhankelijk van de oriëntatie van de dosimeter ten opzichte van de bestralingsbundel en magneetveld). Het formalisme is succesvol geïmplementeerd voor de Elekta Unity MRI-versneller op het UMC Utrecht maar is ook bruikbaar voor andere veldsterktes en geometrieën.

Hoofdstuk 3 beschrijft de metingen van de variatie in de magnetische veldcorrectiefactoren voor twee veelgebruikte dosimeters om te bepalen of generieke factoren kunnen worden toegepast. De onderzochte ionisatie kamers van het type PTW30013 en FC65-G bleken binnen een serie van hetzelfde type zeer constante correctiefactoren te hebben, voor welke oriëntatie ten opzichte van het magnetisch veld ze ook werden gebruikt. De variaties zijn vergelijkbaar met de standaard onzekerheid ($k=1$) van 0.24%. De stabiliteit van de resultaten impliceert dat het niet nodig is om voor iedere nieuwe PTW30013 en FC65-G-kamer een nieuwe factor te meten en berekenen. Per kamer-type (specifiek voor de bundelenergie, de magnetische veldsterkte en de bundelveld-kamer oriëntatie) kunnen literatuur waarden worden gebruikt.

In hoofdstuk 4 zijn de acceptatie metingen en testen beschreven voor de PTW60019 microDiamond detector die gebruikt wordt bij het meten van kleine bestralingsvelden tijdens het karakteriseren van de MRI-linac bundel. Afhankelijk van de mogelijkheden van de MRI-linac zijn, waar nodig, de standaard methoden voor het controleren van detectoren aangepast.

Aspecten als het opwarmen van de detector, bestendigheid, rechtlijnigheid van de dosis, rechtlijnigheid van de dosissnelheid, veldafhankelijkheid en lekstroom waren binnen

tolerantie waarden. Een variatie tot 9,7% werd waargenomen in de hoekgevoeligheid, wat aanzienlijk groter dan in een situatie zonder magneetveld. Voor het scannen van grote bundels in een magnetisch veld is de microDiamond daarom niet geschikt. Echter, het maximale effect voor een profiel scan van een bundel met veldgrootte minder dan 40 cm is ongeveer 0.6%, binnen de tolerantie waarden.

Het effectieve meetpunt van de detector, in een 1.5 T magnetisch veld, was 0.80 ± 0.23 mm onder het oppervlak. Deze studie toont aan dat de PTW60019 microDiamond detector bruikbaar is voor het meten van kleine bestralingsvelden in een 1.5 T magnetisch veld en daarmee bruikbaar bij de commissioning en periodieke kwaliteitsborging van de MRI-linac.

Hoofdstuk 5 beschrijft een nieuw ontwikkelde en geïmplementeerde acceptatie procedure voor de nieuwe Elekta Unity 1.5 T MRI-linac. Hierbij was het doel om dit apparaat te kunnen gebruiken voor stereotactische radiotherapie behandelingen. De procedure bevat een lijst van acceptatie testen, specificaties (tabel 5.2) en een schematische opstelling voor de systeem uitlijning (figuur 5.2). Deze lijst is bedoeld ter ondersteuning van toekomstige MRI-linac gebruikers.

Om de effectiviteit te tonen zijn de resultaten van het eerste Unity systeem gepresenteerd. De MRI-linac voldeed aan de veiligheidseisen voor patiënten, gebruikers ('operators') en aan de specificaties voor de klinische introductie. Daarmee is de Unity geschikt voor SBRT-bestralingen.

Tenslotte wordt in hoofdstuk 6 de karakteristieken van de bestralingsbundel van de Elekta 1.5 T MRI-linac beschreven. Hiervoor zijn meerdere orthogonale profielen van de bestralingsbundel gemeten van veldgrootte van 1×1 tot 57×22 cm². Ook zijn verschillende prestatie-indicatoren van het toestel geverifieerd en voldoet het systeem aan de relevante eisen van de internationale bestralingstoestelnorm (IEC60976). Nieuwe technieken voor het meten van diepte dosis (PDD) curven zijn ontwikkeld inclusief de magneetveld geïnduceerde effecten aan de uittree zijde van de bundel (electron return effect). De studie beschrijft de eerste keer dat de 1.5 T MRI-linac 7 MV FFF bundel is geverifieerd en bruikbaar is bevonden voor klinisch gebruik. Dit was een grote stap naar de eerste klinische behandeling met de 1.5 T MRI-linac welke heeft plaatsgevonden in het Universitair Medisch Centrum Utrecht in mei 2017 (Raaymakers *et al.*, 2017).

Bibliography

- Aalbers A.H.L., Hoornaert M.T., Minken A., Palmans H., Pieksma M.W.H., de Prez L.A., Reynaert N., Vynckier S. and Wittkämper F.W. 2008 Code of practice for the absorbed dose determination in high energy photon and electron beams Tech. Rep. NCS 18 Nederlandse Commissie voor Stralingsdosimetrie Delft, The Netherlands
- Ahmad S.B., Sarfehnia A., Paudel M.R., Kim A., Hissoiny S., Sahgal A. and Keller B. 2016 Evaluation of a commercial MRI linac based Monte Carlo dose calculation algorithm with geant 4 *Medical Physics* 43 894–907
- Alfonso R., Andreo P., Capote R., Huq M.S., Kilby W., Kjäll P., Mackie T.R., Palmans H., Rosser K., Seuntjens J., Ullrich W. and Vatnitsky S. 2008 A new formalism for reference dosimetry of small and nonstandard fields *Medical Physics* 35 5179–5186
- Almaviva S., Ciancaglioni I., Consorti R., Notaristefani F.D., Manfredotti C., Marinelli M., Milani E., Petrucci A., Prestopino G., Verona C. and Verona-Rinati G. 2010 Synthetic single crystal diamond dosimeters for conformal radiation therapy application *Diamond and Related Materials* 19 217 – 220 {NDNC} 2009
- Almaviva S., Marinelli M., Milani E., Tucciarone A., Verona-Rinati G., Consorti R., Petrucci A., Notaristefani F.D. and Ciancaglioni I. 2008 Synthetic single crystal diamond diodes for radiotherapy dosimetry *Nuclear Instruments and Methods in Physics Research Section A: Accelerators, Spectrometers, Detectors and Associated Equipment* 594 273 – 277
- Almond P., Biggs P., Coursey B., Hanson W., Huq M.S., Nath R. and Rogers D. 1999 AAPM's TG51 protocol for clinical reference dosimetry of high-energy photon and electron beams *Med. Phys.* 26 1847 – 1870
- Andreo P., Burns D.T., Hohlfeld K., Huq M.S., Kanai T., Laitano F., Smyth V. and Vynckier S. 2000 Absorbed dose determination in external beam radiotherapy: An international code of practice for dosimetry based on standards of absorbed dose to water Tech. Rep. TRS-398 International Atomic Energy Agency Wagramer Strasse 5 P.O. Box 100, A-1400 Vienna Austria
- Betzel G., Lansley S., Baluti F., Reinisch L. and Meyer J. 2010 Operating parameters of CVD diamond detectors for radiation dosimetry *Nuclear Instruments and Methods in Physics Research Section A: Accelerators, Spectrometers, Detectors and Associated Equipment* 614 130 – 136
- Bol G.H., Lagendijk J.J.W. and Raaymakers B.W. 2015 Compensating for the impact of non-stationary spherical air cavities on IMRT dose delivery in transverse magnetic fields *Physics in Medicine and Biology* 60 755
- Brualla-González L., Gómez F., Pombar M. and Pardo-Montero J. 2016 Dose rate dependence of the PTW 60019 microdiamond detector in high dose-per-pulse pulsed beams *Physics in Medicine and Biology* 61 N11

- Bruinvis I.A.D., Keus R.B., Lenglet W.J.M., Meijer G.J., Mijnheer B.J., van 't Veld A.A., Venselaar J.L.M., Welleweerd J. and Woudstra E. 2005 Quality assurance of 3-D treatment planning systems for external photon and electron beams Tech. Rep. NCS 15 Nederlandse Commissie voor Stralingsdosimetrie Delft, The Netherlands
- Budgell G., Brown K., Cashmore J., Duane S., Frame J., Hardy M., Paynter D. and Thomas R. 2016 IPEM topical report 1: guidance on implementing flattening filter free (FFF) radiotherapy *Physics in Medicine and Biology* 61 8360
- Ciancaglioni I., Marinelli M., Milani E., Prestopino G., Verona C., Verona-Rinati G., Consorti R., Petrucci A. and De Notaristefani F. 2012 Dosimetric characterization of a synthetic single crystal diamond detector in clinical radiation therapy small photon beams *Medical Physics* 39 4493–4501
- Das I.J., Cheng C.W., Watts R.J., Ahnesjö A., Gibbons J., Li X.A., Lowenstein J., Mitra R.K., Simon W.E. and Zhu T.C. 2008 Accelerator beam data commissioning equipment and procedures: Report of the TG-106 of the therapy physics committee of the AAPM *Medical Physics* 35 4186
- De Angelis C., Onori S., Pacilio M., Cirrone G.A.P., Cuttone G., Raffaele L., Bucciolini M. and Mazzocchi S. 2002 An investigation of the operating characteristics of two PTW diamond detectors in photon and electron beams *Medical Physics* 29 248–254
- De Coste V., Francescon P., Marinelli M., Masi L., Paganini L., Pimpinella M., Prestopino G., Russo S., Stravato A., Verona C. and Verona-Rinati G. 2017 Is the PTW 60019 micro-diamond a suitable candidate for small field reference dosimetry? *Physics in Medicine and Biology* 62 7036
- de Prez L., de Pooter J., Jansen B. and Aalbers T. 2016a A water calorimeter for on-site absorbed dose to water calibrations in ^{60}Co and MV-photon beams including MRI incorporated treatment equipment *Physics in Medicine and Biology* 61 5051–5076
- de Prez L., de Pooter J., Jansen B., Perik T. and Wittkämper F. 2018 Comparison of k_Q factors measured with a water calorimeter in flattening filter free (FFF) and conventional flattening filter (cFF) photon beams *Physics in Medicine and Biology* 63 045023
- de Prez L., de Pooter J., Jansen B., Wolthaus J., van Asselen B., Woodings S., Soest T., Kok J. and Raaymakers B. 2016b First water calorimetric D_w measurement and direct measurement of magnetic field correction factors, $k_{Q,B}$, in a 1.5 T B-field of an MRI linac *AAPM 2016 Annual conference TH-CD-BRA-05*
- de Prez L., de Pooter J., Jansen B., Woodings S., Wolthaus J., van Asselen B., van Soest T., Kok J. and Raaymakers B. 2019a Commissioning of a water calorimeter as a primary standard for absorbed dose to water in magnetic fields *Physics in Medicine and Biology* 64 035013
- de Prez L., Woodings S., de Pooter J., van Asselen B., Wolthaus J., Jansen B. and Raaymakers B. 2019b Direct measurement of ion chamber correction factors, k_Q and k_B , in a 7 MV MRI-linac *Physics in Medicine & Biology* 64 105025
- de Vries J.H.W., Seravalli E., Houweling A.C., Woodings S.J., van Rooij R., Wolthaus J.W.H., Lagendijk J.J.W. and Raaymakers B.W. 2018 Characterization of a prototype MR-compatible Delta4 QA system in a 1.5 tesla MR-linac *Physics in Medicine and Biology* 63 02NT02

- Du W., Cho S.H., Zhang X., Hoffman K.E. and Kudchadker R.J. 2014 Quantification of beam complexity in intensity-modulated radiation therapy treatment plans *Medical Physics* 41 021716
- Duglio M., Towe S. and Roberts D. 2016 Beam and cryostat scatter characteristics of the Elekta MR-linac *AAPM 2016 Annual conference SU-F-J-149*
- Ezzell G.A., Galvin J.M., Low D., Palta J.R., Rosen I., Sharpe M.B., Xia P., Xiao Y. and Yu C.X. 2003 Guidance document on delivery, treatment planning, and clinical implementation of IMRT: Report of the IMRT subcommittee of the AAPM radiation therapy committee *Medical Physics* 30 2089
- Fallone B.G. 2014 The rotating biplanar linac–magnetic resonance imaging system *Seminars in Radiation Oncology* 24 200 – 202 Magnetic Resonance Imaging in Radiation Oncology
- Fogliata A., Garcia R., Knöös T., Nicolini G., Clivio A., Vanetti E., Khamphan C. and Cozzi L. 2012 Definition of parameters for quality assurance of flattening filter free (FFF) photon beams in radiation therapy *Medical Physics* 39 6455–6464
- Ghila A., Fallone B.G. and Rathee S. 2016 Influence of standard RF coil materials on surface and buildup dose from a 6 MV photon beam in magnetic field *Medical Physics* 43 5808–5816
- Hackett S., Asselen B.V., Wolthaus J., Kok J., Woodings S., Lagendijk J. and Raaymakers B. 2016 OC-0075: Impact of air around an ion chamber: solid water phantoms not suitable for dosimetry on an MR-linac *Radiotherapy and Oncology* 119 S34 – S35 ESTRO 35, 29 April - 3 May 2016, Turin, Italy
- Hissoiny S., Ozell B., Bouchard H. and Després P. 2011a GPUMCD: A new GPU-oriented Monte Carlo dose calculation platform *Medical Physics* 38 754–764
- Hissoiny S., Raaijmakers A.J.E., Ozell B., Després P. and Raaymakers B.W. 2011b Fast dose calculation in magnetic fields with GPUMCD *Physics in Medicine and Biology* 56 5119–5129
- Houweling A.C., de Vries J.H.W., Wolthaus J., Woodings S., Kok J.G.M., van Asselen B., Smit K., Bel A., Lagendijk J.J.W. and Raaymakers B.W. 2016 Performance of a cylindrical diode array for use in a 1.5 T MR-linac *Physics in Medicine and Biology* 61 N80
- International Atomic Energy Agency 2006 Radiation protection in the design of radiotherapy facilities Tech. Rep. SRS 47 International Atomic Energy Agency Wagramer Strasse 5 P.O. Box 100, 1400 Vienna Austria
- International Commission on Radiation Units & Measurements 1999 Prescribing, recording and reporting photon beam therapy (supplement to ICRU report 50) Tech. Rep. ICRU 62 International Commission on Radiation Units and Measurements Bethesda Maryland USA
- International Commission on Radiation Units & Measurements 2010 Prescribing, recording and reporting photon beam intensity modulated radiation therapy Tech. Rep. ICRU 83 International Commission on Radiation Units and Measurements Bethesda Maryland USA
- International Electrotechnical Commission 2007 IEC 60976 medical electrical equipment

- medical electron accelerators - functional performance characteristics Tech. Rep. IEC 60976 International Electrotechnical Commission Geneva, Switzerland
- International Electrotechnical Commission 2009 IEC 60601-2-1 medical electrical equipment - part 2-1: Particular requirements for the basic safety and essential performance of electron accelerators in the range 1 mev to 50 mev Tech. Rep. IEC 60601 International Electrotechnical Commission Geneva, Switzerland
- International Electrotechnical Commission 2011 IEC 61217 radiotherapy equipment - coordinates movements and scales Tech. Rep. IEC 61217 International Electrotechnical Commission Geneva, Switzerland
- Jaffray D.A., Siewerdsen J.H., Wong J.W. and Martinez A.A. 2002 Flat-panel cone-beam computed tomography for image-guided radiation therapy *International Journal of Radiation Oncology*Biophysics* 53 1337 – 1349
- Keall P.J., Barton M. and Crozier S. 2014 The Australian magnetic resonance imaging–linac program *Seminars in Radiation Oncology* 24 203 – 206 Magnetic Resonance Imaging in Radiation Oncology
- Keyvanloo A., Burke B., Warkentin B., Tadic T., Rathee S., Kirkby C., Santos D.M. and Fallone B.G. 2012 Skin dose in longitudinal and transverse linac-MRIs using Monte Carlo and realistic 3D MRI field models *Medical Physics* 39 6509–6521
- Khan F.M. 1994 *The Physics of Radiation Therapy, 2nd ed.* (Baltimore, Maryland, USA: Lippincott Williams and Wilkins)
- Kim A., Lim-Reinders S., McCann C., Ahmad S.B., Sahgal A., Lee J. and Keller B.M. 2017 Magnetic field dose effects on different radiation beam geometries for hypofractionated partial breast irradiation *Journal of Applied Clinical Medical Physics* 18 62–70
- Kirby M., Ryde S., Hall C., of Physics I, in Medicine (Great Britain) E. and Beavis A. 2006 *Acceptance Testing and Commissioning of Linear Accelerators* IPEM report (94) (Institute of Physics and Engineering in Medicine)
- Klein E., Hanley J., Bayouth J., Yin F., Simon W., Dresser S., Serago C., Aguirre F., Ma L., Arjomandy B., Liu C., Sandin C. and Holmes T. 2009 Task group 142 report: Quality assurance of medical accelerators *Med. Phys.* 36 4197 – 4212
- Kontaxis C., Bol G.H., Stemkens B., Glitzner M., Prins F.M., Kerkmeijer L.G.W., Lagendijk J.J.W. and Raaymakers B.W. 2017 Towards fast online intrafraction replanning for free-breathing stereotactic body radiation therapy with the MR-linac *Physics in Medicine and Biology* 62 7233–7248
- Kutcher G., Coia L., Gillin M., Hanson W., Leibel S., Morton R., Palta J., Purdy J., Reinstein L., Svensson G., Weller M. and Wingfield L. 1994 Comprehensive QA for radiation oncology: Report of task group no. 40 radiation therapy committee AAPM *Med. Phys.* 21 581 – 618
- Lagendijk J.J., Raaymakers B.W., Raaijmakers A.J., Overweg J., Brown K.J., Kerkhof E.M., van der Put R.W., Haardemark B., van Vulpen M. and van der Heide U.A. 2008 MRI/linac integration *Radiotherapy and Oncology* 86 25 – 29
- Lagendijk J.J., Raaymakers B.W. and van Vulpen M. 2014 The magnetic resonance imaging–linac system *Seminars in Radiation Oncology* 24 207 – 209 Magnetic Resonance

Imaging in Radiation Oncology

- Lagendijk J.J.W., Raaymakers B.W., van der Heide U.A., Topolnjak R., Dehnad H., Hofman P., Nederveen A.J., Schulz I.M., Welleweerd J. and Bakker C.J.G. 2002 MRI guided radiotherapy: MRI as position verification system for IMRT *Radiotherapy and Oncology* 64 (Suppl 1)
- Lárraga-Gutiérrez J.M., Ballesteros-Zebadúa P., Rodríguez-Ponce M., no O.A.G.G. and de la Cruz O.O.G. 2015 Properties of a commercial PTW-60019 synthetic diamond detector for the dosimetry of small radiotherapy beams *Physics in Medicine and Biology* 60 905
- Laub W.U. and Crilly R. 2014 Clinical radiation therapy measurements with a new commercial synthetic single crystal diamond detector *Journal of Applied Clinical Medical Physics* 15 92–102
- Looe H.K., Harder D. and Poppe B. 2011 Experimental determination of the effective point of measurement for various detectors used in photon and electron beam dosimetry *Physics in Medicine and Biology* 56 4267
- Malkov V.N., Hackett S.L., Wolthaus J.W.H., Raaymakers B.W. and van Asselen B. 2019 Monte Carlo simulations of out-of-field surface doses due to the electron streaming effect in orthogonal magnetic fields *Physics in Medicine and Biology* 64 115029
- Malkov V.N. and Rogers D.W.O. 2017 Sensitive volume effects on Monte Carlo calculated ion chamber response in magnetic fields *Medical Physics* 44 4854–4858
- Malkov V.N. and Rogers D.W.O. 2018 Monte Carlo study of ionization chamber magnetic field correction factors as a function of angle and beam quality *Medical Physics* 45 908–925
- Mayles R., McKenzie A., Macaulay E., Morgan H., Jordan T. and Powley S. 1999 *Physical Aspects of Quality Control in Radiotherapy* (York, England: Institute of Physics and Engineering in Medicine)
- McEwen M., DeWerd L., Ibbott G., Followill D., Rogers D.W.O., Seltzer S. and Seuntjens J. 2014 Addendum to the AAPM's TG-51 protocol for clinical reference dosimetry of high-energy photon beams *Medical Physics* 41 041501
- McEwen M.R. 2010 Measurement of ionization chamber absorbed dose factors in megavoltage photon beams *Medical Physics* 37 2179–2193
- Meijer G.J., van Kleffens H.J. and Mijnheer B.J. 1996 Quality control of medical linear accelerators; current practice and minimum requirements. Tech. Rep. NCS 9 Nederlandse Commissie voor Stralingsdosimetrie Delft, The Netherlands
- Meijsing I., Raaymakers B.W., Raaijmakers A.J.E., Kok J.G.M., Hogeweg L., Liu B. and Lagendijk J.J.W. 2009 Dosimetry for the MRI accelerator: the impact of a magnetic field on the response of a Farmer NE2571 ionization chamber *Physics in Medicine and Biology* 54 2993
- Menten M.J., Fast M.F., Nill S., Kamerling C.P., McDonald F. and Oelfke U. 2016 Lung stereotactic body radiotherapy with an MR-linac – quantifying the impact of the magnetic field and real-time tumor tracking *Radiotherapy and Oncology* 119 461 – 466
- Mutic S. and Dempsey J.F. 2014 The ViewRay system: Magnetic resonance-guided and

- controlled radiotherapy *Seminars in Radiation Oncology* 24 196–199
- Oborn B.M., Metcalfe P.E., Butson M.J. and Rosenfeld A.B. 2009 High resolution entry and exit Monte Carlo dose calculations from a linear accelerator 6 MV beam under the influence of transverse magnetic fields *Medical Physics* 36 3549–3559
- Oborn B.M., Metcalfe P.E., Butson M.J. and Rosenfeld A.B. 2010 Monte Carlo characterization of skin doses in 6 MV transverse field MRI-linac systems: Effect of field size, surface orientation, magnetic field strength, and exit bolus *Medical Physics* 37 5208–5217
- O’Brien D.J., Dolan J., Pencea S., Schupp N. and Sawakuchi G.O. 2018 Relative dosimetry with an MR-linac: Response of ion chambers, diamond, and diode detectors for off-axis, depth dose, and output factor measurements *Medical Physics* 45 884–897
- O’Brien D.J., Roberts D.A., Ibbott G.S. and Sawakuchi G.O. 2016 Reference dosimetry in magnetic fields: formalism and ionization chamber correction factors *Medical Physics* 43 4915–4927
- O’Brien D.J. and Sawakuchi G.O. 2017 Monte Carlo study of the chamber-phantom air gap effect in a magnetic field *Medical Physics* 44 3830–3838
- Park J.M., Shin K.H., Kim J.i., Park S.Y., Jeon S.H., Choi N., Kim J.H. and Wu H.G. 2018 Air–electron stream interactions during magnetic resonance IGRT *Strahlentherapie und Onkologie* 194 50–59
- PTW 2014 User manual. microDiamond type 60019 Tech. Rep. D930.131.00/02 en PTW PTW-Freiburg Dr. Pychlau GmbH Lorracher Str. 7 FREIBURG 79115 Germany
- PTW 2015 User manual. Roos type 34001 Tech. Rep. D329.131.00/04 en PTW PTW-Freiburg Dr. Pychlau GmbH Lorracher Str. 7 FREIBURG 79115 Germany
- Raaijmakers A.J.E., Raaymakers B.W. and Lagendijk J.J.W. 2005 Integrating a MRI scanner with a 6 MV radiotherapy accelerator: dose increase at tissue–air interfaces in a lateral magnetic field due to returning electrons *Physics in Medicine and Biology* 50 1363
- Raaijmakers A.J.E., Raaymakers B.W. and Lagendijk J.J.W. 2008 Magnetic-field-induced dose effects in MR-guided radiotherapy systems: dependence on the magnetic field strength *Physics in Medicine and Biology* 53 909–923
- Raaijmakers A.J.E., Raaymakers B.W., van der Meer S. and Lagendijk J.J.W. 2007 Integrating a MRI scanner with a 6 MV radiotherapy accelerator: impact of the surface orientation on the entrance and exit dose due to the transverse magnetic field *Physics in Medicine and Biology* 52 929
- Raaymakers B.W., de Boer J.C.J., Knox C., Crijns S.P.M., Smit K., Stam M.K., van den Bosch M.R., Kok J.G.M. and Lagendijk J.J.W. 2011 Integrated megavoltage portal imaging with a 1.5 T MRI linac *Physics in Medicine and Biology* 56 N207
- Raaymakers B.W., Jürgenliemk-Schulz I.M., Bol G.H., Glitzner M., Kotte A.N.T.J., van Asselen B., de Boer J.C.J., Bluemink J.J., Hackett S.L., Moerland M.A., Woodings S.J., Wolthaus J.W.H., van Zijp H.M., Philippens M.E.P., Tijssen R., Kok J.G.M., de Groot-van Breugel E.N., Kiekebosch I., Meijers L.T.C., Nomden C.N., Sikkes G.G., Doornaert P.A.H., Eppinga W.S.C., Kasperts N., Kerkmeijer L.G.W., Tersteeg J.H.A., Brown K.J.,

- Pais B., Woodhead P. and Lagendijk J.J.W. 2017 First patients treated with a 1.5 T MRI-linac: clinical proof of concept of a high-precision, high-field MRI guided radiotherapy treatment. *Physics in Medicine and Biology* 62 L41–L50
- Raaymakers B.W., Lagendijk J.J.W., Overweg J., Kok J.G.M., Raaijmakers A.J.E., Kerkhof E.M., van der Put R.W., Meijnsing I., Crijs S.P.M., Benedosso F., van Vulpen M., de Graaff C.H.W., Allen J. and Brown K.J. 2009 Integrating a 1.5 T MRI scanner with a 6 MV accelerator: proof of concept *Physics in Medicine and Biology* 54 N229
- Raaymakers B.W., Raaijmakers A.J.E., Kotte A.N.T.J., Jette D. and Lagendijk J.J.W. 2004 Integrating a MRI scanner with a 6 MV radiotherapy accelerator: dose deposition in a transverse magnetic field *Physics in Medicine and Biology* 49 4109
- Ralston A., Tyler M., Liu P., McKenzie D. and Suchowerska N. 2014 Over-response of synthetic microDiamond detectors in small radiation fields *Physics in Medicine and Biology* 59 5873
- Reggiori G., Stravato A., Pimpinella M., Lobefalo F., Coste V.D., Fogliata A., Mancosu P., Rose F.D., Palumbo V., Scorsetti M. and Tomatis S. 2017 Use of PTW-microDiamond for relative dosimetry of unflattened photon beams *Physica Medica* 38 45 – 53
- Reynolds M., Fallone B.G. and Rathee S. 2013 Dose response of selected ion chambers in applied homogeneous transverse and longitudinal magnetic fields *Medical Physics* 40 042102–n/a 042102
- Reynolds M., Fallone B.G. and Rathee S. 2014 Dose response of selected solid state detectors in applied homogeneous transverse and longitudinal magnetic fields *Medical Physics* 41 092103–n/a 092103
- Sastre-Padro M., van der Heide U. and Welleweerd H. 2004 An accurate calibration method of the multileaf collimator valid for conformal and intensity modulated radiation treatments. *Physics in Medicine and Biology* 49 2631
- Smit K., Kok J.G.M., Lagendijk J.J.W. and Raaymakers B.W. 2014 Performance of a multi-axis ionization chamber array in a 1.5 T magnetic field *Physics in Medicine and Biology* 59 1845
- Smit K., Sjöholm J., Kok J.G.M., Lagendijk J.J.W. and Raaymakers B.W. 2014b Relative dosimetry in a 1.5 T magnetic field: an MR-linac compatible prototype scanning water phantom *Physics in Medicine and Biology* 59 4099
- Smit K., van Asselen B., Kok J.G.M., Aalbers A.H.L., Lagendijk J.J.W. and Raaymakers B.W. 2013 Towards reference dosimetry for the MR-linac: magnetic field correction of the ionization chamber reading *Physics in Medicine and Biology* 58 5945
- Spindeldreier C.K., Schrenk O., Bakenecker A., Kawrakow I., Burigo L., Karger C.P., Greulich S. and Pfaffenberger A. 2017 Radiation dosimetry in magnetic fields with Farmer-type ionization chambers: determination of magnetic field correction factors for different magnetic field strengths and field orientations *Physics in Medicine and Biology* 62 6708
- Tijssen R.H., Philippens M.E., Paulson E.S., Glitzner M., Chugh B., Wetscherek A., Dubec M., Wang J. and van der Heide U.A. 2019 MRI commissioning of 1.5 T MR-linac systems – a multi-institutional study *Radiotherapy and Oncology* 132 114 – 120

- Torres-Xirau I., Olaciregui-Ruiz I., Baldvinsson G., Mijnheer B.J., van der Heide U.A. and Mans A. 2018 Characterization of the a-Si EPID in the unity MR-linac for dosimetric applications *Physics in Medicine and Biology* 63 025006
- van Asselen B., Woodings S.J., Hackett S.L., van Soest T.L., Kok J.G.M., Raaymakers B.W. and Wolthaus J.W.H. 2018 A formalism for reference dosimetry in photon beams in the presence of a magnetic field *Physics in Medicine and Biology* 63 125008
- van der Wal E., Wiersma J., Ausma A.H., Cuijpers J.P., Tomsej M., Bos L.J., Pittomvils G., Murrer L. and van de Kamer J.B. 2013 Code of practice for the quality assurance and control for intensity modulated radiotherapy Tech. Rep. NCS 22 Nederlandse Commissie voor Stralingsdosimetrie Delft, The Netherlands
- van Dyk J. (ed.) 1999 *The modern technology of radiation oncology* (Madison, Wisconsin: Medical Physics Publishing)
- van Heijst T.C.F., den Hartogh M.D., Lagendijk J.J.W., van den Bongard H.J.G.D. and van Asselen B. 2013 MR-guided breast radiotherapy: feasibility and magnetic-field impact on skin dose *Physics in Medicine and Biology* 58 5917
- van Zijp H.M., van Asselen B., Wolthaus J.W.H., Kok J.M.G., de Vries J.H.W., Ishakoglu K., Beld E., Lagendijk J.J.W. and Raaymakers B.W. 2016 Minimizing the magnetic field effect in MR-linac specific QA-tests: the use of electron dense materials *Physics in Medicine and Biology* 61 N50
- Verellen D., de Ridder M., Linthout N., Tournel K., Soete G. and Storme G. 2007 Innovations in image-guided radiotherapy *Nature Reviews* 7 949
- Werensteijn-Honingh A.M., Kroon P.S., Winkel D., Aalbers E.M., van Asselen B., Bol G.H., Brown K.J., Eppinga W.S., van Es C.A., Glitzner M., de Groot-van Breugel E.N., Hackett S.L., Intven M., Kok J.G., Kontaxis C., Kotte A.N., Lagendijk J.J., Philippens M.E., Tijssen R.H., Wolthaus J.W., Woodings S.J., Raaymakers B.W. and Jürgenliemk-Schulz I.M. 2019 Feasibility of stereotactic radiotherapy using a 1.5 T MR-linac: Multi-fraction treatment of pelvic lymph node oligometastases *Radiotherapy and Oncology* 134 50 – 54
- Winkel D., Bol G.H., Kroon P.S., van Asselen B., Hackett S.S., Werensteijn-Honingh A.M., Intven M.P., Eppinga W.S., Tijssen R.H., Kerkmeijer L.G., de Boer H.C., Mook S., Meijer G.J., Hes J., Willemsen-Bosman M., de Groot-van Breugel E.N., Jürgenliemk-Schulz I.M. and Raaymakers B.W. 2019 Adaptive radiotherapy: The Elekta Unity MR-linac concept *Clinical and Translational Radiation Oncology* 18 54 – 59
- Wolthaus J., van Asselen B., Woodings S., Hackett S., van Zijp L. and Raaymakers B. 2016a Difference in dose to water for photon beams with and without the presence of a magnetic field ep-1515 *Radiotherapy and Oncology* 119 5701
- Wolthaus J., van Asselen B., Woodings S., van Soest T., Kok J., de Prez L., Jansen B., de Pooter J. and Raaymakers B. 2016b Direct measurement of magnetic field correction factors, k_{QB} , for application in future codes of practice for reference dosimetry th-cd-bra-03 *Medical Physics* 43 3873
- Woodings S.J., Bluemink J.J., de Vries J.H.W., Niatsetski Y., van Veelen B., Schillings J., Kok J.G.M., Wolthaus J.W.H., Hackett S.L., van Asselen B., van Zijp H.M., Pencea S., Roberts D.A., Lagendijk J.J.W. and Raaymakers B.W. 2018a Beam characterisation of

- the 1.5 T MRI-linac *Physics in Medicine and Biology* 63 085015
- Woodings S.J., de Vries J.H.W., Kok J.G.M., Hackett S.L., van Asselen B., Bluemink J.J., van Zijp H.M., van Soest T.L., Roberts D.A., Lagendijk J.J.W., Raaymakers B.W. and Wolthaus J.W.H. Submitted, 19 Sep 2019 Acceptance procedure for the linear accelerator of the 1.5 T MRI-linac *Journal of Applied Clinical Medical Physics*
- Woodings S.J., van Asselen B., van Soest T.L., de Prez L.A., Lagendijk J.J.W., Raaymakers B.W. and Wolthaus J.W.H. 2019 Technical note: Consistency of PTW30013 and FC65-G ion chamber magnetic field correction factors *Medical Physics* 46 3739–3745
- Woodings S.J., Wolthaus J.W.H., van Asselen B., de Vries J.H.W., Kok J.G.M., Lagendijk J.J.W. and Raaymakers B.W. 2018b Performance of a PTW 60019 microDiamond detector in a 1.5 T MRI-linac *Physics in Medicine and Biology* 63 05NT04

Acknowledgements

Thank you very much Bas Raaymakers and Jan Lagendijk, for the invention and development of the MRI-linac, and for your leadership and guidance. Thanks also to Jochem Wolthaus and Bram van Asselen for your supervision and clarity of vision.

Thanks to everyone in the Radiotherapy Department. Many work colleagues and friends have made important contributions to this work including Jan Kok, Sara Hackett, Wilfred de Vries, Loes van Zijp, Peter Woodhead, Hanneke Bluemink, Theo van Soest, Leon de Prez, Charis Kontaxis, Tessa Leer, Markus Glitzner, Eline de Groot van Breugel, Lieke Meijers, Ina Jürgenliemk-Schulz, Marielle Philippens, Rob Tijssen, Eric Westzaan, Hans de Boer, Tristan van Heijst, Gijs Bol, Alexis Kotte, Sjoerd Crijns, Victor Malkov and Rosemarie Aben. My apologies to contributors that are not mentioned. Thanks to you all.

Thanks to my Elekta colleagues for their support. Specifically David Roberts, Rob Spaninks, Marcel Schuring, Yury Niatsetski and Daniel O'Brien.

Thank you Evelyn and Tessa. A little bit for being great paranymphs. But mostly for being great friends.

Thank you mum and dad (Jean and Terry Woodings) for your life-long love, support and encouragement. Still needed, still generously given.

About the author

Simon graduated from the University of Western Australia in 1996 with a bachelor of science and first-class honours. His thesis was titled “A plausible physical cause of mass cetacean strandings”. After years studying astronomy and supernovae, Simon began his medical physics work and training in 2001 at Royal Perth Hospital and Perth Radiation Oncology. He was accredited in radiotherapy physics by the Australasian College of Physical Scientists and Engineers in Medicine (ACPSEM) in 2007, and became an examiner for the College from 2012 – 2017. In 2010 Genesis Cancer Care (WA) acquired and created a network of four radiotherapy centres with seven linear accelerators, to which Simon contributed as Head of Physics.

Through good luck and great timing, Simon joined the team at University Medical Center Utrecht (UMCU, Netherlands) in 2015. Just in time to see the benefits of the huge effort from UMCU, Elekta and Philips in designing and creating the Elekta Unity MRI-linac. Simon contributed to the design and implementation of tests for acceptance, commissioning and quality assurance, with the goal of making the transition from research system to full clinical use. This was achieved with the first patient treatment at UMCU in May 2017, and the first treatment with the CE-marked Unity at UMCU in August 2018.

